THE UNIVERSITY OF CHICAGO

EXPLORATION OF ORGANIC MATERIALS FOR LIGHT-HARVESTING AND LIGHT-EMITTING OPTOELECTRONIC DEVICES

A DISSERTATION SUBMITTED TO

THE FACULTY OF THE DIVISION OF THE PHYSICAL SCIENCES

IN CANDIDACY FOR THE DEGREE OF

DOCTOR OF PHILOSOPHY

DEPARTMENT OF CHEMISTRY

BY

VALERII SHARAPOV

CHICAGO, ILLINOIS

DECEMBER 2019

TABLE OF CONTENTS

LIST OF SCHEMES

LIST OF FIGURES

LIST OF TABLES

ACKNOWLEDGEMENTS

The graduate school has probably been one of the most challenging but at the same time rewarding experiences in my life so far. It is challenging to ask the right research questions and search for the right answers. However, as a reward, you learn something new about the world around and something new about yourself. I would like to thank my advisor, Professor Luping Yu for guiding me through my Ph.D. journey. His patience, insightful questions, and advice helped me to overcome the difficulties that I encountered on my way. I would also like to thank Professors Dmitri Talapin and Bozhi Tian for serving on my dissertation committee.

I thank Dr. Justin Jureller, Dr. Qiti Guo, Dr. Alexander Filatov, and Yimei Chen for their help with the instruments and experimental techniques that made my research possible. I also appreciate help provided by our collaborators Dr. Wei Chen and Dr. Joe Strzalka with the synchrotron x-ray scattering measurements at Argonne National Laboratory APS.

I am lucky to have found incredible and collaborative lab mates in the Luping Yu group. I thank our past group members Dr. Luyao Lu for being my mentor in solar cell research and Dr. Donglin Zhao for all her help with the device work and for being a great friend. Organic synthesis work done by our past group members Dr. Qinghe Wu, Dr. Zhengxu Cai, Dr. Tianyue Zheng, Dr. Na Zhang, and Alexander Schneider was essential for my research. Without them, my projects in organic materials would not be possible. I thank our previous group members Dr. Wai-Yip Lo, Dr. In Hwan Jung, Dr. Lianwei Li, Dr. Junpeng Wang and Dr. Aireal Jenkins for their advice and support. I thank current members of our group Andriy Neshchadin, Dr. Xunshan Liu, Mohammad Awais, Dr. Zhen Zhang, and Dr. Dafei Yuan for their synthesis work, their support, and insightful discussions. It has been a pleasure working with you all.

I thank Melinda Moore, Dr. Vera Dragisich, Dr. Meishan Zhao, Dr. Valerie Keller and other staff members of the department of chemistry that have been working hard to make our transition to graduate school as smooth as possible.

Finally, I would like to thank my family for all the opportunities that I could pursue in my life with their encouragement and constant support. Even though my family is thousands of miles away, my friends here in Chicago made my daily grad school life much brighter. I especially thank my friends Andriy, Polina, Vlad and Jingchen for being there for me no matter what.

CHAPTER 1

INTRODUCTION

Every year hundreds of new materials are discovered by researchers worldwide. The purpose of these discoveries is to identify materials that possess new exciting properties or have known properties but greatly improved. These properties may be mechanical, electrical, optical, magnetic or a combination of those. Optoelectronic materials, as follows from their name, are employed in devices where light is used to affect electronic processes in materials or vice versa and thus provide a useful functionality.[1] Devices that belong to this category include solar cells, light-emitting diodes (LED), light-emitting field-effect transistors (LEFET), photodetectors and others. Often, however, not just one material is used in these devices but quite a few. They may form sandwich-like structures, be incorporated in a blend with other materials or be a combination of both. When multiple materials are combined together in a single device, many potential sources of failure may arise from the mutual incompatibility of device components or instability under device fabrication/operation conditions. Therefore, proper identification of potential candidate materials for high performing devices is of great importance. The mere trial-and-error approach will be highly inefficient, thus knowledge of fundamental principles governing interaction of components is crucial for rational choice of materials.

This chapter describes two types of optoelectronic devices. Devices of the first type are light-absorbing and convert optical energy into electrical form. This type of devices includes solar cells and photodetectors. Devices of the second type are light-emitting and convert electrical energy into the optical one. The focus of this chapter will be on organic solar cells, representing light-harvesting devices and light-emitting field-effect transistors representing light-emitting optoelectronic devices. In the solar cell part, a brief overview of organic photovoltaic devices and major processes that facilitate photon-to-electron conversion will be given. Then I will consider fundamental thermodynamic and kinetic effects that govern photovoltaic active layer film formation and how these principles may be used to form blends with required specifications. These blends may consist of organic polymers, small molecules, and combinations of both. Lastly, I will summarize some of the best performing photovoltaic blends with a particular emphasis on structure-property relationships that may help to deduce design rules for future generations of high performing photovoltaic materials. In light-emitting field-effect transistors part I will give an overview of fundamental processes that govern gate modulated switching behavior and simultaneous light emission, describe various device components and geometries and summarize some of the best-performing systems for light-emitting applications in FET.

1.1. Organic Solar Cells

1.1.1 General Overview of Bulk Heterojunction Solar Cells

Photovoltaic devices (solar cells) are designed to convert optical power (sunlight) into electrical power using the photovoltaic effect in semiconductors. The efficiency of this conversion is described with a parameter called power conversion efficiency (PCE), which, in

turn, depends on the open-circuit voltage (V_{OC}), the short-circuit current density (J_{SC}) and the fill factor (FF). Historically, since the invention of the solar cells the first material employed was silicon, which is still widely used in monocrystalline and polycrystalline forms in modern commercially available devices. Later on, other inorganic semiconductors came into play, such as GaAs, PbS, CdSe, and others. Such a wide variety of available semiconductors is especially important for photodetector devices (PD) where both narrow and wide coverage in different parts of the spectrum are important.[2–4]

Inorganic materials offer huge advantages for PV and PD devices, such as broad wavelength coverage, chemical stability of the devices and higher crystallinity. At the same time, they have multiple disadvantages as well, such as expensive purification and doping methods, usage of toxic and/or rare elements (Cd, In, Te), high density and thus higher weight of fabricated devices. Therefore, organic materials may offer a viable alternative to inorganic semiconductors bringing all rich arsenal of organic chemistry to synthesize and optimize these compounds, potential of using green technologies[5,6] to manufacture these devices, as well as potential to manufacture lightweight and flexible devices through the roll-to-roll process.[7,8] A typical architecture of these devices includes an active layer, where photon-to-charge conversion occurs, sandwiched in between of transparent electrode (usually transparent conductive oxide, such as ITO or FTO) and a metal electrode (Ag, Al, Au, etc). Additional electron or hole transporting layers are often inserted in order to improve interfacial charge transfer.[9] An active layer consists of two kinds of materials – an electron donor and an electron acceptor, which typically absorb in complementary parts of the spectrum thus covering a wider range of wavelengths, which maximizes device performance. A photon that is absorbed by one of the

components in the active layer transitions the molecule to its excited state and thus creating a Frenkel exciton (localized electron-hole pair that is tightly bound due to a lower dielectric constant of organic materials).[10–12] The exciton diffuses to the donor/acceptor interface and dissociates, taking advantage of the driving force provided by a favorable downward energy cascade between the donor and the acceptor.[13] The exciton dissociation generates free charge carriers that are collected at the device terminals - electrons are collected at the cathode of the device and holes are collected at the anode. Since generation of free charge carriers takes place at the interface between the electron donor and the acceptor, a concept of bulk heterojunction (BHJ) was introduced, where donors and acceptors are mixed in a single blend, forming a myriad of interfacial connections, thus significantly increasing the efficiency of this process, compared to planar heterojunction devices, where only one heterojunction exists **(**Figure 1.1**)**.[14] When such a complex structure as BHJ blend is formed, a countless number of parameters need to be optimized to maximize the performance of the device. For example, optoelectronic parameters may include materials' light absorption properties, intramolecular polarization, and intramolecular charge carrier mobility. These properties may be controlled through rigorous materials design. For instance, the introduction of molecular units with quinoidal character results in the formation of flat rigid polymers with the narrow bandgap.[15–17] This, in turn, forms polymers with wider light absorption. In addition, when these units are combined to form an intramolecular donor-acceptor pattern in a polymer, this provides an additional driving force for charge separation upon excitation.[18,19] Nowadays, the theoretical computer simulation analysis provides useful tools to predict optoelectronic properties of the material and thus use rational optimization techniques in materials design.[20,21] The other group of parameters includes the ones

related to morphology of photovoltaic films. Since the scale of interactions includes millions of molecules forming domains and interfaces it is much more challenging to provide rational predictions for these properties, therefore trial-and-error approach is often used. General guidelines include requirements for phase separation, molecular orientation, and phase purity. Precise phase separation is of critical importance for these devices since a very fragile balance must be kept between exciton dissociation, charge transport, and dissociation processes.[22–25] When excitons are generated in the bulk of the domain, they diffuse to a donor-acceptor interface and dissociate, thus contributing charge carriers to a circuit. However, for a typical organic material exciton diffusion distance before recombination is around 9-13 nm depending on the material, therefore only excitons generated within this depth from the interface effectively contribute to electrical current.[26] If domains are too big, then a very small fraction of excitons contribute to current, which decreases the efficiency of a device.[27] At the same time, charge transport takes place through a percolating network of domains, therefore when domains are too small, a formed structure has very finely intermixed donor and acceptor contacts, thus providing multiple points for charge recombination during its transport and again decreasing device efficiency.[25] Therefore a very fine balance between charge generation and transport is required.

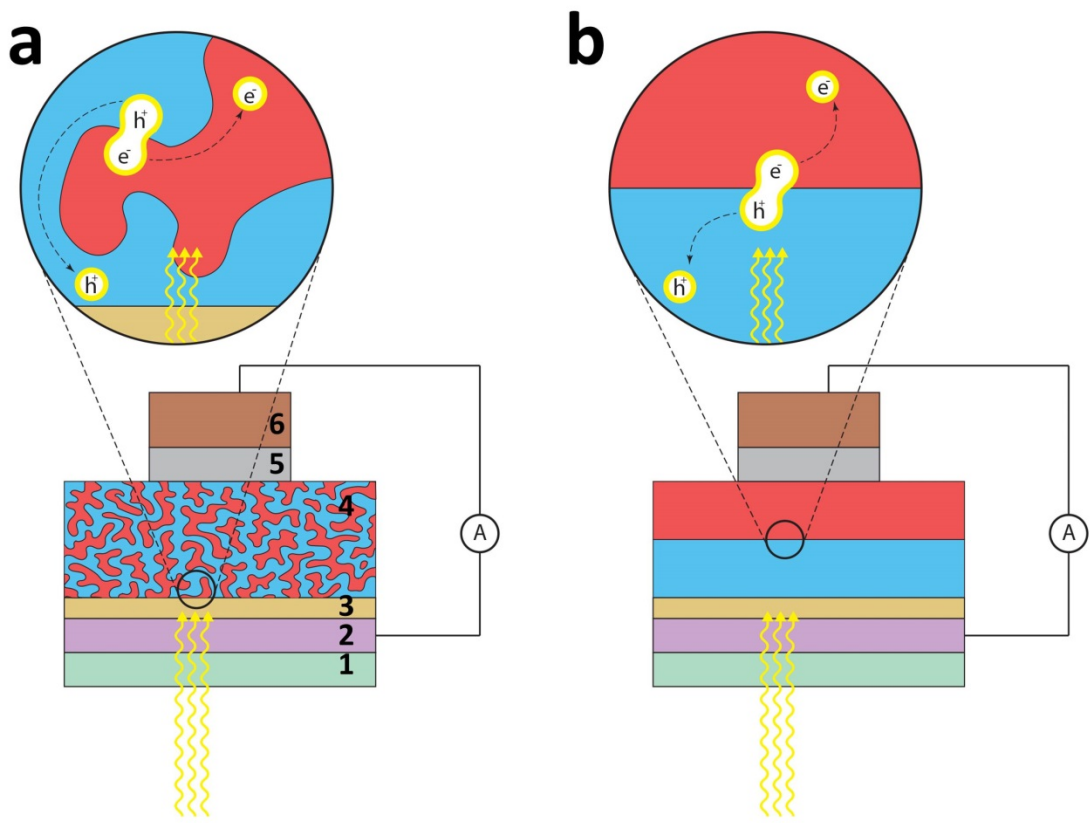

Figure 1.1. a) Bulk heterojunction solar cell device. Layers in the device are marked as follows: 1-transparent substrate (glass, polymer), 2-transparent conductive layer (ITO, FTO), 3-hole transporting layer, 4-bulk heterojunction active layer consisting of electron donor and acceptor, 5-electron transporting layer, 6-metal electrode; b) Planar heterojunction device.

1.1.2. Thermodynamics and Kinetics of Polymer Mixing

Typical organic solar cells have several components blended together in a single film. These components may include electron donor and electron acceptor systems, charge conducting materials, morphology modifiers (plasticizers), inert polymers serving as a matrix and active material being dispersed in it and so on. Despite different requirements for each of these blends, principles that govern film formation are the same. In the end, what determines a

final state of a blend is the interplay between thermodynamic parameters characterizing blend components and kinetic details of film formation.

From the perspective of thermodynamics, the formation of any blend will be governed by its free energy, which in turn has energetic ΔU_{mix} and entropic ΔS_{mix} terms.

$$\Delta F_{mix} = \Delta U_{mix} - T\Delta S_{mix}$$

Since ΔF_{mix} is a thermodynamic potential, a negative value of it indicates favored mixing, which, in turn, depends on signs of energetic and entropic terms. The entropic component of mixing is always positive, thus promoting mixing, however, its exact value depends on the nature of the mixing species, namely whether these components are small molecules or polymers. When two small molecules mix (for example a solvent and a small molecule solute) the number of their possible permutations in space is very large and depends on the volume available for mixing. At the same time, when small molecules are connected in a polymer chain, this imposes geometric restrictions on their movements and a number of possible permutations decreases, thus decreasing an entropic component of mixing, however still keeping it positive. Therefore energetic term of free energy becomes a parameter determining whether mixing is going to occur or not. For multicomponent polymer systems an energetic term is often conveniently described with Flory-Huggins theory.[28,29] This theory describes polymer as a system of cells that occupy a cell space together with solvent and interactions within this system are described using statistical approach. Even though it was developed in order to explain polymer solutions, it may also be used to describe polymer blends.

According to Flory-Huggins, the total change in free energy ΔF_{mix} upon mixing of two components A and B may be expressed as follows:

$$\frac{\Delta F_{mix}}{k_B T} = \phi_A ln\phi_A + \phi_B ln\phi_B + \chi\phi_A\phi_B$$

where ϕ is volume fraction of component A or B, χ is the Flory-Huggins interaction parameter, which in turn depends on temperature T as $\chi=C+D/T$ where C and D are constants determined for a specific combination of blend components. The first two terms in this equation originate from entropic mixing and are always negative, thus promoting mixing. The third term describes the energy of interactions upon mixing and may be positive (opposing mixing), negative (promoting mixing) or zero. Figure 1.2a shows an example of the free energy versus composition curve for a symmetrical system (molecular size of components A and B is equal) for several temperatures (T_5 to T_1).

It may be noticed that at the highest temperature T_5 the curve has a parabolic shape with an energy minimum at ϕ=0.5, indicating that components A and B form a stable homogeneous mixture for all component ratios under these conditions. When the temperature is decreased and reaches a critical level T_C, a curve reaches a point at which its curvature changes from concave downward to concave upward and T_C is an inflection point at which $\frac{\partial^2 \Delta F}{\partial \phi^2}$ is equal to zero. This point indicates that the miscibility of the blend components has reached a limit and a mixture phase separates at the temperatures lower than T_C.

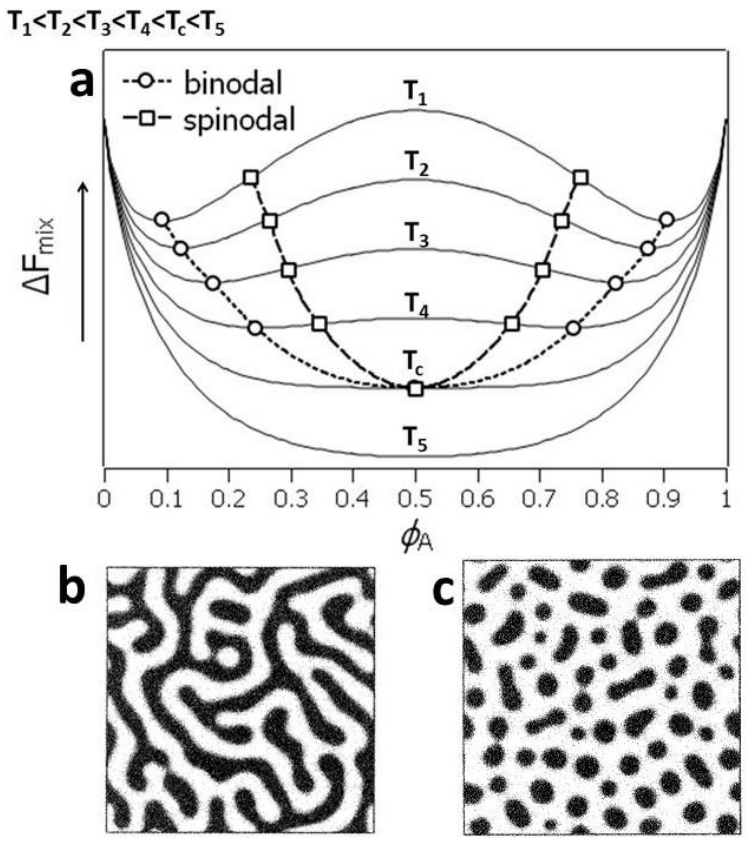

Figure 1.2. a) Free energy versus composition curve for varying temperatures (adapted with permission from ref[30]. Copyright 2008 Elsevier); b) Simulated morphology of a blend after spinodal decomposition; c) Simulated morphology of a blend after phase separation through nucleation and growth mechanisms (figures b and c are reprinted with permission from ref [31]. Copyright 1998 EDP Sciences).

The appearance of two minima on the energy curve indicates phase separation, meaning that two stable phases can be formed and the composition of these phases is determined by a concentration corresponding to an energy minimum. Each of the curves corresponding to temperatures T1 to T4 has two important points. The first one is the point at which $\frac{\partial \Delta F}{\partial \phi} = 0$ (marked with a symbol ○ in Figure 1.2a) showing an energy minimum. The second one is the

point at which $\frac{\partial^2 \Delta F}{\partial \phi^2} = 0$, (marked with a symbol □ in Figure 1.2a) showing an inflection point at which an energy maximum of the curve (an unstable region) transitions to energy minimum (stable region). If all minima points are connected with a line, they will form a binodal line, whereas connected inflection points form a spinodal line. The area in between of spinodal and binodal lines is called a metastable phase. If the system is unstable (located in the areas of the curve in between of two spinodal lines), then spontaneous phase separation happens upon the slightest composition fluctuation. This spontaneous phase separation is called spinodal decomposition and a simulated example of it is shown in Figure 1.2b. At the same time, if the system is in a metastable state, it is more resistant to fluctuations. In this case phase separation may occur through a mechanism of nucleation and growth if composition fluctuations are large enough to form stable nuclei of phase larger than a critical size (Figure 1.2c). Even though the example above describes a binary system where solvent and solute molecules have equal size, similar conclusions can be made for more complicated systems with multiple different components, such as polymer blends.

Most of the blends used for optoelectronic applications must meet specific requirements for phase separation of components in order to have good performance. For example, neither finely intermixed, nor largely phase-separated blends are used for organic solar cells. Bulk heterojunction SC with the highest power conversion efficiency tend to have donor and acceptor components phase-separated to form domains of the size around 10 nm for optimum charge generation and transport.[32,33] Domains much larger or smaller than this, or with low phase purity typically result in increased charge recombination and thus deteriorated performance.[34,35]

Therefore a rational choice of components and their amounts are critically important for future progress in the field.

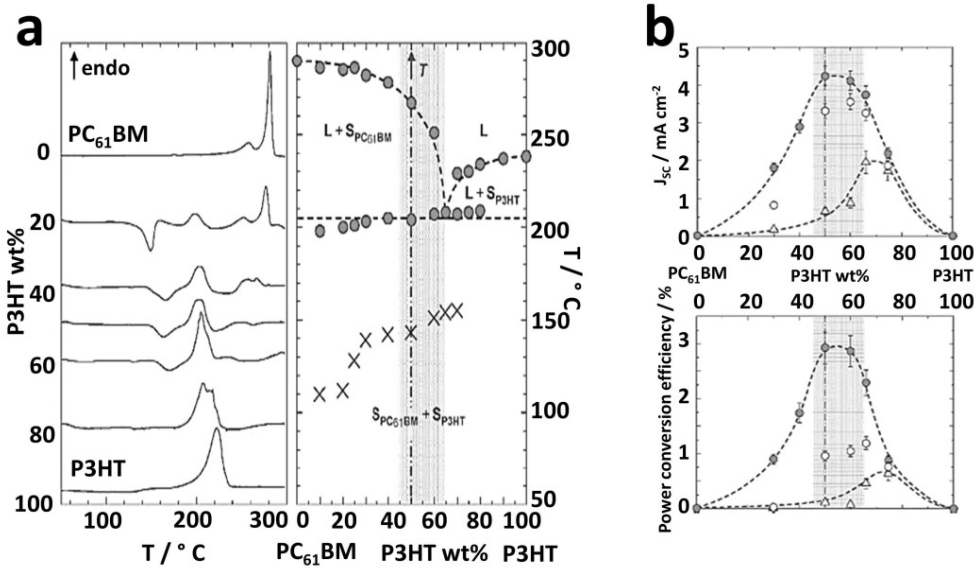

Figure 1.3. a) DSC heating thermograms (left) and corresponding temperature/composition diagram (right) for P3HT:$PC_{61}BM$ system. Crosses represent the onset of crystallization; b) Performance of solar cell devices for systems with an increasing ratio of P3HT. Filled circles represent devices thermally annealed at 140 °C, open triangles represent devices melt-quenched from 290 °C, and open circles represent devices after further annealing at 140 °C. (Reprinted with permission from ref [36]. Copyright 2008 John Wiley and Sons).

It was proposed that studying the eutectic behavior of the mixtures may be a useful tool to use for determining the optimum donor-acceptor ratio in a blend.[36] When a series of blends with varying ratios of P3HT and $PC_{61}BM$ was made and their DSC thermograms were measured, it was observed that mixtures with 65 weight % of P3HT had eutectic behavior (Figure 1.3a). At the same time, device performance was measured for these blends and the highest current density was found for blends with the hypoeutectic composition, corresponding to a slight excess of $PC_{61}BM$ (shadowed area in Figure 1.3). Similar results were observed for other poly-

3-alkylthiophenes and $PC_{71}BM$, however eutectic composition for these systems was slightly shifted. Authors argue that the blends near the eutectic point have optimized phase separation which results in the well-balanced formation of the domains of the optimum size for efficient charge percolation and the interfaces with the surface area large enough for efficient exciton dissociation. At the same time, a slight excess of PCBM is necessary for higher electron mobility. Similar studies have been conducted for P3HT and small molecule non-fullerene acceptors. Authors observed that for blends with acceptors YF25 and K12, devices with the maximum performance are also hypoeutectic, similarly to P3HT:PCBM case.[37] Moreover, highly crystalline and highly amorphous non-fullerene acceptors that did not form eutectic mixtures with P3HT had much inferior performance.[38]

In recent years a tremendous number of new photovoltaic materials have been developed making a number of their potential combinations overwhelmingly large. Therefore, a problem of rational choice of potential candidates for further optimization and detailed studies within this huge pool of materials is currently of great importance. Recently Harald Ade and co-workers proposed an approach aimed at resolving this exact issue.[39] The authors used a modified Flory-Huggins interaction parameter $\chi_{aa}(T)$ (temperature-dependent amorphous-amorphous interaction parameter) to identify the best combinations of donors and acceptors and establish quantitative correlations between material properties, purity of domains and device performance. They found that pairs of materials for which the values of $\chi_{aa}(T)$ were above a threshold value of ~0.72 formed blends with higher phase purity and thus higher FF in the solar cell device. Moreover, it was showed that a similar interaction parameter measured from DSC $\chi_{aa}(T_m)$ may be used as an excellent tool to rationalize performance in 15 different donor-acceptor systems (Figure 1.4).

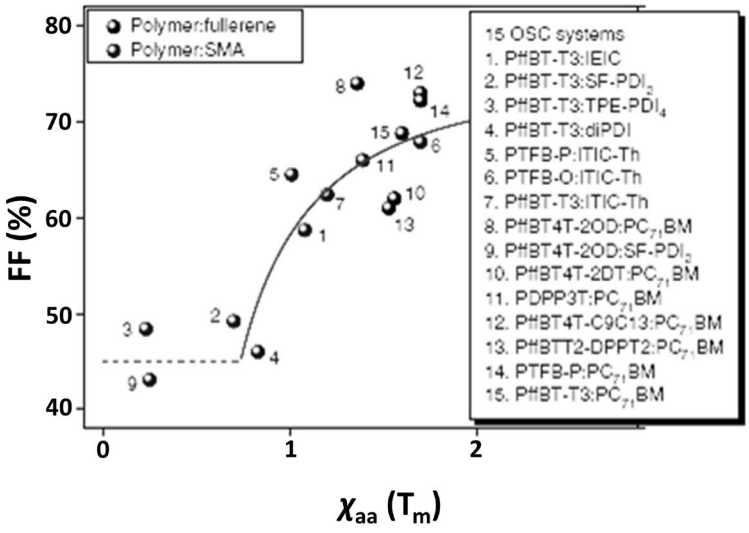

Figure 1.4. Dependence of FF on interaction parameter $\chi_{aa}(T_m)$ estimated from DSC for 15 pairs of electron donors and acceptors. (Reprinted with permission from ref. [39]. Copyright 2018 Springer Nature).

Even though thermodynamic properties play a crucial role in predicting compatibility and providing useful tools for the rational choice of photovoltaic materials, the final outcome largely depends on the kinetics of film formation. For example, when photovoltaic film is processed from a fast-drying solvent, it is often observed that very large (>100 nm) domains of polymer and PCBM are formed. However, addition of small quantities of high boiling point solvents, such as DIO or o-dichlorobenzene, often results in much finer phase separation and superior device performance. Studies on real-time film-drying dynamics helped to rationalize this result.[40] Thus, for a low boiling point solvent (chloroform), it was observed that fast spinodal decomposition preceding polymer aggregation occurred during film drying. This resulted in formation of large aggregates of polymer and PCBM phases that deteriorated device performance. However when high boiling point solvent additive was added, the mechanism was

drastically different. Polymer pre-aggregation induced by a solvent additive suppressed fast liquid-liquid demixing which in turn prevented formation of large PCBM aggregates (Figure 1.5).

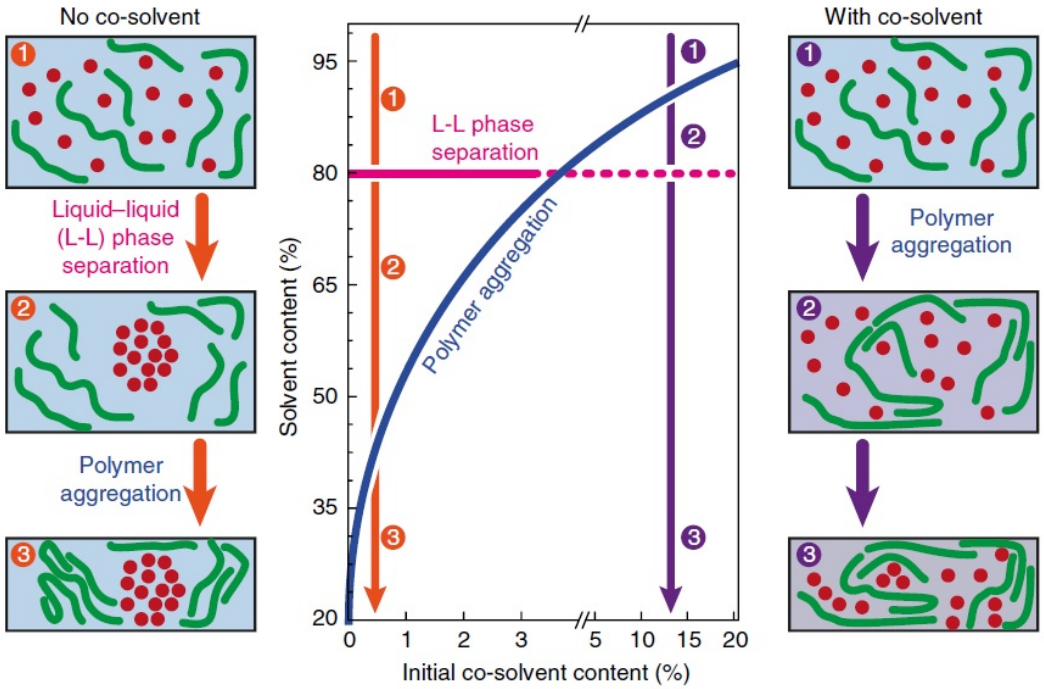

Figure 1.5. Schematic diagram showing mechanisms of film formation with (right side) and without (left side) presence of high boiling point solvent additive. (Reprinted with permission from ref [40]. Copyright 2015 Springer Nature).

1.1.3 Ternary Blend Organic Solar Cells

One of the recently emerging fields in the organic photovoltaics is ternary blend solar cells (or in more general case multiple component blends).[41–45] A key feature of these systems is that in addition to the main blend component (typically a polymer donor and a small molecule acceptor) another photoactive component is added which often results in enhanced performance

of OPV devices. Some of the most common high-efficiency donors and third components are summarized in Figures 1.6 and 1.7, respectively.

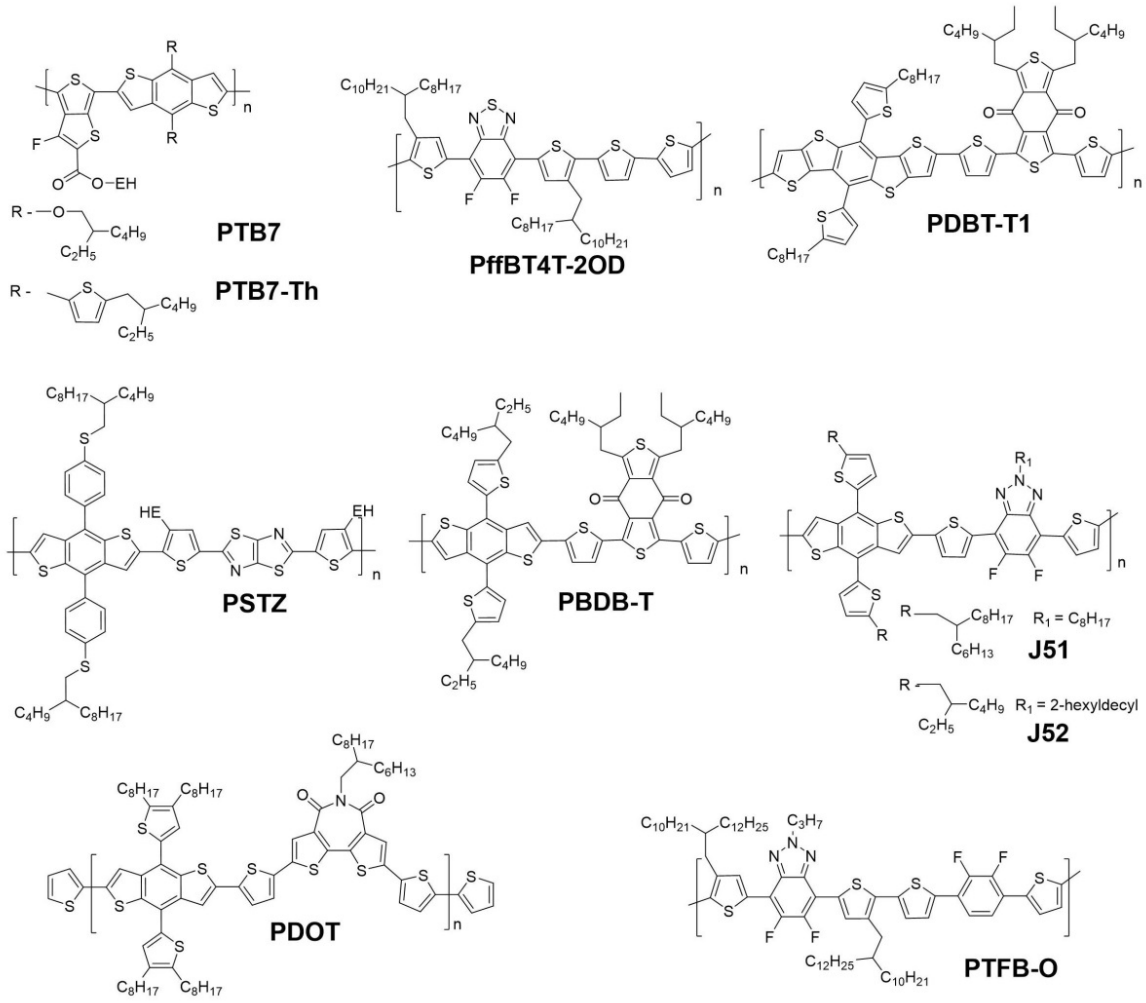

Figure 1.6. Molecular structures of donor polymers for high efficiency organic solar cell devices.

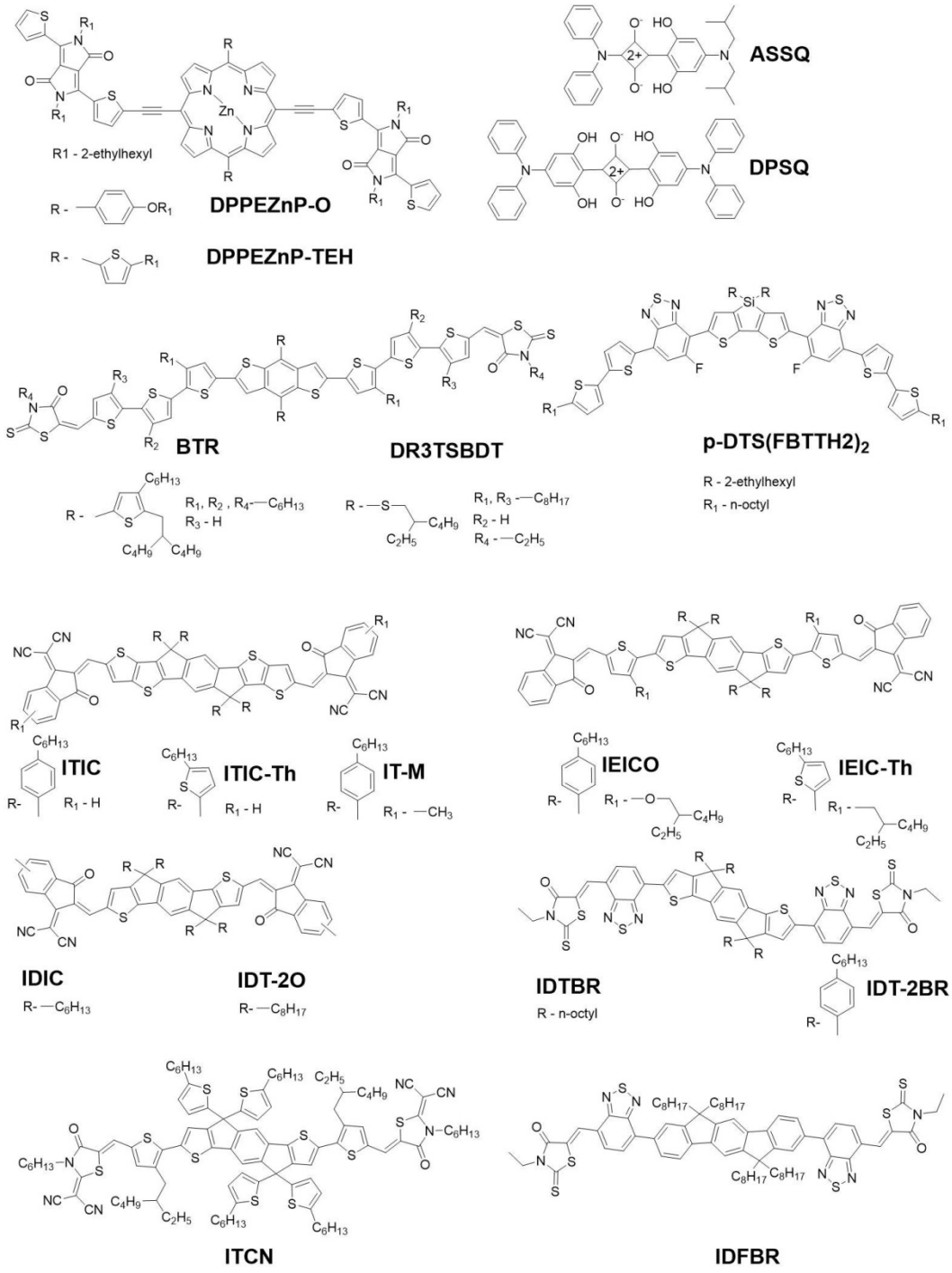

Figure 1.7. Molecular structures of third components used for high-efficiency ternary blend organic solar cells.

In order to be a good third component, a material needs to meet a range of criteria. These criteria include complementary light absorption with the blend main components, a cascade of energy levels facilitating charge transport between the phases and compatible morphology. Another parameter that is especially important for polymer third components is molecular weight and polydispersity.[46] Because of large batch-to-batch variations in molecular weight and polydispersity, these blends may suffer from the irreproducibility of device performance. Therefore small molecule third components were developed as a viable alternative. Typical mechanisms involved in PCE enhancement include harvesting of additional photons due to complementary absorption of the third component, relay effects due to energy level cascades which allow for additional harvesting of charge carriers and morphology effects.

Additional light harvesting is possible when a third component has a light absorption spectrum complementary to the spectrum of blend's main components and with high absorption coefficient. Additional light harvesting is usually required in the areas where main components lack absorption – typically UV region and near-IR. Organic dyes, such as based on porphyrin and squaraine moieties, showed the most promising results recently in near-IR sensitization. Porphyrin-zinc molecules DPPEZnP-O and its modified version DPPEZnP-TEH were successfully employed as third components in PTB7:$PC_{71}BM$ based devices.[47,48] The role of these additives was two-fold – expanding photon harvesting by an additional absorption in 800-900 nm region and improving charge transport in the device by taking advantage of cascading energy levels. The authors observed an increase in PCE from 7.47% to 8.39% for devices with DPPEZnP-O as a third component. Even higher results were achieved for DPPEZnP-TEH, where thiophene unit was added to the side chains thus expanding conjugation – PCE increased

from 7.85% to 9.52% after incorporation of the third component and improved even further to 11.03% after cathode interfacial layer with higher electrical conductivity was inserted. Another example of near-IR sensitization is incorporation of squaraine dyes. Small quantities of these compounds were used in quaternary blend solar cells in PTB7/$PC_{71}BM$ and PTB7-Th/$PC_{71}BM$ systems to achieve high PCEs. Two sensitizers have been used in PTB polymers:$PC_{71}BM$ blends – ASSQ absorbing near 550 nm and DPSQ absorbing near 720 nm, therefore covering regions where absorption of the main components is weaker.[49] When blend components formed a quaternary blend with only 2% of each sensitizer present, the authors achieved an increase in PCE from 8.7% to 10.3% for PTB7 system, originating mostly from an increase in J_{SC} and FF, and an increase from 9.6% to 10.7% for PTB7-Th. They observed a cascade of electron and energy transfer processes – photon energy harvested by ASSQ was transferred through Förster resonance energy transfer (FRET) mechanism to DPSQ and PTB7 and charge transfer was observed from PTB7-Th to DPSQ and eventually to PCBM.

The other enhancement mechanisms originate from morphology effects. These effects may be divided into several categories – crystallinity, control of domain size and control of domain purity. The addition of crystalline small molecules as third components was recently demonstrated as a viable strategy to achieve higher PCEs. For example, two similar molecules (DR3TSBDT and BTR) were used to increase crystallinity of the PTB7-Th:$PC_{71}BM$ blend. Despite their structural similarities, incorporation of these molecules had drastically different effects on morphology.[50,51] When highly ordered liquid-crystalline small molecule benzodithiophene terthiophene rhodamine (BTR) was used as a third component, this allowed fabrication of thicker devices where PCE increased from 7.07% to 11.40% for 250 nm film. A

significant increase in hole mobility was observed (more than 5-fold) and the effect was mostly attributed to a shorter π-π stacking distance, increased crystallinity and increased domain purity (0.53 for binary versus 0.75 for ternary blend).[50] Similar results were observed for another system with PffBT4T-2OD:$PC_{71}BM$ as the main components and BTR as the third component, where maximum achieved PCE was 10.59% for 280 nm film.[52] At the same time for a modified version of this small molecule DR3TSBDT, where thiophene unit was replaced with alkylthio chain and a shorter alkyl chain on the acceptor units, drastically different morphology effects were observed. First, a gradual change in device V_{OC} was observed upon addition of DR3TSBDT, which typically indicates an alloy formation with the main components, while the opposite trend was observed in case of BTR – V_{OC} stayed fixed at the PTB7-Th/$PC_{71}BM$ level. In addition, authors observed appearance of mixed face-on edge-on phase for polymer blend and an increase in correlations length in q_{xy} direction for ternary blends. Typically, a face-on orientation of π-π stacks is beneficial for charge transport, however despite randomization in stack orientation in this case, authors observed a slight increase in hole and electron mobilities and an overall PCE increase from 10.10% to 12.10% (certified 11.76%) for binary and ternary devices, respectively.[51] Another small molecule third component that demonstrated promising results is p-DTS(FBTTH2)2 in PTB7-Th/$PC_{71}BM$ system. When small amount of this small molecule (15%) was added to a polymer blend and film was processed from chlorobenzene:DIO solution, the authors observed PCE of 9.20% and 10.50% for binary and ternary devices, respectively.[53] The addition of the small molecule did not affect phase separation of the components and it formed an alloy with the blend main components and resulted in an increased ratio of face-on to edge-on oriented polymer π-π stacks and increased correlation lengths in the

film. Very similar results were observed for films coated from a greener non-halogenated solvent *ortho*-xylene which also allowed thicker films (~270 nm) and a maximum PCE of 10.78% for optimized ternary blend devices.[54]

There are also cases when multiple enhancement mechanisms contribute simultaneously. One class of the materials where multiple mechanisms were successfully balanced is a family of fused-ring electron acceptor (FREA) materials. These molecules have a very flat fused ring donor unit (indacenodithiophene or dithieno-indacenodithiophene) in the middle of the molecule and two acceptor units at the periphery of the molecule. The donor part is shielded with non-conjugated groups, therefore its participation in electron transfer processes in the device is minimized. The molecule becomes end-capped with the electron acceptor moieties. In addition, this family of molecules has unique optical properties absorbing light in the visible and near-IR parts of the spectrum, which usually lack coverage in other types of materials. Several different types of ternary blends demonstrated superior performance with the FREA materials. We will categorize them into three groups: systems with the FREA and fullerene-based acceptors, systems with the FREA and another non-fullerene non-FREA acceptor and systems with two FREA-type acceptors. For example, ITIC-Th was studied as the third component in PDBT-T1:$PC_{71}BM$ system.[55] Authors observed PCE increase from 9.29% for binary to 10.48% for ternary device (conventional architecture) with 50% content of ITIC-Th, attributed mostly to an increase in V_{oc} and J_{sc}. Enhanced performance originated mostly from an increase in hole and electron mobilities and additional light harvesting in near-IR region. No major changes took place in molecular packing and three separate phases were observed – polymer, ITIC-Th and $PC_{71}BM$, indicating that both polymer:ITIC-Th and polymer:$PC_{71}BM$ systems form independent

percolation networks and thus work in parallel-like manner. ITIC was also used as a third component in a similar polymer system PBDB-T:$PC_{71}BM$.[56] The optimum composition for this system was PBDB-T:ITIC:$PC_{71}BM$ (1:0.7:0.3), which is much higher than in previous case and here effectively $PC_{71}BM$ is the third component. When 30% $PC_{71}BM$ was added to PBDB-T:ITIC blend, the efficiency increased from 9.6% to 11.0% mostly due to an increase in J_{SC} and FF. An increase in FF was attributed to an increase in hole and electron mobilities, while an increase in J_{SC} was attributed to enhanced light harvesting, improved morphology (increased donor and acceptor correlation lengths). Moreover, the authors observed that the addition of $PC_{71}BM$ enhances favorable vertical distribution of components (for inverted architecture) – acceptors concentrate at the bottom of the device and polymer forms a crystalline phase at the interface near hole collecting electrode which improves efficiency of charge transport. When ITIC was replaced with a wider band gap acceptor IDT-2O in the same system, surprisingly high PCE was observed as well, even despite the narrower absorption coverage.[57] Ternary blend showed increased PCE (inverted configuration) of 10.67% compared to binary blends PBDB-T:$PC_{71}BM$ (7.47% PCE) and PBDB-T:IDT-2O (9.65% PCE). The increase originated from enhanced light absorption, increased and more balanced hole and electron mobilities and improved morphology. The addition of $PC_{71}BM$ into a blend decreased excessive aggregation of IDT-2O thus resulting in more balanced phase separation. Interestingly, a less crystalline analog of IDT-2O where alkyl chains were replaced with bulkier alkylphenyl chains IDT-2B showed the opposite trend and ternary blend performance decreased upon addition of $PC_{71}BM$ which indicated a significant disruption in electron-conducting phase. Very impressive results were achieved for the same polymer PBDB-T and methylated ITIC IT-M when bis[70]PCBM was

used as the third component.[58] Upon incorporation of 20% bis[70]PCBM the efficiency of devices increased from 10.80% to 12.20% PCE which is currently one of the highest results for single-junction ternary blend OPV. The enhancement was attributed to extended absorption in short wavelength region, increase in hole and electron mobilities and preferential concentration of bis[70]PCBM on the top surface of the film, at the interface between the active layer and a cathode which is favorable for charge transport in devices of conventional architecture.

Incorporation of the FREA in polymer:PCBM system may also result in thicker film devices. Thus, incorporation of 20% ITIC in PDOT:$PC_{71}BM$ system, increased PCE from 9.54% for a binary device to 11.21% for ternary device in 230 nm film.[59] The device performance was highly dependent on the amount of solvent additive DIO present. The crystallinity of ITIC phase in the ternary blend increased with increasing content of DIO from 0% to 1%, however at higher concentrations large aggregates of ITIC were formed that deteriorated device performance. The optimum PCE was observed for 0.5% DIO.

Devices with the FREA acceptors and polymer non-fullerene acceptors were used as a viable strategy for high performing devices. Thus, naphthalene diimide (NDI) based polymer acceptor N2200 was used a third component in PBDB-T:ITIC, PBDB-T:ITIC-Th and PBDB:IT-M blends.[60] Impressive results were achieved when 10% of N2200 was incorporated. For blends with PBDB-T and ITIC, the PCE increased from 10.03% for binary to 11.41% for ternary blends. Even better results were achieved for ternary devices with ITIC-Th and IT-M – 11.40% and 12.10%, respectively. The enhancement originated from a more balanced hole and electron mobility, extended light absorption and more pronounced face-on orientation in PBDB-T and

ITIC upon incorporation of N2200. In addition, these devices showed excellent air stability – 80% of initial PCE was retained after storage in air for 1000 h.

There are multiple reports on ternary blends where two FREA-type acceptors are present in the film with one polymer donor and demonstrate excellent power conversion efficiencies of 11% and higher.[61–66] The common feature of these systems is the presence of highly crystalline wide band gap donor polymer and two highly compatible acceptors forming an alloy-like acceptor phase. It has been suggested that the ability to form an alloy is highly dependent on the surface tension of the materials and even structurally dissimilar systems having close surface tension may form an alloy.[61] As a result of alloy formation V_{OC} has a linear dependence on the device composition thus avoiding pinning. Also, addition of the third component may fine-tune crystallinity of acceptor alloy phase typically resulting in crystalline face-on structures to be formed.

1.1.4. OPV Conclusions

In this part of the chapter, I have provided an overview of the blends of organic materials for photovoltaic applications (Table 1.1). We have covered fundamental thermodynamic principles that govern formation of polymer blends and provided specific examples of how these principles may be used to predict and study their behavior. Additional examples were given on how processing conditions may affect kinetics of film formation and thus largely determine the final outcome and eventually performance of the devices. We have applied this material to summarize some of the best performing blends in modern organic photovoltaics and deduce common characteristics of these blends that resulted in high performance. Special attention has been paid to ternary blend solar cells – one of the emerging fields in OPV that significantly

progressed recently due to tremendous success in the development of high-performance non-fullerene electron acceptors.

Due to increasing energy needs, the importance of alternative energy sources, such as photovoltaics, will be growing in the future. Search for new photovoltaic materials will be accompanied by the simultaneous development of theoretical and experimental tools capable of predicting materials properties and avoid the trial-and-error approach in the next generation of high-efficiency photovoltaic materials.

Table 1.1 Summary of device parameters for high performing ternary blend OPV and their corresponding binary systems.

System	V_{OC} [V]	J_{SC} [mA cm^{-2}]	FF [%]	PCE^{max} [%]	Ref.
PTB7:$PC_{71}BM$	0.747	16.96	70.04	9.09	[48]
PTB7:$PC_{71}BM$:DPPEZnPTEH	0.769	18.68	74.89	11.03	[48]
PTB7-Th:$PC_{71}BM$	0.794	17.05	68.60	9.60	[49]
PTB7-Th:$PC_{71}BM$:ASSQ:DPSQ	0.789	17.82	71.7	10.70	[49]
PTB7-Th:$PC_{71}BM$ (thickness 250 nm)	0.771	17.8	50.6	7.07	[50]
PTB7-Th:$PC_{71}BM$:BTR (thickness 250 nm)	0.751	21.4	70.0	11.4	[50]
PTB7-Th:$PC_{71}BM$	0.785	19.43	64.90	10.10	[51]
PTB7-Th:$PC_{71}BM$:DR3TSBDT	0.765	22.63	68.51	12.10	[51]
PTB7-Th:$PC_{71}BM$	0.797	20.70	55.50	9.16	[54]
PTB7-Th:$PC_{71}BM$:p-DTS(FBTTH2)2	0.737	21.67	67.50	10.78	[54]
PTB7-Th:$PC_{71}BM$	0.799	16.70	67.0	9.28	[67]
PTB7-Th:$PC_{71}BM$:ICBA	0.826	17.90	68.8	10.5	[67]
PffBT4T-2OD:$PC_{71}BM$	0.74	17.43	73.93	9.76	[52]
PffBT4T-2OD:$PC_{71}BM$:BTR	0.77	18.28	74.02	10.59	[52]
PDBT-T1:$PC_{71}BM$	0.915	13.24	76.2	9.29	[55]
PDBT-T1:$PC_{71}BM$:ITIC-Th	0.934	15.54	70.5	10.48	[55]
PBDB-T:$PC_{71}BM$	0.92	15.9	65.6	9.6	[56]
PBDB-T:$PC_{71}BM$:ITIC	0.91	17.7	68.3	11.0	[56]
PBDB-T:IDT-2O	0.86	15.70	71.6	9.65	[57]
PBDB-T:IDT-2O: $PC_{71}BM$	0.87	16.80	72.11	10.67	[57]
PBDB-T:IT-M	0.937	16.70	69.0	10.80	[58]
PBDB-T:IT-M:bis[70]PCBM	0.952	17.39	73.7	12.20	[58]
PBDB-T:IT-M	0.930	16.64	71.7	11.10	[60]
PBDB-T:IT-M:N2200	0.934	17.17	75.5	12.10	[60]

Table 1.1 (Continued)

PDOT: $PC_{71}BM$	0.94	13.92	72.9	9.54	[59]
PDOT: $PC_{71}BM$:ITIC	0.96	17.49	66.8	11.21	[59]
PTFB-O:ITIC-Th	0.920	16.8	66	10.2	[61]
PTFB-O:ITIC-Th:EIEC-Th	0.948	16.4	72	11.2	[61]
PTB7-Th:IDTBR:IDFBR	1.03	17.2	60	11.0	[62]
PSTZ:IDIC	0.928	14.7	59.1	8.06	[63]
PSTZ:IDIC:ITIC	0.953	17.4	66.9	11.1	[63]
PBDB-T:IT-M	0.937	17.05	68.1	10.81	[64]
PBDB-T:IT-M:ITCN	0.954	17.67	71.2	12.16	[64]
J52:IT-M	0.843	17.1	65.1	9.4	[65]
J52:IT-M:IEICO	0.847	19.7	66.8	11.1	[65]

1.2 Organic Solution-Processed Light-Emitting Field-Effect Transistors

1.2.1. General Background

Organic semiconductor devices for light-emitting applications have been widely studied for several decades by the research groups and companies worldwide. Some of those devices, such as organic light-emitting diodes (OLED) have now become commercially available. The other technologies are still in the experimental stage in the laboratory setting. Those technologies require more effort to bring the efficiencies up to the levels high enough for any practical applications. One of those technologies is organic light-emitting field-effect transistors (OLEFET).[68,69]

OLEFETs utilize organic semiconductor materials to achieve light-emitting and gate-modulated electrical switching in a single device. OLEFETs may find applications in traditional display and lighting areas, where LEDs are currently used. Modern screens based on LED technologies require a separate layer of logical circuit based on TFT devices to switch individual pixels, and a separate layer of light-emitting LEDs.[70] This brings additional complexity and cost

into the manufacturing process and generates additional sources of failure, thus limiting reliability of the resulting devices. The OLEFET device may solve this issue and boost the development of future generations of light-emitting technologies. In addition to traditional applications, OLEFETS may significantly boost progress in new areas, such as photonic communications and electrically pumped organic lasers.[71–73]

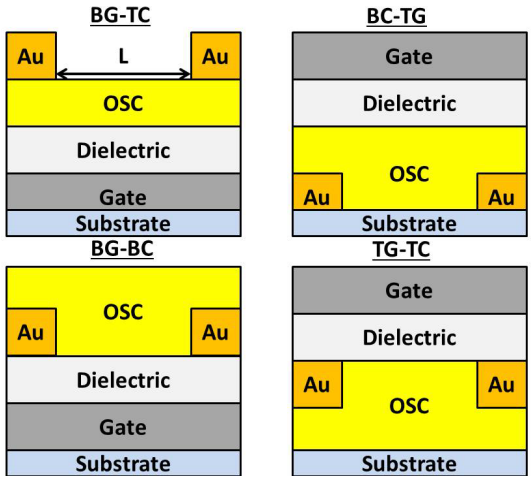

Figure 1.8. OFET devices in bottom-gate top contact (BG-TC), bottom contact top gate (BC-TG), bottom gate bottom contact (BG-BC) and top gate top contact (TG-TC) configurations

1.2.2. Device Components and Mechanism of Operation

Similarly to regular, non-light-emitting OFET, the light-emitting transistors have several main components: gate, gate dielectric, one or multiple layers of organic semiconductor (OSC) and source-drain contacts (Figure 1.8). Gate serves as a 'valve' opening and closing the channel that conducts electrical current between the source and the drain electrodes. When voltage is applied to the gate electrode, the dielectric that separates the gate from the semiconductor becomes polarized. If positive gate voltage is applied then the dielectric surface becomes

positively polarized and vice versa. Polarization of the dielectric interface causes injection of the charge carriers with the charge opposite to that of the interface, meaning that positive gate voltage induces injection of electrons and negative voltage induces injection of holes. The extent of polarization and eventually total induced charge at the interface q_{tot} is described with the equation (1):

$$q_{tot} = C_d \cdot V_G = \frac{\varepsilon\varepsilon_0 A}{t_d} V_G \quad (1)$$

where V_G is gate voltage, C_d capacitance of the dielectric, ε dielectric constant, A area of the device and t_d thickness of the dielectric layer.

When there is no voltage applied between the source and drain electrodes, the gate-induced charges uniformly distributed in the channel. Small applied source-drain voltage induces drift of the charge carriers toward the drain electrode thus forming a conducting channel. Typically, source-drain current appears above certain threshold gate voltage V_{th}, which indicates that part of the gate-induced charges are trapped at the dielectric-semiconductor interface and additional driving force is required to drive the charge carriers.[74] Thus, total mobile charge at the interface q_{mob} is described with a modified version of the equation (1):

$$q_{mob} = \frac{\varepsilon\varepsilon_0 A}{t_d}(V_G - V_{th}) \qquad (2)$$

It is evident from the equation (2) that total charge and eventually current in the channel will be maximized when a thinner dielectric layer with a higher dielectric constant is used and a threshold voltage is low. At the same time, thinner dielectrics may cause significant source-gate

current leakage, which is detrimental to the device performance, therefore balanced approach is necessary.

Rational selection and modifications of dielectric are important steps in designing dielectric-semiconductor interface in OLEFET devices. Care must be taken to induce enough charges at the interface, avoid excessive trapping, ensure low source-gate leakage and facilitate charge transport through the channel. Silicon dioxide (SiO_2) is one of the most popular dielectrics that is used in organic transistor research. It is stable under device operating conditions, has good dielectric strength (~10^7 V cm^{-1}), high enough dielectric constant (3.7-3.9).[75] Reliable synthesis approaches are developed, which make it an ideal material for initial benchmark testing of the devices. Early light-emitting transistors and some modern ones are fabricated using SiO_2 as a dielectric.[76–79] Despite the benefits, one of the critical disadvantages of SiO_2 is the presence of silanol groups (Si-OH) on the surface, which contribute to significant electron trapping and often make electron channel conduction almost impossible.[80] It was observed that the elimination of Si-OH groups, for example by coating another dielectric layer, may increase observed electron mobilities by several orders of magnitude for a wide variety of polymer semiconductors[80]. For example, OLEFET devices with OC_1C_{10}-PPV as an emissive layer and BCB (thermally cross-linked divinyltetramethylsiloxane-bis(benzocyclobutene)), as a buffer dielectric coated on SiO_2, demonstrated ambipolar behavior with relatively balanced electron and hole mobilities of 3×10^{-3} $cm^2V^{-1}s^{-1}$ and 6×10^{-4} $cm^2V^{-1}s^{-1}$, respectively (Figure 1.9a).[81] Transfer characteristics of the devices had typical V-shaped I-V curves, which is indicative of ambipolar behavior (Figure 1.9b). Moreover, light emission was observed from the

middle of the channel and the position of the emissive recombination zone was controlled by gate voltage (Figure 1.9c).

Another way to deal with the presence of silanol groups is by replacing SiO_2 with a different dielectric. A plethora of inorganic and organic materials have been studied for this purpose. Just several examples of inorganic dielectrics that were successfully used in OLEFET devices include tantalum oxide (Ta_2O_5), aluminum oxide (Al_2O_3) and silicon nitride (Si_3N_4)[82,83]. These materials do not completely eliminate the problem of hydroxyl groups on the surface, however their huge advantage is potentially much higher dielectric constant. Some organic polymers have comparable dielectric properties and do not have any hydroxyl groups in their molecular structure. One of the best examples is a family of halogen-containing polymers.

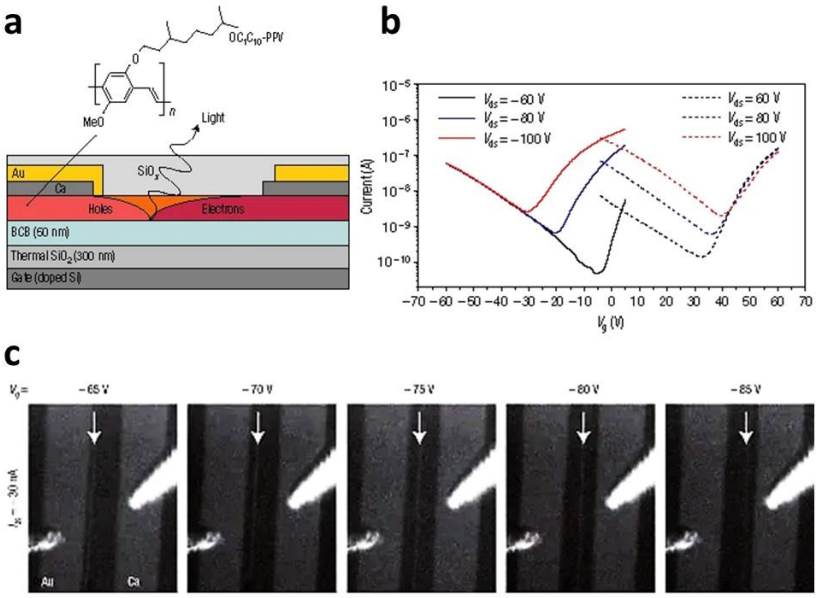

Figure 1.9. a) Schematic illustration of a light-emitting ambipolar transistor with O-C_1C_{10}-PPV as an emissive layer; b) Transfer characteristics of such as transistor at different negative and positive source-drain voltages; c) Digital camera images of light emission from O-C_1C_{10}-PPV transistor at a constant drain current of -30 nA during a V_G sweep. (Reprinted with permission from ref [81]. Copyright 2006 Springer Nature).

A polymer P(VDF-TrFE-CFE), which is fluorinated-chlorinated poly-vinyl based polymer has reported dielectric constant 27-30, which is comparable to the best inorganic dielectrics.[84] At the same time, it can be solution-processed, which is convenient for benchmark thickness control, it does not have any hydroxyl groups in its structure and it is chemically stable in air and under device operating conditions. It has been employed in OLEFET devices and its performance was compared to another widely used organic dielectric PMMA. It was found that devices with the 450 nm layer of P(VDF-TrFE-CFE) had higher EQE at lower voltages compared with devices containing PMMA of the same thickness, 3.3% versus 2.6%, respectively. Moreover, complete turn-on state of devices with P(VDF-TrFE-CFE) was observed at -20V, while for devices with PMMA it was 5 times higher, -100 V.

1.2.3. Hybrid Light-Emitting Field-Effect Transistors

Recently, low-voltage OLEFET devices have been actively studied and reported in the literature. The motivation for this direction of research is twofold. Firstly, elimination of charge trapping and, as a result, higher current densities results in more efficient OLEFETsand may also open new technological horizons, such as electrically pumped organic lasers. Secondly, there are limitations on the amount of power that OLEFET devices may consume to be economically and technologically viable if used in any practical applications. Therefore, the introduction of OLEFETs that are efficient and have low threshold voltage is of great fundamental and practical importance.

Hybrid organic-inorganic LEFET devices showed a great promise in low voltage applications. This kind of devices has semiconducting and light-emitting functions separated in two different materials. The light-emitting function is usually provided by regular organic

fluorescent materials, such as Super Yellow and others. Semiconducting properties are provided by inorganic materials that have to be optically transparent in the spectral region of interest and have high charge carrier mobility. This approach solves the problem of mutually exclusive requirements for light emission and good conductivity in materials when these two functions are combined in a single device. Inorganic materials that are often used for this purpose are n-type semiconductors based on metal oxides and nitrides. For example, zinc-oxynitride (ZnON) has very high electron mobility >120 $cm^2V^{-1}s^{-1}$ and high transparency in the visible region. It was used as a semiconducting electron transporting layer in bottom gate-top contact OLEFET with Super Yellow polymer as a light-emitting layer.[85] Obtained n-type devices had a low threshold voltage of 7.16 V, devices were very bright (3.04×10^4 cd m^{-2}) and had EQE of 0.1% at the highest brightness point. Interestingly, these high results were obtained for devices assembled in quite an unfavorable configuration. Dielectric SiO_2 that was used in this study is not the most effective one and source-drain contacts were symmetrical, i.e. made of the same metal. Authors also studied effect of nature of source-drain contact metal (Al, Ag or Au) on optoelectronic performance of devices as well as the effect of insertion of hole-injecting layer MoO_x. The lowest electron injection threshold voltage and highest electron mobility were obtained for Ag source-drain electrodes. However, no significant light emission was observed in these devices. This result is not surprising since injection of both holes and electrons is required for efficient light emission. In this case a barrier of 2.2 eV for hole injection is too high. Insertion of MoO_x significantly improved hole injection and devices with the highest brightness were obtained for MoO_x/Au electrodes.

Even though ZnON showed very promising results, the semiconductor was deposited by reactive magnetron sputtering process. Alternative, solution-processed inorganic semiconductors for low voltage LEFET devices were reported as well. For example, a solution-processed In_2O_3/ZnO low-dimensional heterojunction system was used as the n-type channel in LEFET devices with Super Yellow as an emissive layer.[86] These devices operated at the gate and source-drain voltages below 10 V, and demonstrated emission with the brightness of 700 cd m^{-2} and EQE at the highest brightness point 0.02%. Even though the device performance parameters appear to be lower than the ones obtained with ZnON, they are actually comparable. For devices with ZnON the highest EQE was observed at around 15 V gate voltage, while devices with In_2O_3/ZnO heterojunction were studied in <10 V regime. There are no reported studies of devices with ZnON in <10 V regime, however based on the graphs depicting brightness vs gate voltage, performance of both types of devices is quite comparable (Figure 1.10).

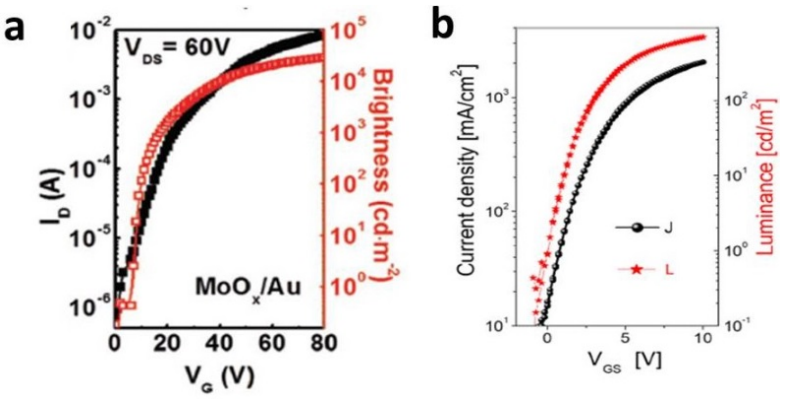

Figure 1.10. Transfer characteristics and brightness curves of LEFET devices with a) ZnON and b) In_2O_3/ZnO semiconducting layers. (Reprinted with permission from ref [85]. Copyright 2019 John Wiley and Sons. Reprinted with permission from ref [86]. Copyright 2018 American Chemical Society).

Most of the LEFET devices operating in low-voltage conditions use n-type inorganic semiconductors for better electrical properties. However, both n- and p-type injection is required for light emission. Improving hole injection may be one of the ways to obtain even more efficient devices. For example, incorporation of a hole transporting material into an emissive layer may be used as one of the approaches. Thus, hole transporting small molecule C_8-BTBT was blended with Super Yellow in hybrid LEFET devices with In_2O_3 as an inorganic semiconductor.[87] Devices with a light-emitting blend had just slightly increased electrical threshold voltage (from 2.0V to 3.5 V), however light turn-on voltage decreased significantly, from 27 V to 2 V. Also, brightness increased for a blend device from 41 to 67 cd m^{-2} and EQE increased from 0.02% to 0.08%. Despite improved hole transport devices worked mostly in the unipolar regime and emission was only observed in the narrow region near the hole injecting electrode.

1.2.4. Device Configurations

Depending on the application, OLEFET device components can be arranged in two different configurations. Devices in staggered configuration have source-drain contacts separated from the conduction channel with a layer of semiconductor, while devices in co-planar configuration, have contacts positioned on the same plane with the channel (Figure 1.8). Devices in staggered configuration have two variations – bottom contact-top gate (BC-TG) and bottom gate-top contact (BG-TC), depending on the position of source-drain contacts and a gate relative to the active layer semiconductor. These two configurations are used in OLEFET devices most widely. Devices in BC-TG have metal contacts typically patterned on the flat glass

surface. The active semiconductor layer, a layer of dielectric and then a gate electrode are coated sequentially. One of the advantages of this configuration is a potential fabrication of devices on light-weight, transparent and flexible substrates. Another advantage is the possibility of modifying bottom contacts by coating interfacial layers or self-assembled monolayers (SAM) with good adhesion to metal electrode. For example, thin layers of ZnO were used as electron injecting layer, coated on top of gold source-drain electrodes in OLEFET devices. Bottom contact configuration is beneficial in this case since the formation of ZnO film requires rather high annealing temperatures (150-200°C), which could potentially degrade organic materials if top contact configuration were used.[88] For example, introduction of ZnO as an electron transporting layer in OLEFET devices with blue F8 as an emissive polymer left hole transport practically unaltered. However, threshold voltage for electron injection was decreased significantly from 68 V to 8 V. Similar effect was observed when green F8BT was used as an emissive layer – threshold voltage for electron injection decreased from 34 V to 5V compared with bare gold devices. Position of the recombination zone was dependent on the gate voltage. Its position in the middle of the channel could be achieved for certain conditions. Even more impressive results were achieved after device optimization. When silver was used as a gate electrode and thickness of PMMA dielectric was optimized, impressive 8.16% EQE were obtained for a single layer F8BT devices with ZnO electron transporting layer.[89]

Another advantage of BC-TG configuration is the possibility to control the surface properties of bottom metal electrodes. For example, when bottom contact electrodes are deposited by vacuum e-beam evaporation technique, surface properties depend on the evaporation rate. Gold films deposited at 0.5 Å s^{-1} rate have larger grain size than the films

deposited at a faster rate of 3 Å s^{-1}. The films with larger grain size have wider flat regions, where dipole of SAM is better aligned and facilitates charge injection into organic semiconductor. As a result, contact resistance decreases from 3100 Ohm cm for devices evaporated at 3 Å s^{-1} rate to 500 Ohm cm for devices evaporated at 0.5 Å s^{-1} rate with the better-aligned surface dipoles.[90]

Devices in BG-TC configuration typically have silicon wafers used as substrates, where doped silicon serves as a gate electrode and it is separated from an organic semiconductor with a layer of dielectric. As an alternative, a glass slide coated with indium-tin oxide (ITO) can be used as a gate. However introduction of materials with high refractive index, such as ITO, limits light outcoupling from the device due to enhanced total internal reflection and waveguide effects.[91]

Unlike staggered configuration, devices in a co-planar configuration have charge injecting source-drain electrodes situated on the same plane with the conducting channel. In this case charge carriers are not required to cross the layer of semiconductor to reach the channel upon their injection. Typically, co-planar devices are assembled in two configurations – bottom gate bottom contact (BG-BC) and top gate top contact (TG-TC). These configurations are rarely used in solution-processed light-emitting transistors due to inability to incorporate additional layers to improve charge injection and transport. However, some success was achieved in BG-BC devices with shorter channel lengths (2-20 μm).[79]

Despite spatial proximity of charge injecting electrodes and conducting channel in co-planar geometry, these devices often demonstrate inferior current-voltage characteristics and

elevated contact resistances, than their staggered analogs.[92] Typically charge injection in co-planar devices happens from the side of the metal electrode, which has thickness of a few tens of nanometers into a narrow accumulation region at the dielectric-semiconductor interface, which is just 2-3 monolayers thick.[93] Injection from the metal electrode's top surface is usually negligible since it is not gate-modulated. This deficiency significantly limits currents due to contact-limited behavior. At the same time, devices in staggered configuration demonstrate much better charge injection, since all the area underneath the source and drain electrodes is gate-modulated and can potentially participate in the process.[94,95]

1.2.5. Factors Affecting Light Emission in OLEFET

The property that distinguishes OLEFET devices from the regular FETs is the ability to emit light when the output current is on. Light emission originates from the radiative recombination of holes and electrons that are simultaneously injected into an organic semiconducting layer. The fundamental properties of materials such as alignment of semiconductor's HOMO and LUMO levels with the work function of the metal electrodes determine efficiency of this injection. The bandgap of the material determines color of emitted light. The electronic coupling and the solid-state structure determine mobility of charge carriers and therefore the position of the recombination zone. The emissive material's fluorescence quantum yield determines maximum possible external quantum efficiency (EQE) of the OLEFET device. Even more complex phenomena are observed when materials harvesting triplet excitons are used, such as TADF emitters or phosphorescent materials, both of which have been successfully used in OLEFETs, however studies on solution-processed devices are scarce.[96–98] In addition to fundamental properties of materials, device engineering plays an important role.

Thus, source-drain contact engineering[99,100], transistor dielectric engineering[101], incorporation of interfacial layers[102–104], incorporation of metal nanoparticles with surface plasmon resonance[105,106] have been previously used to tune the properties of light-emitting devices.

The ideal light-emitting semiconductor needs to have appropriate energy levels to minimize charge injection barriers from metal contacts, it requires high, balanced and, ideally, ambipolar, charge carrier mobility to ensure light emission at the center of the channel. It also needs to have high fluorescence quantum yield. In addition, it is also desirable that the solution processing approach is available in such materials, therefore they have to be soluble in common fast-drying solvents and have good film-forming abilities. All of these parameters have to be carefully fine-tuned to balance optoelectronic processes in the device and achieve most efficient exciton-to-photon conversion. However, one of the challenges of OLEFET optimization is the fact that the requirements mentioned above are often mutually exclusive. For example, the materials demonstrating high charge carrier mobility are required to have high crystallinity, tight molecular packing, and good electronic coupling to ensure efficient intermolecular charge transport. At the same time, the efficient π-π stacking that is crucial for high mobility usually causes fluorescence quenching due to formation of exciplexes/excimers, charge transfer states and other non-radiative decay processes.[107] In addition, making materials soluble usually requires incorporation of bulky alkyl groups in the molecular structure, which hinders molecular stacking and thus can potentially deteriorate electronic coupling and eventually mobility.

Another challenge present in OLEFET devices is achieving balanced charge injection and transport. Unlike regular OFET devices where injection of just a single type of carriers in the channel can provide useful functionality and result in efficient p or n-type field-effect

transistors, the light-emitting devices require the simultaneous injection of both carrier types under the same conditions for radiative recombination to be possible. Taking into account the structure of traditional OFET devices which use the same metal (typically gold) for the source and drain electrodes, it is even harder to have equally effective injection of holes into HOMO of the semiconductor and electrons into LUMO, just because of different barriers. As a consequence, organic FET devices demonstrate more pronounced unipolar p-type behavior, mostly due to better alignment of organic material's HOMOs (typically -5 to -6 eV) with the work function of gold (-5.3 eV).[108] Despite preferential injection of just one type of charge carriers, even unipolar devices demonstrate light-emitting properties.

1.2.6 Unipolar Light-Emitting Transistors

Unipolar p-type FETs have preferential hole transport for gate voltages $V_G<0$ and electron transport for $V_G>0$. For example, when negative voltage is applied to the gate electrode, the dielectric positioned right above the gate becomes polarized. As a result of this polarization, the surface of the dielectric possesses a partial negative charge. The negative polarization facilitates the injection of oppositely charged holes from the grounded source electrode. When negative source-drain voltage is applied across the channel, holes move towards the drain electrode, thus creating a closed circuit and contributing to the output current from the OFET device. At the same time, it was observed that in certain systems, the minority electrons can be injected from the drain electrode into the area of close proximity to the electrode. "Majority" holes and "minority" electrons recombine and light emission is observed near the drain electrodes. Injection of minority electrons is highly inefficient and energetically unfavorable, thus efficiency of exciton-to-photon conversion in such systems is quite low. Light emission

originating from injection of minority charge carriers in unipolar devices was observed both in thermally evaporated small molecule systems and solution-processed polymers.[76,77] Experimental and theoretical studies conducted on these systems showed that non-Ohmic contact present at metal/semiconductor interface allows interfacial electron tunneling from the metal into the semiconductor, which explains observed behavior. This process is facilitated even further in energetically disordered systems, such as conjugated polymers, where injection of minority charge carriers into low energy tail of the density of states (DOS) is possible.[109] Even though, light emission is observed in such devices, brightness is often quite low. Moreover, maximum optical outcoupling efficiency is below 10% for near-electrode emission and up to 30% for the emission occurring in the middle of the channel.[109] Another problem associated with the near-electrode emission is the fact that the size of the emission zone often depends on gate voltage. This means that aperture ratio of the emitting device may change for different ratios of gate and source-drain voltages. This is not compatible with the modern pixelated screen technologies, where pixel size has to be constant. One of the ways to solve this problem is using transparent source or drain electrode. It has constant area and therefore light emission originating from the area underneath this electrode has constant aperture ratio. This kind of device may be described with an equivalent circuit of LED positioned in series with FET. However, in this case LED is not a separate device, but one of the electrodes in FET. These devices possess all the properties of the regular FETs, but have light emission originating from the area underneath one of the semitransparent electrodes rather than in the middle of the FET channel.

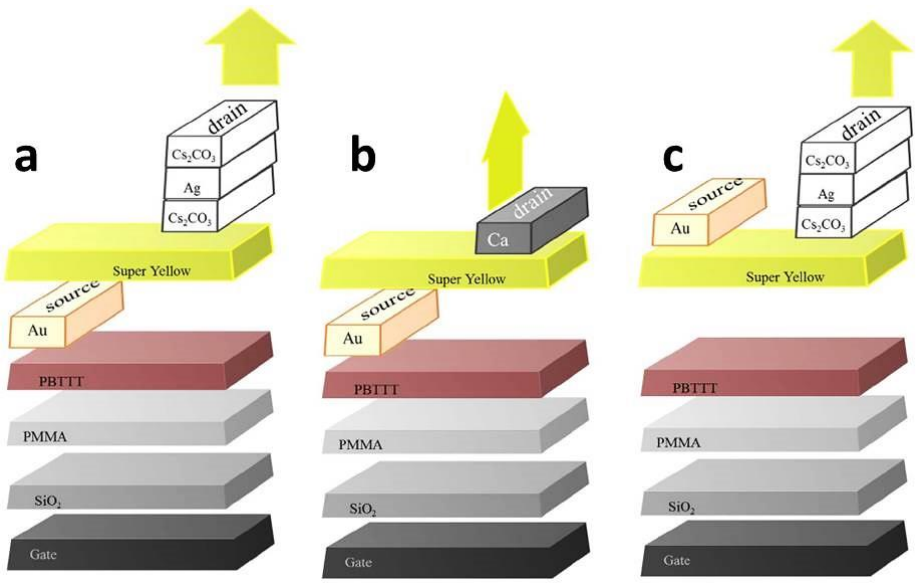

Figure 1.11. a) Device design of pixelated light-emitting transistors using semitransparent drain electrode, b) non-planar light-emitting transistor with conventional Au/Ca source/drain electrodes; c) light-emitting transistor in conventional top contact configuration with a semitransparent drain electrode. (Reprinted from ref [110]. Copyright 2015 Springer Nature licensed under Creative Commons Attribution 4.0 International License).

One of the examples of such a device is OLEFET with Super Yellow as an emissive layer and non-planar asymmetric source-drain electrodes. A layer of gold underneath Super Yellow worked as a source electrode and thin stack of Cs_2CO_3/Ag/Cs_2CO_3 (CAC) as a semitransparent drain electrode.[110] Devices shown in Figure 1.11a exhibit the brightest emission of 1350 cd m^{-2} and EQE of 1% at the brightest point. Light emission happens from the area underneath semitransparent drain electrode and calculated aperture ratio at the brightest point is 24%. Non-planar configuration of source-drain electrodes ensured low contact resistance and better energy level alignment for efficient charge injection. Control devices where drain CAC electrode was replaced with calcium or assembled in planar configuration showed inferior results. EQE of the device with Ca electrode was 0.09% and planar CAC 0.45%. The light was emitted from the edge of the drain electrode in Ca containing device and calculated aperture ratio was only 2.5%.

Similar strategies have been utilized in hybrid LEFET devices. For example, semitransparent MoO_x/Au drain electrodes were used in hybrid devices with solution-processed zinc tin oxide (ZTO) and a series of light-emitting polymers, such as Super Yellow, green F8BT and blue PFO.[111] Non-planar source-drain geometry was used with Al as a source electrode, which was modified with a thin layer of PEIE for more efficient electron injection. Area emission was observed for all three systems, with the Super Yellow being the brightest one – 1330 cd m^{-2} and EQE 0.087%. Specially designed circular source-drain mask allowed authors to achieve a 50% aperture ratio in these hybrid LEFETs, which is much higher than the previously reported results, where regular interdigitated electrodes were used. Device performance with Super Yellow was improved even further when an additional electron injecting layer of Cs_2CO_3 was inserted right underneath the drain electrode (Figure 1.12).[112] Two hybrid solution-processed systems were used in this study – bilayer In_2O_3/ZnO and multilayer In_2O_3/Ga_2O_3/ZnO. Additional Ga_2O_3 layer is used in multilayer stack in order to passivate electron traps present in In_2O_3. Devices with the multilayer semiconductor stack and inserted Cs_2CO_3 showed the best performance. When Cs_2CO_3 is coated on the surface of the oxide semiconductors, the work function is modified from -4.2 eV to -3.7 eV, which is much more favorable for electron injection. Electrons were transported through OFET channel from Al electrode to Cs_2CO_3 and were further injected into organic SY layer where they recombined with holes injected from semitransparent MoO_x/Au electrode. As a result, 1800 cd m^{-2} bright emission with the EQE 0.5% was observed from the area underneath the semitransparent drain electrode. The calculated aperture ratio was 38% and did not depend on the gate voltage.

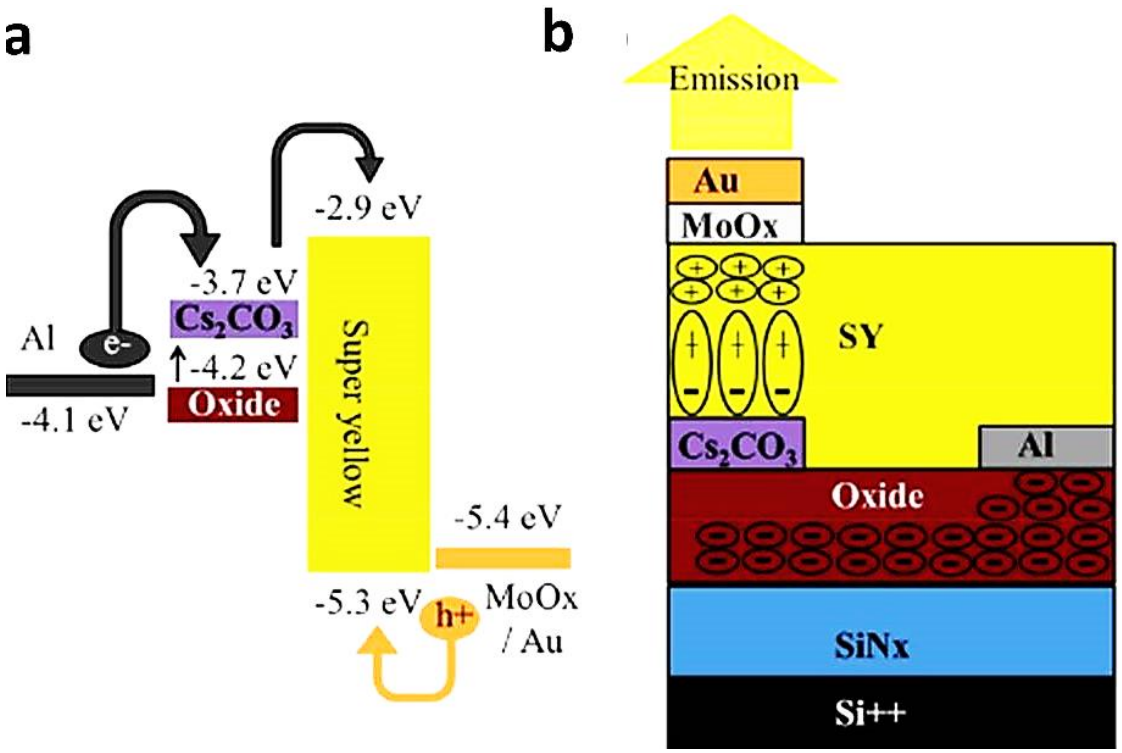

Figure 1.12. a) Energy level diagram and charge injection mechanism hybrid LEFET devices with area emission, b) Schematics of charge injection and light emission in the hybrid LEFET devices. (Reprinted with permission from ref [112]. Copyright 2016 John Wiley and Sons).

1.2.7 Ambipolar Light-Emitting Transistors

The only way to push the recombination zone away from the drain electrode into the middle of the channel is providing high and equal hole and electron injection into the channel, which is realized in truly ambipolar OLEFETs. One of the useful functionalities of ambipolar devices is their ability to exhibit both p and n-type transistor behavior. Under certain conditions and specific ratios of gate voltage V_G, source-drain voltage V_{SD} and threshold voltage V_{th}, both hole and electron accumulation channels exist. For efficient injection of both holes in ambipolar devices V_G-V_{SD} has to be lower than threshold voltage for hole accumulation $V_{th}^{(h)}$, while for

efficient injection of electrons V_G has to be bigger than the threshold voltage for electron accumulation $V_{th}^{(el)}$. Summarizing, conditions for ambipolar charge injection are $(V_G - V_{SD}) > V_{th}^{(h)}$ and $V_G > V_{th}^{(el)}$.[113] When both hole and electron accumulation channels appear in the device, their effective length before recombination, L_h and L_e, respectively, will depend on the relative mobilities. This relationship may be described with an equation (3)[81]

$$\frac{L_h}{L_e} = \frac{\mu_h}{\mu_e} \times \frac{(V_G - V_{th}^{(h)})^2}{(V_G - V_{SD} - V_{th}^{(el)})^2} \quad (3)$$

where L_h is hole accumulation channel length, L_e electron accumulation channel length, μ_h hole FET mobility, μ_e electron FET mobility. It is evident from equation (3) that the position of the recombination zone (L_h/L_e =1 for position at the center of the channel) highly depends on the ratio of hole and electron mobilities in the device. The best results can be achieved when the mobility values are high and equal. Several approaches have been described in the literature to achieve such balance.

Even when balanced ambipolar transport is achieved and recombination happens in the middle of the channel, the width of the recombination zone is often quite narrow. Moreover, the length and position of it in the channel may depend on the applied voltage, which makes the aperture ratio unstable. There have been several attempts to resolve this issue and obtain surface light emission from all the area of the channel. One of the suggested strategies is incorporation of bilayer organic structures as emissive materials in ambipolar OLEFETs. Bilayer structure consisting of fluorene based polymers F8 and F8BT was used in bottom contact-top gate OLEFET devices with symmetric source-drain electrodes made of ITO.[114] Polymers were

coated from solutions in orthogonal solvents in such a way that F8BT formed a lower layer in the device (closer to source-drain electrodes) and F8 was coated on top of it, thus forming upper layer (closer to dielectric). It was observed that light emission happened predominantly near the drain electrode for very high and very low gate voltages, however wide-area emission from the channel was observed for mid-range gate voltages (20-50 V). HOMO and LUMO energy levels of the polymers were aligned in such a way that holes could freely move between two polymers in the bilayer (HOMO offset was 0.1 eV), however electron transfer from F8BT to F8 was somewhat hindered (LUMO offset 0.6 eV), thus F8 acted as an electron blocking layer in the system. Due to the energy barrier, threshold voltage for electron injection into F8 in single layer devices was higher than into F8BT, 46 V versus 20 V, respectively. When gate voltage was slightly larger than the threshold voltage for electron injection into F8BT (region I in Figure 13), hole and electron transport took place in two separate layers – electron transport happened predominantly in F8BT layer, and hole transport happened in F8. Holes and electrons recombine at the interface between F8BT and F8 thus resulting in wide area emission. When gate voltage increases (regions II and III in Figure 1.13), electron transport gradually shifts to F8 layer thus resulting in recombination and eventually light emission taking place in the narrow area near the drain electrode.

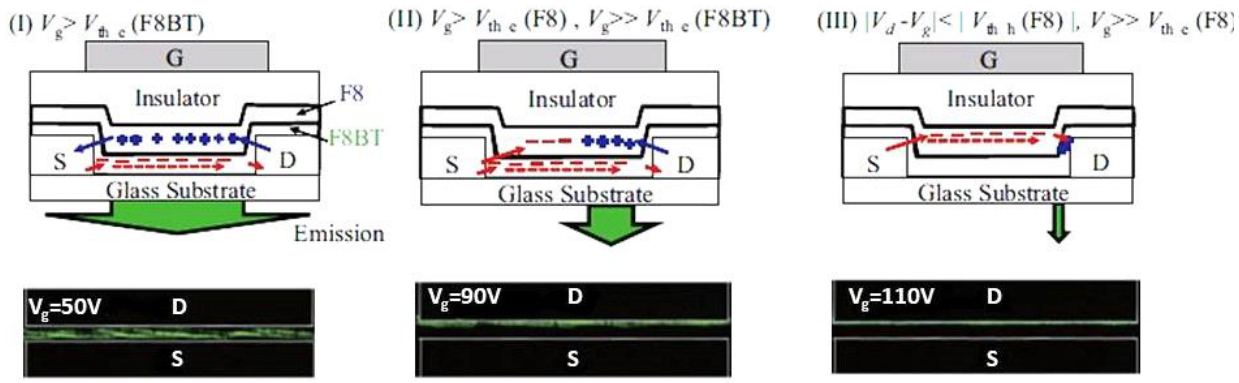

Figure 1.13. a) Schematic representations of the bilayer device showing the expected hole and electron transport and location of the light-generation area in regions I, II and III. (Reprinted with permission from ref[114]. Copyright 2014 Elsevier).

The results described in this example were obtained using OLEFET devices with two polymer films spin-coated sequentially from orthogonal solvents – F8BT was coated from xylene and F8 from cyclohexane. However, this idea has also been explored using other solution-based film coating methods, such as contact printing with PDMS stamp and floating film transfer method (FTM). Devices with F8 layer printed on F8BT had very similar optoelectronic properties to spin-coated devices, however, they exhibited more uniform light emission, possibly due to improved uniformity in the film thickness.[114] Floating film transfer method was used to study effects of polymer chain orientation on OLEFET optoelectronic properties in bilayer devices. A series of devices was fabricated where F8 and F8BT films of varying thickness were coated on top of one another and polymer chains had preferential alignment perpendicular or parallel to the charge transport direction in the channel.[115] It was found that thickness of electron blocking F8 is of great importance and wide area emission was only obtained for devices with the thickness of F8 around 80 nm. In addition, optoelectronic properties of devices improved tremendously when both F8BT and F8 chains had preferential

orientation along the channel – more balanced hole and electron transport was achieved and EQE increased almost 3 times, from 0.6% to 1.5% compared to films without alignment. Interestingly, these results are consistent with similar studies for unipolar OLEFETs where preferential alignment of semiconductor polymer chains in BG-TC devices was achieved by scratching the surface of the dielectric in order to form grooves approximately 5 nm deep, 100 nm wide and 1-2 μm long.[116] These grooves induced parallel preferential orientation of DPP-DTT, a hole transporting polymer that was dip-coated on top of the dielectric to form a semiconducting layer in the device. Observed source-drain currents were 10 times higher along the direction of the grooves, compared to the perpendicular one. Performance of light-emitting devices with Super Yellow emissive layer spin-coated on top of DPP-DTT improved tremendously as well – EQE increased from 0.04% for a device without alignment to 0.4%, and brightness increased from 900 cd m^{-2} to 29000 cd m^{-2}.

1.2.8 OLEFET Summary and Outlook

Organic optoelectronics has experienced a tremendous boost in recent decades. Nowadays every traditional device based on inorganic semiconductors has its organic alternative, which sometimes is even more efficient than the original device. Fundamental properties of materials, as well as device engineering approaches, are studied for organic solar cells, light-emitting diodes, memory devices, lasers, light-emitting transistors and many other optoelectronic technologies by the research groups worldwide. Despite all the progress in the field of organic optoelectronics in general, organic light-emitting transistors, in particular, are still relatively undeveloped. Mutually exclusive requirements for efficient charge transport and efficient light emission are one of the obstacles hindering progress in the field. Most of the materials for

solution-processed OLEFET devices were directly adopted from OLEDs, however this approach is not ideal. Typically materials for OLED do not require high mobilities. Charge carriers in OLED have to travel the distance of only tens of nanometers through the active layer film, unlike transistors, where charge carriers path may be thousands times longer. As a result, OLEFET devices are in general much less efficient than OLEDs, with some rare exceptions. Nowadays, state of the art OLED devices can easily reach EQEs of 25-30% for a wide variety of materials, while the most efficient solution-processed OLEFET was reported back in 2012 and had EQE of 8%, which is 3 times lower, and it was reported only for one polymer F8BT. Analysis of recent literature shows that more research is required to bring efficiencies of OLEFET devices to the levels at least comparable with the OLEDs. Possible directions of research may include development of highly emissive ambipolar semiconductors where light-emitting and charge-transporting properties combined in one material. As an alternative, these two properties can be separated in two different materials, however good integration of both functions in a single device has to be ensured. Spin related processes are still relatively unexplored in OLEFET devices. Even though TADF emitters and phosphorescent materials have been reported in light-emitting transistors, these studies are scarce. In addition, radical emitters that were reported as one of the highly promising materials that do not follow typical singlet-triplet statistics in OLEDs have not been studied for light-emitting transistor applications at all.[117] In addition to fundamental material properties, there is still room for improvement in device engineering. For example, metal nanoparticles have been reported to improve fluorescence in organic polymers, however only a handful of reports can be found describing studies on light-emitting transistor devices incorporating the nanoparticles, and most of these

reports are for near-IR OLEFETs. Experimental studies alone are not enough to boost progress in the field. More effort is required in theoretical research as well. There is still lack of understanding of charge transport, recombination and light emission in multilayer transistor devices and theoretical guidelines for design of efficient organic materials for OLEFET applications are not reliable.

1.3 References

(1) Ostroverkhova, O. Organic Optoelectronic Materials: Mechanisms and Applications. *Chem. Rev.* **2016**, *116*, 13279–13412.

(2) García de Arquer, F. P.; Armin, A.; Meredith, P.; Sargent, E. H. Solution-Processed Semiconductors for next-Generation Photodetectors. *Nat. Rev. Mater.* **2017**, *2*, 16100.

(3) Jansen-van Vuuren, R. D.; Armin, A.; Pandey, A. K.; Burn, P. L.; Meredith, P. Organic Photodiodes: The Future of Full Color Detection and Image Sensing. *Adv. Mater.* **2016**, *28*, 4766–4802.

(4) Hussain, A. M.; Hussain, M. M. CMOS-Technology-Enabled Flexible and Stretchable Electronics for Internet of Everything Applications. *Adv. Mater.* **2016**, *28*, 4219–4249.

(5) Chen, X.; Liu, X.; Burgers, M. a; Huang, Y.; Bazan, G. C. Green-Solvent-Processed Molecular Solar Cells. *Angew. Chem. Int. Ed. Engl.* **2014**, 14378–14381.

(6) Zhao, J.; Li, Y.; Yang, G.; Jiang, K.; Lin, H.; Ade, H.; Ma, W.; Yan, H. Efficient Organic Solar Cells Processed from Hydrocarbon Solvents. *Nat. Energy* **2016**, *1*, 15027.

(7) Diao, Y.; Shaw, L.; Bao, Z.; Mannsfeld, S. C. B. Morphology Control Strategies for Solution-Processed Organic Semiconductor Thin Films. *Energy Environ. Sci.* **2014**, *7*, 2145–2159.

(8) Richter, L. J.; DeLongchamp, D. M.; Amassian, A. Morphology Development in Solution-Processed Functional Organic Blend Films: An In Situ Viewpoint. *Chem. Rev.* **2017**, *117*, 6332–6366.

(9) Chueh, C.-C.; Li, C.-Z.; Jen, A. K.-Y. Recent Progress and Perspective in Solution-Processed Interfacial Materials for Efficient and Stable Polymer and Organometal Perovskite Solar Cells. *Energy Environ. Sci.* **2015**, *8*, 1160–1189.

(10) Torabi, S.; Jahani, F.; Van Severen, I.; Kanimozhi, C.; Patil, S.; Havenith, R. W. a.; Chiechi, R. C.; Lutsen, L.; Vanderzande, D. J. M.; Cleij, T. J.; *et al.* Strategy for Enhancing the Dielectric Constant of Organic Semiconductors Without Sacrificing Charge Carrier Mobility and Solubility. *Adv. Funct. Mater.* **2015**, *25*, 150–157.

(11) Cho, N.; Schlenker, C. W.; Knesting, K. M.; Koelsch, P.; Yip, H. L.; Ginger, D. S.; Jen, A. K. Y. High-Dielectric Constant Side-Chain Polymers Show Reduced Non-Geminate Recombination in Heterojunction Solar Cells. *Adv. Energy Mater.* **2014**, *4*, 1301857.

(12) Armin, A.; Stoltzfus, D. M.; Donaghey, J. E.; Clulow, A. J.; Nagiri, R. C. R.; Burn, P. L.; Gentle, I. R.; Meredith, P. Engineering Dielectric Constants in Organic Semiconductors. *J. Mater. Chem. C* **2017**, *5*, 3736–3747.

(13) Clarke, T. M.; Durrant, J. R. Charge Photogeneration in Organic Solar Cells. *Chem. Rev.* **2010**, *110*, 6736–6767.

(14) Yu, G.; Gao, J.; Hummelen, J. C.; Wudl, F.; Heeger, A. J. Polymer Photovoltaic Cells : Enhanced Efficiencies via a Network of Internal Heterojunctions. *Science (80-.).* **1995**, *270*, 1789–1791.

(15) Liang, Y.; Xiao, S.; Feng, D.; Yu, L. Control in Energy Levels of Conjugated Polymers for Photovoltaic Application †. *J. Phys. Chem. C* **2008**, *112*, 7866–7871.

(16) Liang, Y.; Yu, L. A New Class of Semiconducting Polymers for Bulk Heterojunction Solar Cells with Exceptionally High Performance. *Acc. Chem. Res.* **2010**, *43*, 1227–1236.

(17) Lu, L.; Zheng, T.; Wu, Q.; Schneider, A. M.; Zhao, D.; Yu, L. Recent Advances in Bulk Heterojunction Polymer Solar Cells. *Chem. Rev.* **2015**, *115*, 12666–12731.

(18) Collado-Fregoso, E.; Boufflet, P.; Fei, Z.; Gann, E.; Ashraf, S.; Li, Z.; McNeill, C. R.; Durrant, J. R.; Heeney, M. Increased Exciton Dipole Moment Translates into Charge-Transfer Excitons in Thiophene-Fluorinated Low-Bandgap Polymers for Organic Photovoltaic Applications. *Chem. Mater.* **2015**, *27*, 7934–7944.

(19) Rolczynski, B. S.; Szarko, J. M.; Son, H. J.; Yu, L.; Chen, L. X. Effects of Exciton Polarity in Charge-Transfer Polymer/PCBM Bulk Heterojunction Films. *J. Phys. Chem. Lett.* **2014**, *5*, 1856–1863.

(20) Liang, C.; Wang, Y.; Li, D.; Ji, X.; Zhang, F.; He, Z. Modeling and Simulation of Bulk Heterojunction Polymer Solar Cells. *Sol. Energy Mater. Sol. Cells* **2014**, *127*, 67–86.

(21) Zhugayevych, A.; Tretiak, S. Theoretical Description of Structural and Electronic Properties of Organic Photovoltaic Materials. *Annu. Rev. Phys. Chem.* **2014**, *66*, 305–330.

(22) Treat, N. D.; Chabinyc, M. L. Phase Separation in Bulk Heterojunctions of Semiconducting Polymers and Fullerenes for Photovoltaics. *Annu. Rev. Phys. Chem.* **2014**, *65*, 59–81.

(23) Bartelt, J. a.; Douglas, J. D.; Mateker, W. R.; Labban, A. El; Tassone, C. J.; Toney, M. F.; Fréchet, J. M. J.; Beaujuge, P. M.; McGehee, M. D. Controlling Solution-Phase Polymer Aggregation with Molecular Weight and Solvent Additives to Optimize Polymer-Fullerene Bulk Heterojunction Solar Cells. *Adv. Energy Mater.* **2014**, *4*, 1–11.

(24) Collins, B. A.; Li, Z.; Tumbleston, J. R.; Gann, E.; Mcneill, C. R.; Ade, H. Absolute Measurement of Domain Composition and Nanoscale Size Distribution Explains Performance in PTB7:PC71bm Solar Cells. *Adv. Energy Mater.* **2013**, *3*, 65–74.

(25) Huang, Y.; Kramer, E. J.; Heeger, A. J.; Bazan, G. C. Bulk Heterojunction Solar Cells: Morphology and Performance Relationships. *Chem. Rev.* **2014**, *114*, 7006–8043.

(26) Lin, J. D. a.; Mikhnenko, O. V.; Chen, J.; Masri, Z.; Ruseckas, A.; Mikhailovsky, A.; Raab, R. P.; Liu, J.; Blom, P. W. M.; Loi, M. A.; *et al.* Systematic Study of Exciton Diffusion Length in Organic Semiconductors by Six Experimental Methods. *Mater. Horizons* **2014**, *1*, 280–285.

(27) Gordon J. Hedley, Alexander J. Ward, Alexander Alekseev, Calvyn T. Howells, Emiliano R. Martins, Luis A. Serrano, Graeme Cooke, A. R. & I. D. W. S. Determining the Optimum Morphology in High-Performance Polymer-Fullerene Organic Photovoltaic Cells. *Nat. Commun.* **2013**, *4*, 2867.

(28) Huggins, M. L. Solutions of Long Chain Compounds. *J. Chem. Phys.* **1941**, *9*, 440–440.

(29) Flory, P. J. Thermodynamics of High Polymer Solutions. *J. Chem. Phys.* **1941**, *9*, 660–660.

(30) Cheng, S. Z. D. *Phase Transitions in Polymers: The Role of Metastable States*; 1st ed.; Elsevier Science S.A., 2008.

(31) Garcia-Ojalvo, J.; Lacasta, A. M.; Sancho, J. M.; Toral, R. Phase Separation Driven by External Fluctuations. *Eur. Lett.* **1998**, *42*, 125.

(32) Dou, L.; You, J.; Hong, Z.; Xu, Z.; Li, G.; Street, R. a; Yang, Y. 25Th Anniversary Article: A Decade of Organic/Polymeric Photovoltaic Research. *Adv. Mater.* **2013**, *25*, 6642–6671.

(33) Lu, L.; Yu, L. Understanding Low Bandgap Polymer PTB7 and Optimizing Polymer Solar Cells Based on It. *Adv. Mater.* **2014**, *26*, 4413–4430.

(34) Lyons, B. P.; Clarke, N.; Groves, C. The Relative Importance of Domain Size, Domain Purity and Domain Interfaces to the Performance of Bulk-Heterojunction Organic Photovoltaics. *Energy Environ. Sci.* **2012**, *5*, 7657.

(35) Lakhwani, G.; Rao, A.; Friend, R. H. Bimolecular Recombination in Organic Photovoltaics. *Annu. Rev. Phys. Chem.* **2014**, *65*, 557–581.

(36) Müller, C.; Ferenczi, T. A. M.; Campoy-Quiles, M.; Frost, J. M.; Bradley, D. D. C.;

Smith, P.; Stingelin-Stutzmann, N.; Nelson, J. Binary Organic Photovoltaic Blends: A Simple Rationale for Optimum Compositions. *Adv. Mater.* **2008**, *20*, 3510–3515.

(37) Wolfer, P.; Schwenn, P. E.; Pandey, A. K.; Fang, Y.; Stingelin, N.; Burn, P. L.; Meredith, P. Identifying the Optimum Composition in Organic Solar Cells Comprising Non-Fullerene Electron Acceptors. *J. Mater. Chem. A* **2013**, *1*, 5989–5995.

(38) Stoltzfus, D. M.; Clulow, A. J.; Jin, H.; Burn, P. L.; Gentle, I. R. Impact of Dimerization on Phase Separation and Crystallinity in Bulk Heterojunction Films Containing Non-Fullerene Acceptors. *Macromolecules* **2016**, *49*, 4404–4415.

(39) Ye, L.; Hu, H.; Ghasemi, M.; Wang, T.; Collins, B. A.; Kim, J. H.; Jiang, K.; Carpenter, J. H.; Li, H.; Li, Z.; *et al.* Quantitative Relations between Interaction Parameter, Miscibility and Function in Organic Solar Cells. *Nat. Mater.* **2018**, *17*, 253–260.

(40) van Franeker, J. J.; Turbiez, M.; Li, W.; Wienk, M. M.; Janssen, R. a. J. A Real-Time Study of the Benefits of Co-Solvents in Polymer Solar Cell Processing. *Nat. Commun.* **2015**, *6*, 6229.

(41) de Zerio, A. D.; Müller, C. Glass Forming Acceptor Alloys for Highly Efficient and Thermally Stable Ternary Organic Solar Cells. *Adv. Energy Mater.* **2018**, *1702741*, 1–18.

(42) An, Q.; Zhang, F.; Zhang, J.; Tang, W.; Deng, Z.; Hu, B. Versatile Ternary Organic Solar Cells: A Critical Review. *Energy Environ. Sci.* **2016**, *9*, 281–322.

(43) Savoie, B. M.; Dunaisky, S.; Marks, T. J.; Ratner, M. a. The Scope and Limitations of Ternary Blend Organic Photovoltaics. *Adv. Energy Mater.* **2015**, *5*, 1400891.

(44) Lu, L.; Kelly, M. A.; You, W.; Yu, L. Status and Prospects for Ternary Organic Photovoltaics. *Nat. Photonics* **2015**, *9*, 491–500.

(45) Li, H.; Lu, K.; Wei, Z. Polymer/Small Molecule/Fullerene Based Ternary Solar Cells. *Adv. Energy Mater.* **2017**, *7*, 1602540.

(46) Zhou, N.; Dudnik, A. S.; Li, T. I. N. G.; Manley, E. F.; Aldrich, T. J.; Guo, P.; Liao, H.-C.; Chen, Z.; Chen, L. X.; Chang, R. P. H.; *et al.* All-Polymer Solar Cell Performance Optimized via Systematic Molecular Weight Tuning of Both Donor and Acceptor Polymers. *J. Am. Chem. Soc.* **2016**, *138*, 1240–1251.

(47) Xiao, L.; Gao, K.; Zhang, Y.; Chen, X.; Hou, L.; CAO, Y.; Peng, X. A Complementary Absorption Small Molecule for Efficient Ternary Organic Solar Cells. *J. Mater. Chem. A* **2016**, *4*, 5288–5293.

(48) Nian, L.; Gao, K.; Liu, F.; Kan, Y.; Jiang, X.; Liu, L.; Xie, Z.; Peng, X.; Russell, T. P.; Ma, Y. 11% Efficient Ternary Organic Solar Cells with High Composition Tolerance via Integrated Near-IR Sensitization and Interface Engineering. *Adv. Mater.* **2016**, *28*, 8184–8190.

(49) Goh, T.; Huang, J. S.; Yager, K. G.; Sfeir, M. Y.; Nam, C. Y.; Tong, X.; Guard, L. M.; Melvin, P. R.; Antonio, F.; Bartolome, B. G.; *et al.* Quaternary Organic Solar Cells Enhanced by Cocrystalline Squaraines with Power Conversion Efficiencies >10%. *Adv. Energy Mater.* **2016**, *6*, 1600660.

(50) Zhang, G.; Zhang, K.; Yin, Q.; Jiang, X.; Zhang, G.; Zhang, K.; Yin, Q.; Jiang, X.; Wang, Z.; Xin, J.; *et al.* High-Performance Ternary Organic Solar Cell Enabled by a Thick Active Layer Containing a Liquid Crystalline Small Molecule Donor. *J. Am. Chem. Soc.* **2017**, *139*, 2387–2395.

(51) Kumari, T.; Lee, S. M.; Kang, S.-H.; Chen, S.; Yang, C. Ternary Solar Cells with a Mixed Face-on and Edge-on Orientation Enable an Unprecedented Efficiency of 12.1%. *Energy Environ. Sci.* **2017**, *10*, 258–265.

(52) Xiao, M.; Zhang, K.; Jin, Y.; Yin, Q.; Zhong, W.; Huang, F.; Cao, Y. Low Temperature Processed High-Performance Thick Film Ternary Polymer Solar Cell with Enhanced Stability. *Nano Energy* **2018**, *48*, 53–62.

(53) Zhang, J.; Zhang, Y.; Fang, J.; Lu, K.; Wang, Z.; Ma, W.; Wei, Z. Conjugated Polymer-Small Molecule Alloy Leads to High Efficient Ternary Organic Solar Cells. *J. Am. Chem. Soc.* **2015**.

(54) Zhang, J.; Zhao, Y.; Fang, J.; Yuan, L.; Xia, B.; Wang, G.; Wang, Z.; Zhang, Y.; Ma, W.; Yan, W.; *et al.* Enhancing Performance of Large-Area Organic Solar Cells with Thick Film via Ternary Strategy. *Small* **2017**, *13*, 1–8.

(55) Liu, T.; Xue, X.; Huo, L.; Sun, X.; An, Q.; Zhang, F.; Russell, T. P.; Liu, F.; Sun, Y. Highly Efficient Parallel-Like Ternary Organic Solar Cells. *Chem. Mater.* **2017**, *29*, 2914–2920.

(56) Bi, P.; Xiao, T.; Yang, X.; Niu, M.; Wen, Z.; Zhang, K.; Qin, W.; So, S. K.; Lu, G.; Hao, X.; *et al.* Regulating the Vertical Phase Distribution by Fullerene-Derivative in High Performance Ternary Organic Solar Cells. *Nano Energy* **2018**, *46*, 81–90.

(57) Zhang, C.; Feng, S.; Liu, Y.; Ming, S.; Lu, H.; Ma, D.; Xu, X.; Wu, Y.-Z.; Bo, Z. High Efficiency Ternary Polymer Solar Cells Based on a Fused Pentacyclic Electron Acceptor. *J. Mater. Chem. A* **2018**, *6*, 6854–6859.

(58) Zhao, W.; Li, S.; Zhang, S.; Liu, X.; Hou, J. Ternary Polymer Solar Cells Based on Two Acceptors and One Donor for Achieving 12.2% Efficiency. *Adv. Mater.* **2017**, *29*, 1604059.

(59) Zhang, T.; Zhao, X.; Yang, D.; Tian, Y.; Yang, X. Ternary Organic Solar Cells with >11% Efficiency Incorporating Thick Photoactive Layer and Nonfullerene Small Molecule Acceptor. *Adv. Energy Mater.* **2018**, *8*, 1–9.

(60) An, Q.; Zhang, F.; Gao, W.; Sun, Q.; Zhang, M.; Yang, C.; Zhang, J. High-Efficiency and

Air Stable Fullerene-Free Ternary Organic Solar Cells. *Nano Energy* **2018**, *45*, 177–183.

(61) Jiang, K.; Zhang, G.; Yang, G.; Zhang, J.; Li, Z.; Ma, T.; Hu, H.; Ma, W.; Ade, H.; Yan, H. Multiple Cases of Efficient Nonfullerene Ternary Organic Solar Cells Enabled by an Effective Morphology Control Method. *Adv. Energy Mater.* **2018**, *8*, 1701370.

(62) Baran, D.; Ashraf, R. S.; Hanifi, D. A.; Abdelsamie, M.; Gasparini, N.; Röhr, J. A.; Holliday, S.; Wadsworth, A.; Lockett, S.; Neophytou, M.; *et al.* Reducing the Efficiency-Stability-Cost Gap of Organic Photovoltaics with Highly Efficient and Stable Small Molecule Acceptor Ternary Solar Cells. *Nat. Mater.* **2017**, *16*, 363–369.

(63) Su, W.; Fan, Q.; Guo, X.; Meng, X.; Bi, Z.; Ma, W.; Zhang, M.; Li, Y. Two Compatible Nonfullerene Acceptors with Similar Structures as Alloy for Efficient Ternary Polymer Solar Cells. *Nano Energy* **2017**, *38*, 510–517.

(64) Jiang, W.; Yu, R.; Liu, Z.; Peng, R.; Mi, D.; Hong, L.; Wei, Q.; Hou, J.; Kuang, Y.; Ge, Z. Ternary Nonfullerene Polymer Solar Cells with 12.16% Efficiency by Introducing One Acceptor with Cascading Energy Level and Complementary Absorption. *Adv. Mater.* **2018**, *30*, 1–7.

(65) Yu, R.; Zhang, S.; Yao, H.; Guo, B.; Li, S.; Zhang, H.; Zhang, M.; Hou, J. Two Well-Miscible Acceptors Work as One for Efficient Fullerene-Free Organic Solar Cells. *Adv. Mater.* **2017**, *29*, 1700437.

(66) Zhang, M.; Gao, W.; Zhang, F.; Mi, Y.; Wang, W.; An, Q.; Wang, J.; Ma, X.; Miao, J.; Hu, Z.; *et al.* Efficient Ternary Non-Fullerene Polymer Solar Cells with PCE of 11.92% and FF of 76.5%. *Energy Environ. Sci.* **2018**, *11*, 841–849.

(67) Cheng, P.; Yan, C.; Wu, Y.; Wang, J.; Qin, M.; An, Q.; Cao, J.; Huo, L.; Zhang, F.; Ding, L.; *et al.* Alloy Acceptor: Superior Alternative to PCBM toward Efficient and Stable Organic Solar Cells. *Adv. Mater.* **2016**, *28*, 8021–8028.

(68) Liu, C.-F.; Liu, X.; Lai, W.-Y.; Huang, W. Organic Light-Emitting Field-Effect Transistors: Device Geometries and Fabrication Techniques. *Adv. Mater.* **2018**, *1802466*, 1802466.

(69) Zhang, C.; Chen, P.; Hu, W. Organic Light-Emitting Transistors: Materials, Device Configurations, and Operations. *Small* **2016**, *12*, 1252–1294.

(70) Sirringhaus, H. 25th Anniversary Article: Organic Field-Effect Transistors: The Path beyond Amorphous Silicon. *Adv. Mater.* **2014**, *26*, 1319–1335.

(71) Clark, J.; Lanzani, G. Organic Photonics for Communications. *Nat. Photonics* **2010**, *4*, 438–446.

(72) Kuehne, A. J. C.; Gather, M. C. Organic Lasers: Recent Developments on Materials, Device Geometries, and Fabrication Techniques. *Chem. Rev.* **2016**, *116*, 12823–12864.

(73) Gwinner, M. C.; Khodabakhsh, S.; Song, M. H.; Schweizer, H.; Giessen, H.; Sirringhaus, H. Integration of a Rib Waveguide Distributed Feedback Structure into a Light-Emitting Polymer Field-Effect Transistor. *Adv. Funct. Mater.* **2009**, *19*, 1360–1370.

(74) Sirringhaus, H. Device Physics of Solution-Processed Organic Field-Effect Transistors. *Adv. Mater.* **2005**, *17*, 2411–2425.

(75) Klein, N.; Gafni, H. The Maximum Dielectric Strength of Thin Silicon Oxide Films. *IEEE Trans. Electron Devices* **1966**, *ED-13*, 281–289.

(76) Ahles, M.; Hepp, A.; Schmechel, R.; Von Seggern, H. Light Emission from a Polymer Transistor. *Appl. Phys. Lett.* **2004**, *84*, 428–430.

(77) Santato, C.; Capelli, R.; Loi, M. A.; Murgia, M.; Cicoira, F.; Roy, V. A. L.; Stallinga, P.; Zamboni, R.; Rost, C.; Karg, S. F.; *et al.* Tetracene-Based Organic Light-Emitting Transistors: Optoelectronic Properties and Electron Injection Mechanism. *Synth. Met.* **2004**, *146*, 329–334.

(78) Rost, C.; Karg, S.; Riess, W.; Loi, M. A.; Murgia, M.; Muccini, M. Ambipolar Light-Emitting Organic Field-Effect Transistor. *Appl. Phys. Lett.* **2004**, *85*, 1613–1615.

(79) Hou, L.; Zhang, X.; Cotella, G. F.; Carnicella, G.; Herder, M.; Schmidt, B. M.; Pätzel, M.; Hecht, S.; Cacialli, F.; Samorì, P. Optically Switchable Organic Light-Emitting Transistors. *Nat. Nanotechnol.* **2019**, *14*, 347–353.

(80) Chua, L.-L.; Zaumseil, J.; Chang, J.-F.; Ou, E. C.-W.; Ho, P. K.-H.; Sirringhaus, H.; Friend, R. H. General Observation of -Type Field-Effect Behavior in Organic Semiconductors. *Nature* **2005**, *434*, 194–199.

(81) Zaumseil, J.; Friend, R. H.; Sirringhaus, H. Spatial Control of the Recombination Zone in an Ambipolar Light-Emitting Organic Transistor. *Nat. Mater.* **2006**, *5*, 69–74.

(82) Ma, T. P. Making Silicon Nitride Film a Viable Gate Dielectric. *IEEE Trans. Electron Devices* **1998**, *45*, 680–690.

(83) Facchetti, A.; Yoon, M. H.; Marks, T. J. Gate Dielectrics for Organic Field-Effect Transistors: New Opportunities for Organic Electronics. *Adv. Mater.* **2005**, *17*, 1705–1725.

(84) Soldano, C.; D'Alpaos, R.; Generali, G. Highly Efficient Red Organic Light-Emitting Transistors (OLETs) on High-k Dielectric. *ACS Photonics* **2017**, *4*, 800–805.

(85) Park, Y. J.; Song, A. R.; Walker, B.; Seo, J. H.; Chung, K. B. Hybrid ZnON–Organic Light Emitting Transistors with Low Threshold Voltage <5 V. *Adv. Opt. Mater.* **2019**, *7*, 1–6.

(86) Chaudhry, M. U.; Tetzner, K.; Lin, Y. H.; Nam, S.; Pearson, C.; Groves, C.; Petty, M. C.; Anthopoulos, T. D.; Bradley, D. D. C. Low-Voltage Solution-Processed Hybrid Light-

Emitting Transistors. *ACS Appl. Mater. Interfaces* **2018**, *10*, 18445–18449.

(87) Abbas, M.; Ablat, A.; Kyndiah, A.; Bachelet, A.; Takimiya, K.; Hirsch, L.; Fasquel, S. Low Optical Turn-on Voltage in Solution Processed Hybrid Light Emitting Transistor. *Appl. Phys. Lett.* **2019**, *115*, 023301.

(88) Gwinner, M. C.; Vaynzof, Y.; Banger, K. K.; Ho, P. K. H.; Friend, R. H.; Sirringhaus, H. Solution-Processed Zinc Oxide as High-Performance Air-Stable Electron Injector in Organic Ambipolar Light-Emitting Field-Effect Transistors. *Adv. Funct. Mater.* **2010**, *20*, 3457–3465.

(89) Gwinner, M. C.; Kabra, D.; Roberts, M.; Brenner, T. J. K.; Wallikewitz, B. H.; McNeill, C. R.; Friend, R. H.; Sirringhaus, H. Highly Efficient Single-Layer Polymer Ambipolar Light-Emitting Field-Effect Transistors. *Adv. Mater.* **2012**, *24*, 2728–2734.

(90) Lamport, Z. A.; Barth, K. J.; Lee, H.; Gann, E.; Engmann, S.; Chen, H.; Guthold, M.; McCulloch, I.; Anthony, J. E.; Richter, L. J.; *et al.* A Simple and Robust Approach to Reducing Contact Resistance in Organic Transistors. *Nat. Commun.* **2018**, *9*, 5130.

(91) Meerheim, R.; Furno, M.; Hofmann, S.; Lüssem, B.; Leo, K. Quantification of Energy Loss Mechanisms in Organic Light-Emitting Diodes. *Appl. Phys. Lett.* **2010**, *97*, 253305.

(92) Richards, T.; Sirringhaus, H. Bias-Stress Induced Contact and Channel Degradation in Staggered and Coplanar Organic Field-Effect Transistors. *Appl. Phys. Lett.* **2008**, *92*, 90–93.

(93) Koopman, W. W. A.; Toffanin, S.; Natali, M.; Troisi, S.; Capelli, R.; Biondo, V.; Stefani, A.; Muccini, M. Mapping of Charge Distribution in Organic Field-Effect Transistors by Confocal Photoluminescence Electromodulation Microscopy. *Nano Lett.* **2014**, *14*, 1695–1700.

(94) Kim, C. H.; Bonnassieux, Y.; Horowitz, G. Fundamental Benefits of the Staggered Geometry for Organic Field-Effect Transistors. *IEEE Electron Device Lett.* **2011**, *32*, 1302–1304.

(95) Natali, D.; Caironi, M. Charge Injection in Solution-Processed Organic Field-Effect Transistors: Physics, Models and Characterization Methods. *Adv. Mater.* **2012**, *24*, 1357–1387.

(96) Ullah, M.; Tandy, K.; Clulow, A. J.; Burn, P. L.; Gentle, I. R.; Meredith, P.; Lo, S. C.; Namdas, E. B. Host-Free Blue Phosphorescent Dendrimer Organic Light-Emitting Field-Effect Transistors and Equivalent Light-Emitting Diodes: A Comparative Study. *ACS Photonics* **2017**, *4*, 754–760.

(97) Wawrzinek, R.; Muhieddine, K.; Ullah, M.; Koszo, P. B.; Shaw, P. E.; Grosjean, A.; Maasoumi, F.; Stoltzfus, D. M.; Clegg, J. K.; Burn, P. L.; *et al.* Orange-Red-Light-Emitting Field-Effect Transistors Based on Phosphorescent Pt(II) Complexes with Area

Emission. *Adv. Opt. Mater.* **2016**, *4*, 1867–1874.

(98) Song, L.; Hu, Y.; Liu, Z.; Lv, Y.; Guo, X.; Liu, X. Harvesting Triplet Excitons with Exciplex Thermally Activated Delayed Fluorescence Emitters toward High Performance Heterostructured Organic Light-Emitting Field Effect Transistors. *ACS Appl. Mater. Interfaces* **2017**, *9*, 2711–2719.

(99) Ullah, M.; Tandy, K.; Li, J.; Shi, Z.; Burn, P. L.; Meredith, P.; Namdas, E. B. High-Mobility, Heterostructure Light-Emitting Transistors and Complementary Inverters. *ACS Photonics* **2014**, *1*, 954–959.

(100) Ullah, M.; Tandy, K.; Yambem, S. D.; Aljada, M.; Burn, P. L.; Meredith, P.; Namdas, E. B. Simultaneous Enhancement of Brightness, Efficiency, and Switching in RGB Organic Light Emitting Transistors. *Adv. Mater.* **2013**, *25*, 6213–6218.

(101) Namdas, E. B.; Hsu, B. B. Y.; Yuen, J. D.; Samuel, I. D. W.; Heeger, A. J. Optoelectronic Gate Dielectrics for High Brightness and High-Efficiency Light-Emitting Transistors. *Adv. Mater.* **2011**, *23*, 2353–2356.

(102) Namdas, E. B.; Samuel, I. D. W.; Shukla, D.; Meyer, D. M.; Sun, Y.; Hsu, B. B. Y.; Moses, D.; Heeger, A. J. Organic Light Emitting Complementary Inverters. *Appl. Phys. Lett.* **2010**, *96*, 2008–2011.

(103) Seo, J. H.; Namdas, E. B.; Gutacker, A.; Heeger, A. J.; Bazan, G. C. Conjugated Polyelectrolytes for Organic Light Emitting Transistors. *Appl. Phys. Lett.* **2010**, *97*, 1–4.

(104) Seo, J. H.; Namdas, E. B.; Gutacker, A.; Heeger, A. J.; Bazan, G. C. Solution-Processed Organic Light-Emitting Transistors Incorporating Conjugated Polyelectrolytes. *Adv. Funct. Mater.* **2011**, *21*, 3667–3672.

(105) Zakharko, Y.; Held, M.; Sadafi, F. Z.; Gannott, F.; Mahdavi, A.; Peschel, U.; Taylor, R. N. K.; Zaumseil, J. On-Demand Coupling of Electrically Generated Excitons with Surface Plasmons via Voltage-Controlled Emission Zone Position. *ACS Photonics* **2016**, *3*, 1–7.

(106) Zakharko, Y.; Held, M.; Graf, A.; Rödlmeier, T.; Eckstein, R.; Hernandez-Sosa, G.; Hähnlein, B.; Pezoldt, J.; Zaumseil, J. Surface Lattice Resonances for Enhanced and Directional Electroluminescence at High Current Densities. *ACS Photonics* **2016**, *3*, 2225–2230.

(107) Birks, J. *Photophysics of Aromatic Molecules*; Wiley: London, 1970.

(108) Sachtler, W. M. H.; Dorgelo, G. J. H.; Holscher, A. A. The Work Function of Gold. *Surf. Sci.* **1966**, *5*, 221–229.

(109) Roelofs, W. S. C.; Adriaans, W. H.; Janssen, R. A. J.; Kemerink, M.; De Leeuw, D. M. Light Emission in the Unipolar Regime of Ambipolar Organic Field-Effect Transistors. *Adv. Funct. Mater.* **2013**, *23*, 4133–4139.

(110) Ullah, M.; Armin, A.; Tandy, K.; Yambem, S. D.; Burn, P. L.; Meredith, P.; Namdas, E. B. Defining the Light Emitting Area for Displays in the Unipolar Regime of Highly Efficient Light Emitting Transistors. *Sci. Rep.* **2015**, *5*, 1–6.

(111) Muhieddine, K.; Ullah, M.; Maasoumi, F.; Burn, P. L.; Namdas, E. B. Hybrid Area-Emitting Transistors: Solution Processable and with High Aperture Ratios. *Adv. Mater.* **2015**, *27*, 6677–6682.

(112) Ullah, M.; Lin, Y. H.; Muhieddine, K.; Lo, S. C.; Anthopoulos, T. D.; Namdas, E. B. Hybrid Light-Emitting Transistors Based on Low-Temperature Solution-Processed Metal Oxides and a Charge-Injecting Interlayer. *Adv. Opt. Mater.* **2016**, *4*, 231–237.

(113) Zaumseil, J.; Sirringhaus, H. Electron and Ambipolar Transport in Organic Field-Effect Transistors. *Chem. Rev.* **2007**, *107*, 1296–1323.

(114) Kajii, H.; Tanaka, H.; Kusumoto, Y.; Ohtomo, T.; Ohmori, Y. In-Plane Light Emission of Organic Light-Emitting Transistors with Bilayer Structure Using Ambipolar Semiconducting Polymers. *Org. Electron.* **2015**, *16*, 26–33.

(115) Ohtomo, T.; Hashimoto, K.; Tanaka, H.; Ohmori, Y.; Ozaki, M.; Kajii, H. Improved Carrier Balance and Polarized In-Plane Light Emission at Full-Channel Area in Ambipolar Heterostructure Polymer Light-Emitting Transistors. *Org. Electron.* **2016**, *32*, 213–219.

(116) Chaudhry, M. U.; Muhieddine, K.; Wawrzinek, R.; Li, J.; Lo, S. C.; Namdas, E. B. Nano-Alignment in Semiconducting Polymer Films: A Path to Achieve High Current Density and Brightness in Organic Light Emitting Transistors. *ACS Photonics* **2018**, *5*, 2137–2144.

(117) Ai, X.; Evans, E. W.; Dong, S.; Gillett, A. J.; Guo, H.; Chen, Y.; Hele, T. J. H.; Friend, R. H.; Li, F. Efficient Radical-Based Light-Emitting Diodes with Doublet Emission. *Nature* **2018**, *563*, 536–540.

CHAPTER 2

ORGANIC SOLAR CELLS WITH THE DA_4 –TYPE NON-FULLERENE ELECTRON ACCEPTOR BASED ON 3-DICYANOMETHYLIDENE-INDAN-1-ONE

2.1 Introduction and background

The trends in organic solar cell research discussed in Chapter 1 indicate that the development of new electron acceptors is one of the major reasons for a significant boost of photovoltaic efficiencies observed in the past several years.[1–5] Fullerene based acceptors, such as $PC_{71}BM$ and $PC_{61}BM$ dominated the field for almost two decades since the time they were first introduced in 1995.[6] Those modified fullerenes exhibited good solubility in common organic solvents and good morphological and energetic compatibility with most electron donors. In addition, they also formed desired bulk heterojunction structures that resulted in highly efficient devices.[7] Despite those benefits, fullerene-based materials exhibit weaker light absorption and limited possibilities for chemical functionalization, which makes it difficult to fine-tune the material properties and device fabrication conditions. Therefore, the search for alternative acceptor materials was necessary in order to achieve higher photovoltaic efficiencies. Both polymer and small molecule acceptors were explored, however the major success was achieved with the small molecules. Rylene based structures, such as perylene diimide (PDI) or naphthalene diimide (NDI) are among the most commonly used fragments in organic electron acceptors. Just a few of their benefits include relative ease of synthesis, chemical stability, strong light absorption, and appropriate energy levels. In addition, a wide variety of possible ways of chemical functionalization make it possible to develop a multitude of structures and fine-tune the properties.

A large family of rylene based electron acceptors has been previously developed and studied in Luping Yu lab. We have established several design strategies that resulted in high-efficiency devices. Firstly, the intramolecular donor-acceptor polarization is important. One of the problems existing in organic materials is hindered exciton dissociation and increased recombination due to lower dielectric constant of the organic medium and thus stronger coulombic attraction between holes and electrons. The intramolecular polarization present in donor-acceptor materials provides additional driving force for exciton splitting and opens a new avenue for the development of more efficient organic photovoltaics. We studied several donor-acceptor combinations, such as weak donor-strong acceptor (WD-SA), weak acceptor-strong acceptor (WA-SA), strong donor-strong acceptor (SD-SA) and found that the latter one is the most efficient.[8,9] PDI unit worked as a strong acceptor in these molecules. Secondly, DA_4 structure with four accepting units being connected to a donor core was the most promising in our studies. When acceptor units are arranged in cross-like geometry, it somewhat mimics the spherical shape of PCBM buckyball providing symmetrically distributed electron density around the core. Electron acceptor TPB with four PDI units connected through alpha position to a donor benzodithiophene (BDT) core showed power conversion efficiencies of 8.5% for a champion device.[10] A similar molecule with PDIs connected through a beta position had lower PCE of 5.85%, due to steric hindrance present in the bay position of perylene diimide unit making it less planar.[11] Interestingly, when steric hindrance was eliminated through cyclization of PDI and the core, forming a fused rigid structure, the efficiency of devices improved to 7.7%. The structures with four acceptor units distributed around the conjugated core may also improve exciton dissociation. The electron transferred from the donor to acceptor during exciton dissociation

becomes delocalized over four acceptor units in the molecule. This increases hole-electron separation distance and prevents their immediate recombination from happening in the system.[12] We explored different kinds of DA_4 structures, including the ones with the conjugated core, fused propeller-type molecules, tetrahedral single atom core and different PDI connecting modes. However, there are limited possibilities of molecular design when exclusively PDI is used as an electron-withdrawing unit. Moreover, most PDI based compounds have similar light absorption profiles and energy levels. This limits their compatibility with certain high-efficiency donors and hinders further progress in the field. In this chapter we present and explore new DA_4 type acceptor TCN-BDT with the strong and compact, non-PDI electron withdrawing unit 3-(dicyanomethylidene)-indan-1-one (DCI).

2.2 Results and Discussion

2.2.1 Molecular Design and Characterization of Basic Properties

The molecular structures of electron acceptor TCN-BDT and polymer electron donor PTB7-Th used in this study are shown in Figure 2.1a. Four electron-withdrawing units are connected to benzodithiophene core through thiophene bridges. The alkyl chains are added to the thiophene units for better solubility of the acceptor. DCI was chosen as an electron-accepting unit in the molecule due to its superior electron-withdrawing abilities. As a result, the DCI containing compounds have LUMO energy levels close to PCBM -3.9 eV, which provides enough driving force for exciton dissociation for most electron donors. Polymer PTB7-Th is a widely used electron donor in OPV due to its strong light absorption, face-on preferential orientation in the solid-state packing, appropriate energy levels, and good solubility in organic solvents. We used DFT calculations to determine the acceptor molecule's optimized geometry, shape, and the

distribution of HOMO/LUMO frontier orbitals and their energies. As shown in Figure 1.2b TCN-BDT molecule has the optimized cross-like geometry. Four DCI units are uniformly distributed around the center. HOMO orbitals are predominantly concentrated on the electron-donating BDT core and LUMO orbitals are localized on electron-withdrawing DCI units. We further characterized properties of the molecules and measured their HOMO and LUMO energy levels using cyclic voltammetry (CV). The results plotted in Figure 2.1c show that PTB7-Th donor has HOMO level at -5.2 eV and LUMO at -3.6 eV. The acceptor TCN-BDT has lower levels – HOMO at -5.4 eV and LUMO at -3.9 eV. LUMO energy of TCN-BDT is very close to LUMO of PCBM based acceptors, but HOMO is 0.7 eV higher. There is a downward energy cascade in LUMOs from the donor to the acceptor, which provides a driving force of 0.3 eV to facilitate the exciton splitting at the donor-acceptor bulk heterojunction interface.

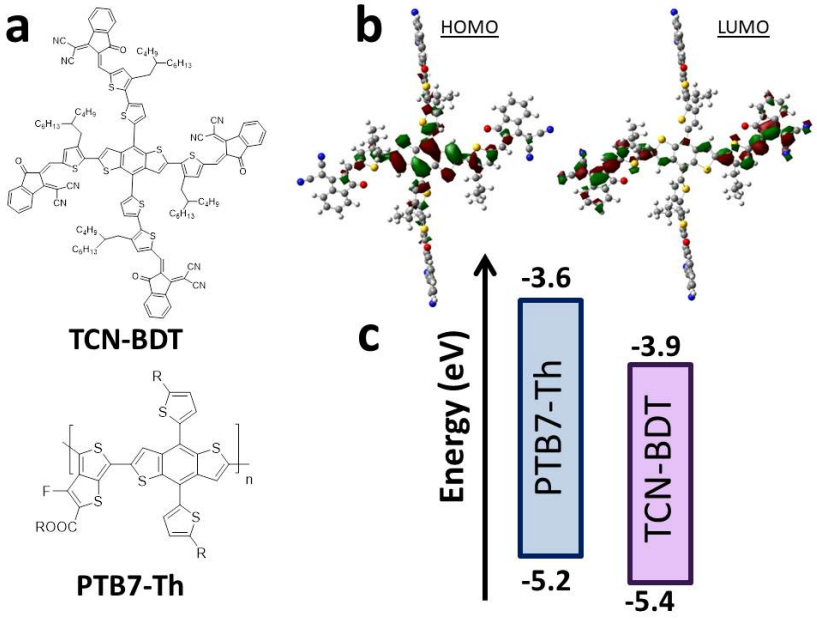

Figure 2.1. a) Structural formulas of polymer donor PTB7-Th and non-fullerene small molecule acceptor TCN-BDT; b) DFT calculated geometries of HOMO and LUMO orbitals in TCN-BDT; c) Energy level diagram of PTB7-Th and TCN-BDT.

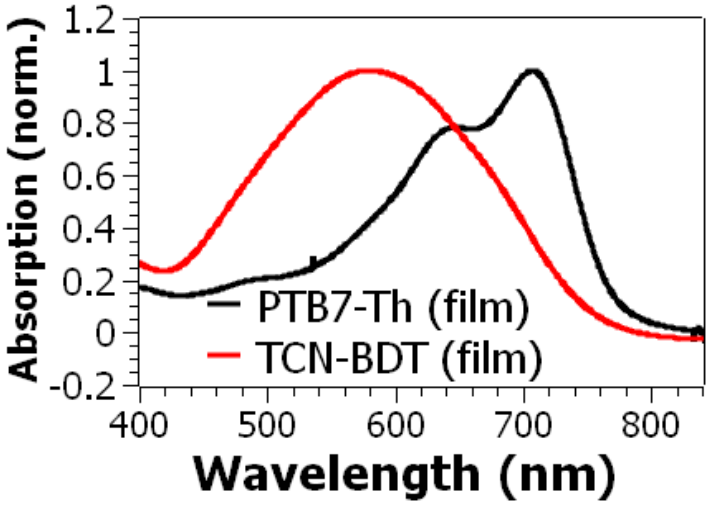

Figure 2.2. UV-Vis absorption spectra of PTB7-Th and TCN-BDT films.

We measured the optical properties of TCN-BDT and PTB7-Th. The UV-Vis absorption spectrum depicted in Figure 2.2 shows that TCN-BDT has a broad, featureless absorption spectrum ranging from 400 nm to 750 nm with the absorption maximum at 580 nm. The absorption onset is at 750 nm which corresponds to the optical band gap of 1.65 eV. This is very close to the electrochemical band gap of 1.5 eV, which was calculated from HOMO-LUMO energy gap. The donor polymer has the absorption spectrum ranging from 550 nm to 800 with two peaks at 640 nm and 700 nm. The absorption spectra of two compounds are complementary to each other and cover all the visible range, all the way to the near-IR. We measured the concentration-dependent absorption and fluorescence properties of TCN-BDT in chloroform solution (Figure 2.9). The solution absorption spectrum stays unchanged in the range of concentrations from 10^{-7} M to 10^{-5} M, which indicates that possible aggregation of TCN-BDT does not change its optical properties. A similar trend was observed in molecule's

photoluminescence spectrum. The spectra excited at 565 nm had broad, featureless, concentration-independent emission from 600 nm to 850 nm with the maximum at 700 nm.

2.2.2 Photovoltaic Properties

We studied the photovoltaic properties of these materials and used PTB7-Th/TCN-BDT blend as an active layer in organic solar cells. We assembled devices in an inverted configuration, consisting of ITO/ZnO/active layer/MoO_x/Ag layers. Indium tin oxide (ITO) was used as a transparent, conductive electrode, ZnO was electron transporting layer, MoO_x hole transporting layer and Ag was top metal electrode. It is known that the device fabrication conditions, in particular higher boiling point solvent additives, significantly affect device performance. For example, the devices with PTB7-Th and PCBM have much better performance due to more favorable phase separation when 1,8-diiodooctane (DIO) is used as a solvent additive in addition to the main solvent chlorobenzene. In our previous studies of non-fullerene electron acceptor TPB, devices with diphenyl ether (DPE) had better performance. In this study with PTB7-Th and TCN-BDT we optimized device fabrication conditions and study effects of solvent additives DIO, DPE and mixed DIO+DPE system. The photovoltaic performance was evaluated by measuring voltage-current characteristics of the devices under AM1.5G illumination with an intensity of 100 mW cm^{-2}. The solar cell parameters, such as open-circuit voltage V_{OC}, short-circuit current density J_{SC} and fill factor FF were extracted from J-V curves and power conversion efficiency (PCE) of the devices was calculated from them. The photovoltaic parameters are summarized in Table 2.1.

Table 2.1 Averaged photovoltaic parameters of devices based on PTB7-Th/TCN-BDT active layer without any solvent additives, with DIO, DPE and DIO+DPE as a solvent additive.

Solvent additive	V_{OC} (V)	J_{SC} (mA cm^{-2})	FF (%)	PCE^{av} [PCE^{max}] (%)
No additive	0.82±0.00	15.7±0.3	56.0±1.0	7.1±0.1 [7.2]
DIO	0.77±0.08	15.4±0.3	61.1±1.0	7.2±0.2 [7.4]
DPE	0.76±0.01	15.5±0.4	55.0±3.0	6.5±0.3 [6.9]
DIO+DPE	0.77±0.00	15.8±0.3	64.0±1.0	7.8±0.2 [8.1]

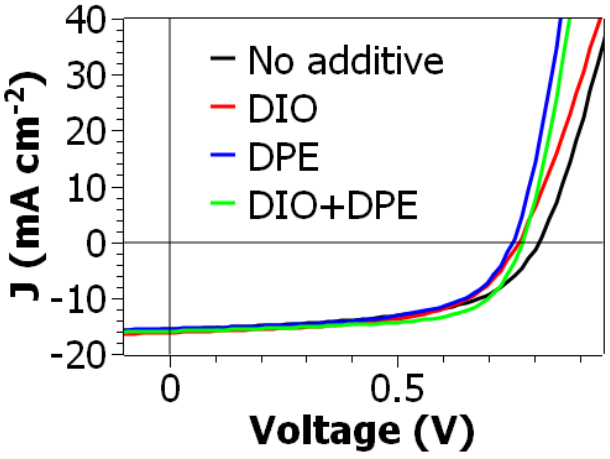

Figure 2.3. Current-voltage characteristics of OPV devices.

The devices have typical J-V curves shown in Figure 2.3. Even without any solvent additives, the system PTB7-Th/TCN-BDT demonstrated promising photovoltaic performance. The average power conversion efficiency of the system was 7.1% with V_{OC} 0.82V, J_{SC} 15.7 mA cm^{-2} and FF 56%. Voltage and current observed in this system are comparable to devices with PCBM, however FF is much lower, which is a commonly observed problem in non-fullerene acceptor devices. The introduction of solvent additives significantly affected FF in these devices. Thus, when DIO was used as a solvent additive V_{OC} decreased slightly from 0.82 to

0.77 V and J_{SC} decreased from 15.7 to 15.4 mA cm^{-2}. At the same time fill factor increased from 56.0% to 61.1%, which slightly increased overall average PCE from 7.1% to 7.2%. The addition of DPE slightly decreased overall performance of devices from 7.1 to 6.5%, with the V_{OC} decreasing from 0.82 to 0.76 V, J_{SC} decreasing from 15.7 to 15.5 mA cm^{-2} and FF staying almost the same 56 versus 55%. The most effective approach was using mixed solvent additive DIO+DPE. In this system FF increased significantly from 56% to 64% and overall PCE increased from 7.1 to 7.8% with the champion device PCE 8.1%.

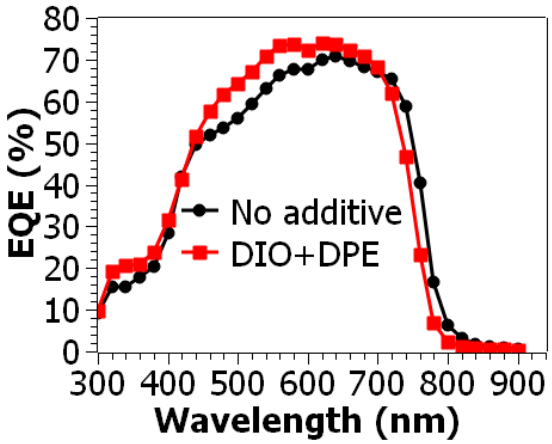

Figure 2.4. Wavelength dependent external quantum efficiency EQE.

We measured the spectral dependence of photovoltaic efficiency by measuring external quantum efficiency EQE (Figure 2.4). Photovoltaic devices are active in the range of wavelengths from 400 nm to 800 nm, which is consistent with the absorption profile of the materials composing the blend. For devices without solvent additive, EQE reaches a maximum of 70% at 640 nm, which corresponds to absorption peak of PTB7-Th. The EQE spectrum sustains the value above 65% in the range of 560-720 nm, which corresponds to absorption

profile of PTB7-Th and covers the onset and absorption maximum of TCN-BDT. It is evident from the EQE spectrum that photons absorbed by the polymer are converted into charge carriers more efficiently, than the ones absorbed by the acceptor. The shape of the spectrum changes when mixed DIO/DPE additive is used. Two peaks with EQE 74% are observed at 570 nm and 630 nm, which correspond to absorption maxima of TCN-BDT and PTB7-Th. In this case charge carrier harvesting from excitons generated in TCN-BDT significantly improved, compared to the devices without any solvent additives.

2.2.3 Mechanistic Studies

We studied the photovoltaic mechanisms in the devices with and without solvent additives. Charge carrier recombination is one of the most important parameters affecting the performance of solar cells. We conducted light intensity (LI) dependent studies to characterize recombination in the devices. Typically, the dependence of $\log(J_{SC})=\alpha\times\log(LI)+A$ will be linear with the slope $\alpha=1$ when bimolecular recombination is low.[13] Non-linear trends are observed when significant recombination is present. Results are shown in Figure 2.5

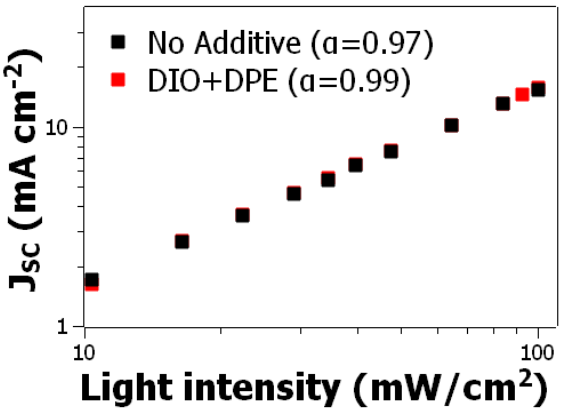

Figure 2.5. Dependence of short circuit current density J_{SC} of OPV devices on light intensity.

For devices both with and without solvent additives, the recombination is quite low. Devices without any solvent additives had slope α=0.97, which increased slightly to 0.99 when mixed DIO/DPE additive was used. Recombination decreased in the devices with mixed solvent additive.

In addition to the charge recombination, we studied the opposite process of exciton dissociation as well. Exciton dissociation probability can be evaluated from the dependence of photocurrent J_{ph} on the effective voltage of the device. It is assumed that 100% exciton dissociation is observed at high effective voltages in the device. Exciton dissociation probability at the device operating conditions can be evaluated by normalizing photocurrent density at short circuit conditions to the saturated current observed at higher effective voltages. The dependence of J_{ph} on effective voltage is shown in Figure 2.6.

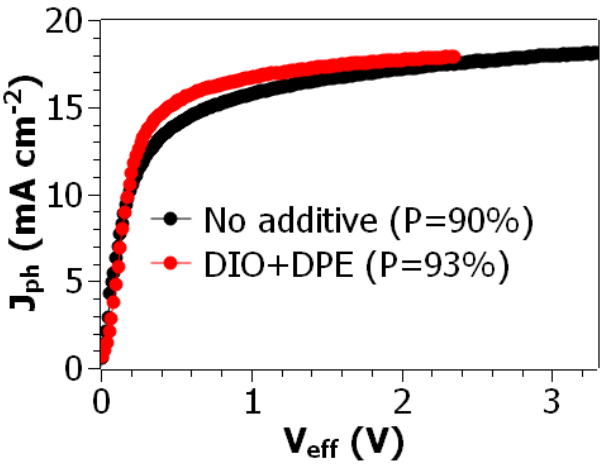

Figure 2.6. Dependence of photocurrent J_{ph} on the effective voltage in the device.

Exciton dissociation probability increases from 90% without solvent additive to 93% with mixed DIO/DPE solvent additive. Therefore, based on these data we can see that excitons are more likely to dissociate and exhibit less bimolecular recombination when films are processed from solutions with mixed solvent additive.

2.2.4 Morphology Studies

In order to rationalize observed results, we studied the morphology of the active layer films. The GIWAXS scattering profiles are shown in Figure 2.7. The neat TCN-BDT film shows quite strong and broad arc-like scattering, which indicates significant aggregation in the film, but it lacks a preferential orientation. The blend films are more crystalline and their packing depends on the solvent additive used. To obtain the quantitative data on the packing, we extracted 1D linecut graphs in out-of-plane and in-plane directions and fitted the peaks. The graphs are shown in Figure 2.8 and quantitative parameters are summarized in Table 2.2.

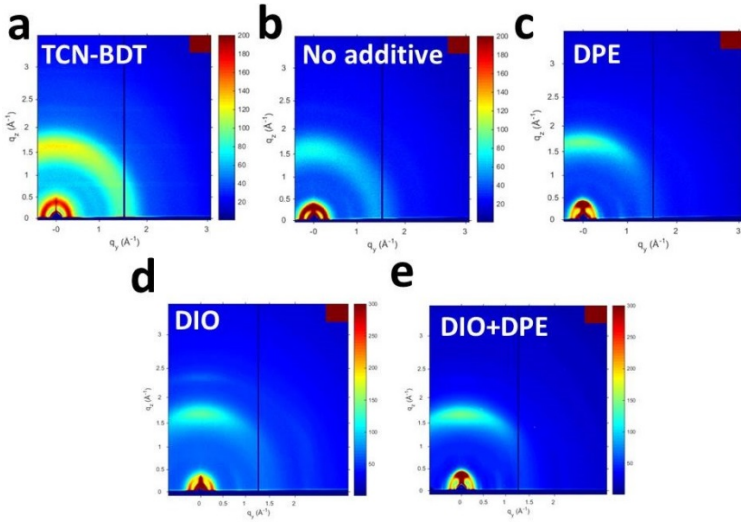

Figure 2.7. Image of grazing incidence wide-angle x-ray scattering (GIWAXS) 2D profile for a) neat TCN-BDT, b) PTB7-Th/TCN-BDT blend prepared without solvent additives, c) PTB7-Th/TCN-BDT blend prepared with a DPE, d) PTB7-Th/TCN-BDT blend prepared with a DIO, e) PTB7-Th/TCN-BDT blend prepared with a mixed additive DPE+DIO

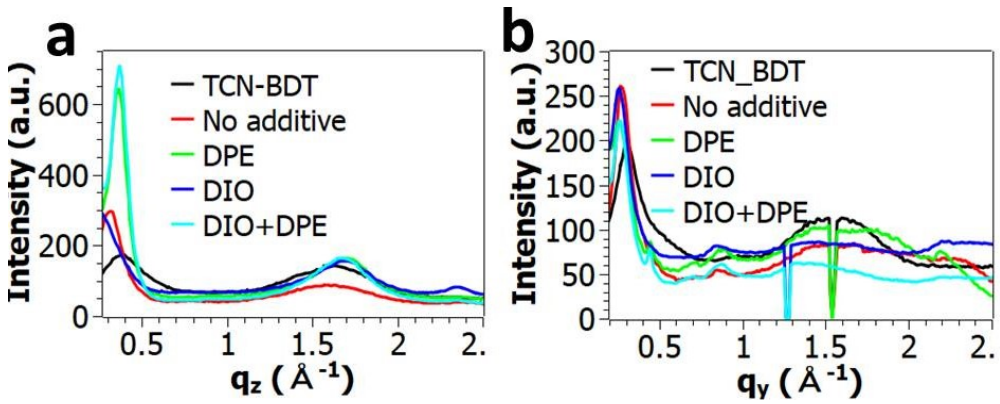

Figure 2.8. 1D linecuts of GIWAXS scattering profiles in a) out-of-plane direction and b) in-plane direction.

Table 2.2. Summary of GIWAXS linecut parameters in out-of-plane (OoP) and in-plane (IP) directions.

System	Lamellar OoP peak				π-π OoP peak				Lamellar IP peak			
	q_z (Å^{-1})	D_z (Å)	Δq_z (Å^{-1})	L_z (Å)	q_z (Å^{-1})	D_z (Å)	Δq_z (Å^{-1})	L_z (Å)	q_y (Å^{-1})	D_y (Å)	Δq_y (Å^{-1})	L_y (Å)
Acceptor	0.39	16.1	0.28	20.0	1.60	3.93	1.47	3.85	0.31	20.3	0.35	16.3
Blend:												
No SA	0.31	20.3	0.19	29.7	1.59	3.96	1.45	3.90	0.28	22.5	0.26	21.7
DIO	-	-	-	-	1.67	3.75	0.89	6.33	0.25	24.5	0.31	18.2
DPE	0.36	17.5	0.10	58.4	1.68	3.75	0.99	5.68	0.25	24.6	0.34	16.7
Mixed	0.36	17.3	0.11	48.8	1.66	3.79	0.44	12.9	0.26	24.0	0.30	18.9

SA – solvent additive; q – position of the peak, D – spacing ($D=\frac{2\pi}{q}$), Δq – peak's full width at half maximum (FWHM), L – correlation length calculated from FWHM using Scherrer analysis.

TCN-BDT film has two peaks in out-of-plane direction – at 0.39 Å^{-1} and a broad peak from 1.2 to 2 Å^{-1} centered at around 1.6 Å^{-1}. From our previous studies, we found that PTB7-Th neat film exhibits scattering peaks at 0.28 Å^{-1} and at 1.61 Å^{-1}. The π-π scattering peaks at around 1.6 Å^{-1} overlap for polymer and for acceptor in this case, which makes it hard to distinguish their behavior in the blend. The donor-acceptor blend processed without any solvent additives exhibits narrow lamellar peak centered at 0.31 Å^{-1} which indicates that TCN-BDT does not form

detectable individual crystalline structures and is well blended with the donor polymer. When mixed solvent additive is used the peak becomes more intense and its position shifts to 0.36 $Å^{-1}$. In addition, an increase in correlation length from 29.7 to 48.8 Å indicates higher crystallinity of the system. The proximity of the blend lamellar peak's position to the peak of the neat TCN-BDT possibly indicates formation of more crystalline phase of acceptor in the blend. This is consistent with the fact that EQE increased in the TCN-BDT absorption region after mixed solvent additive was used. More crystalline TCN-BDT phase will facilitate extraction of charge carriers generated from the excitons originated in the acceptor. The position of π-π stacking peaks didn't change significantly when TCN-BDT was blended with PTB7-Th without solvent additives used, however it shifted to 1.66 $Å^{-1}$ for the films processed from mixed additive. Also, correlation length increased more than 3 times, from 3.9 to 12.9 Å, which indicates much more crystalline π-π stacking. Due to overlapping position of peaks for PTB7-Th and TCN-BDT we could not distinguish which of the blend components was predominantly responsible for an increase in the crystallinity. However, it is evident from the morphology changes that DIO predominantly affects crystallinity at the lower scale of π-π stacks and DPE mostly increases crystallinity of larger scale lamellar polymer layers. When combined together as a solvent additive they result in more efficient OPV devices with the PCE of >8%.

2.3 Conclusions

As a result of our studies, we have developed a new DA_4-type electron acceptor with non-PDI electron-withdrawing units and studied its photovoltaic properties. PTB7-Th was used as an electron donor due to its complementary absorption and appropriate energy levels providing enough driving force for exciton separation. We found that solar cell devices based on PTB7-

Th/TCN-BDT blend achieve power conversion efficiencies of 7.1% with the V_{OC} of 0.82V, J_{SC} 15.7 mA cm^{-2} and FF 56%. These results can be further improved to more than 8% PCE if mixed DIO/DPE solvent additive is used. The origin of this improvement is mostly in an increased FF, from 56% for devices without solvent additives to 64% with mixed DIO/DPE additive. Mechanistic studies showed that light harvesting from TCN-BDT improved upon addition of mixed solvent additive and exciton dissociation improved together with decreased bimolecular recombination. Favorable morphology was mostly responsible for performance improvements. The addition of DPE improved lamellar crystallinity of the blend with the more organized TCN-BDT phase. The simultaneous presence of DIO and DPE increased lamellar and π-π stacking crystallinity of the blend which improved charge transport and resulted in more efficient devices.

2.4 Experimental Section

Materials used

Small molecule acceptor TCN-BDT and all of its precursors were synthesized and purified by Dr. Qinghe Wu using methods described elsewhere.[10,14] Polymer donor PTB7-Th was purchased from 1 Material, Inc. Anhydrous solvents and solvent additives chlorobenzene, DIO and DPE were purchased from Sigma Aldrich and used without further purification. ZnO was prepared via sol-gel method using $Zn(CH_3COO)_2 \cdot 2H_2O$, 2-methoxyethanol and 2-aminoethanol all of which were purchased from Sigma Aldrich and used as obtained. Molybdedum oxide for device fabrication was purchased from Sigma Aldrich and silver was purchased from Fisher Scientific.

Device fabrication

Devices were assembled in an inverted configuration including layers of ITO/ZnO/active layer/MoO_x/Ag sequentially deposited on top of each other. ITO glass was purchased from the company Thin Film Devices. To clean glass slides, they were sequentially ultrasonicated in chloroform, acetone and isopropyl alcohol, 15 minutes for each solvent. After ultrasonication the glasses were exposed to UV light /O_3 for 20 minutes, cooled down to room temperature and layer of ZnO was deposited on it. We used sol-gel method of ZnO formation described in the literature. The precursor solution was prepared 12 hours ahead of time and used immediately after that. The solution was filtered through syringe PTFE filter, 2-3 drops of it were placed onto the ITO surface and spin-coated at 4000 rpm/40 seconds in air. Films were immediately annealed in air at 200^0C for 30 minutes (films placed on hot surface). After annealing films were slowly cooled down to room temperature and transferred to glove box. Polymer and small molecule acceptors were dissolved in a mixture of solvents to prepare a series of solutions in chlorobenzene, chlorobenzene:DIO, chlorobenzene:DPE and chlorobzenene:DIO:DPE. Concentrations of all components were optimized for maximum results. The ratio of PTB7-Th to TCN-BDT was 1 to 1.5 by weight. The concentration of solvent additives was optimized for maximum performance. For DIO only devices the content of DIO was 1% of total liquid volume. For DPE only devices the concentration of DPE was 5% by volume. For mixed DIO/DPE devices their ratio was 0.5%/5% by volume. The solutions were stirred overnight at 85^0C and spin-coated on ZnO surface at 70^0C. After spin-coating films were immediately transferred to vacuum chamber for thermal evaporation of top electrode. Molybdenum (VI)

oxide (8 nm) and Ag (100 nm) were thermally evaporated on the active layer surface under vacuum < $2 \cdot 10^{-6}$ Torr.

Device characterization

To test solar cell performance of the devices J-V curves were obtained under illumination and in dark using source meter unit Keithley 2420. Devices for OPV were tested under 1 sun conditions (AM1.5G, 100 mW cm^{-2}) using xenon lamp (Oriel 69920) intensity of which was calibrated with a standard NREL certified Si cell (Newport, 91150V). Masks with a well-defined area of 3.14 mm^2 were used to define an active area of the device. EQE was measured with a Newport QE measurement system (IQE-200) with a tungsten halogen lamp as a light source. For light intensity-dependent measurements a series of neutral density filters was used.

Optical and electrochemical properties

HOMO and LUMO energy levels were measured as oxidation and reduction onsets in cyclic voltammograms. CV was measured in 3 electrode configuration using PGSTAT 12 potentiostat. Silver chloride (Ag/AgCl) electrode was used as a reference electrode and two platinum wires were used as a working and counter electrodes. 0.1M solution of tetra-n-butylammonium hexafluorophosphate in anhydrous acetonitrile was used as an electrolyte.

Solution and film absorption spectra were measured using SHIMADZU UV-2401PC spectrometer. Fluorescence spectra were measured using Horiba FluoroLog fluorometer at the University of Chicago MRSEC MPML facilities.

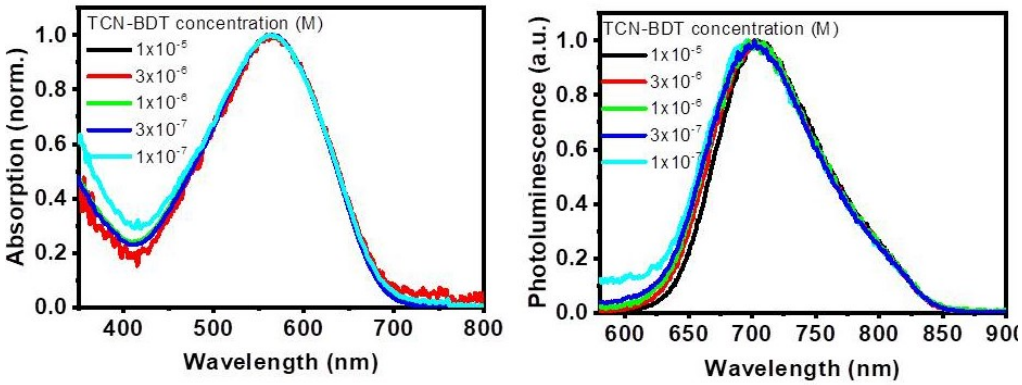

Figure 2.9. Concentration-dependent UV-Vis absorption spectra (left) and photoluminescence spectra excited at 565 nm (right) of TCN-BDT solutions in chloroform.

Morphology

The GIWAXS measurements were performed at 8ID-E beamline of Advanced Photon Source, Argonne National Laboratory with a radiation wavelength 1.1364 Å. Samples for GIWAXS were prepared on polished Si wafer, covered with ZnO and coated with an active layer film being studied. Scherrer analysis of GIWAXS data was conducted where linecut peaks were fitted with pseudo-Voigt function to determine peak's position and full width at half maximum (FWHM).

2.5 References

(1) Wadsworth, A.; Moser, M.; Marks, A.; Little, M. S.; Gasparini, N.; Brabec, C. J.; Baran, D.; McCulloch, I. Critical Review of the Molecular Design Progress in Non-Fullerene Electron Acceptors towards Commercially Viable Organic Solar Cells. *Chem. Soc. Rev.* **2019**, *48*, 1596–1625.

(2) Hou, J.; Inganäs, O.; Friend, R. H.; Gao, F. Organic Solar Cells Based on Non-Fullerene Acceptors. *Nat. Mater.* **2018**, *17*, 119–128.

(3) Zhang, G.; Zhao, J.; Chow, P. C. Y.; Jiang, K.; Zhang, J.; Zhu, Z.; Zhang, J.; Huang, F.; Yan, H. Nonfullerene Acceptor Molecules for Bulk Heterojunction Organic Solar Cells. *Chem. Rev.* **2018**, acs.chemrev.7b00535.

(4) Zhang, J.; Tan, H. S.; Guo, X.; Facchetti, A.; Yan, H. Material Insights and Challenges for Non-Fullerene Organic Solar Cells Based on Small Molecular Acceptors. *Nat. Energy* **2018**, *3*, 720–731.

(5) Gasparini, N.; Wadsworth, A.; Moser, M.; Baran, D.; McCulloch, I.; Brabec, C. J. The Physics of Small Molecule Acceptors for Efficient and Stable Bulk Heterojunction Solar Cells. *Adv. Energy Mater.* **2018**, *8*, 1–15.

(6) Hummelen, J. C.; Knight, B. W.; LePeq, F.; Wudl, F.; Yao, J.; Wilkins, C. L. Preparation and Characterization of Fulleroid and Methanofullerene Derivatives. *J. Org. Chem.* **1995**, *60*, 532–538.

(7) Yu, G.; Gao, J.; Hummelen, J. C.; Wudl, F.; Heeger, A. J. Polymer Photovoltaic Cells : Enhanced Efficiencies via a Network of Internal Heterojunctions. *Science (80-.).* **1995**, *270*, 1789–1791.

(8) Jung, I. H.; Lo, W.-Y.; Jang, J.; Chen, W.; Zhao, D.; Landry, E. S.; Lu, L.; Talapin, D. V; Yu, L. Synthesis and Search for Design Principles of New Electron Accepting Polymers for All-Polymer Solar Cells. *Chem. Mater.* **2014**, *26*, 3450–3459.

(9) Jung, I. H.; Zhao, D.; Jang, J.; Chen, W.; Landry, E. S.; Lu, L.; Talapin, D. V.; Yu, L. Development and Structure/Property Relationship of New Electron Accepting Polymers Based on Thieno[2′,3′:4,5]Pyrido[2,3- *g*]Thieno[3,2- *c*]Quinoline-4,10-Dione for All-Polymer Solar Cells. *Chem. Mater.* **2015**, *27*, 5941–5948.

(10) Wu, Q.; Zhao, D.; Schneider, A. M.; Chen, W.; Yu, L. Covalently Bound Clusters of Alpha-Substituted PDI-Rival Electron Acceptors to Fullerene for Organic Solar Cells. *J. Am. Chem. Soc.* **2016**, *138*, 7248–7251.

(11) Wu, Q.; Zhao, D.; Yang, J.; Sharapov, V.; Cai, Z.; Li, L.; Zhang, N.; Neshchadin, A.; Chen, W.; Yu, L. Propeller-Shaped Acceptors for High-Performance Non-Fullerene Solar Cells: Importance of the Rigidity of Molecular Geometry. *Chem. Mater.* **2017**, *29*, 1127–1133.

(12) Wu, Q.; Zhao, D.; Goldey, M. B.; Filatov, A. S.; Sharapov, V.; Colon, Y. J.; Cai, Z.; Chen, W.; de Pablo, J. J.; Galli, G.; *et al.* Intra-Molecular Charge Transfer and Electron Delocalization in Non-Fullerene Organic Solar Cells. *ACS Appl. Mater. Interfaces* **2018**, *10*, 10043–10052.

(13) Cowan, S. R.; Roy, A.; Heeger, A. J. Recombination in Polymer-Fullerene Bulk Heterojunction Solar Cells. *Phys. Rev. B* **2010**, *82*, 245207.

(14) Jung, M. H.; Song, K. H.; Ko, K. C.; Lee, J. Y.; Lee, H. Nonvolatile Memory Organic Field Effect Transistor Induced by the Steric Hindrance Effects of Organic Molecules. *J. Mater. Chem.* **2010**, *20*, 8016–8020.

CHAPTER 3

HIGH PERFORMANCE TERNARY ORGANIC SOLAR CELLS DUE TO FAVORED INTERFACIAL CONNECTION BY A NON-FULLERENE ELECTRON ACCEPTOR WITH A CROSS-LIKE MOLECULAR GEOMETRY

3.1 Introduction and Background

Bulk heterojunction organic solar cells are very complex system. Numerous parameters, such as molecular structure, blend composition, morphology and device architecture have to be tuned to achieve high power conversion efficiency. A substantial research effort worldwide is devoted to the development of new photovoltaic materials and improvement of device fabrication for better morphology control, higher crystallinity, and more efficient light harvesting. As a consequence of these efforts, power conversion efficiencies of organic solar cells have already surpassed a mark of 13% in single heterojunction devices.[1–7] One of the effective approaches to fabricate high efficiency organic photovoltaic devices (OPV) is to utilize multiple donors or multiple acceptors approach in bulk heterojunction (BHJ) solar cells (so-called ternary blends). The obvious advantage of this approach is the ability to broaden coverage of the solar spectrum to harvest a wider range of photons and minimize the voltage-current trade-off present when only one light-absorbing material is used.[8] Another advantage is a possibility of replacing or complementing fullerene derivatives with a better absorbing non-

fullerene acceptor (NFA) thus ensuring more efficient photon harvesting in green and blue parts of the spectrum.[8–10] While ternary blend devices with donor third components (both polymer and small molecule) have been intensively studied before[8,9,11–13], ternary systems with small molecule acceptors are still an emerging field. Early trials in this field involved incorporation of multiple fullerene-based acceptors, such as PCBM and ICBA into a blend. This approach was proven to be effective resulting in an increased performance both for highly crystalline P3HT and more amorphous PTB7.[14,15] More recently, PCBM/ICBA mixture was incorporated into double donor system PTB7:PBDTTA, thus forming a quaternary blend which resulted in a performance increase up to 10.2% PCE, mostly due to complementary light absorption of components, bilateral cascade of energy levels and higher crystallinity of complementary donor polymer.[16] Even though very promising results were achieved with this strategy, possibilities for chemical modification in fullerene-based molecules are very limited, which becomes a bottleneck for further optimization. The non-fullerene acceptors and their use in ternary devices become attractive. In general, to act as an effective third component, a material must exhibit a set of essential properties, including complementary light absorption with a donor, cascade of energy levels for efficient charge transfer and morphological compatibility. More detailed mechanistic studies showed that origin of device efficiency enhancement varies depending on the nature of materials used and the composition of a system. For example, in case of indacenodithiophene based IDTBR and indenofluorene based IDFBR acceptors three distinct phases were observed in the best performing system P3HT:IDFBT:IDTBR (1:0.3:0.7) which also resulted in an increased PCE up to 7.7% PCE. The same acceptor system studied with more amorphous PTB7-Th resulted in >11% PCE.[5] Small molecule acceptors also play an

important role in controlling charge carrier mobilities, where more balanced transport of holes and electrons results in devices with better performance.[5,16–21] Another mechanism of enhancement in ternary solar cells is Förster resonance energy transfer (FRET) between components of the blend, therefore matching bandgaps of blend components are crucial for these systems. A typical example is based on squaraine based acceptors (SQ) in ternary cells as an energy transfer relay. [18,22] Similar strategy applied for planar heterojunction devices with one donor and two subphtalocyanine based acceptors resulted in an enhanced performance due to favorable energy level cascade and FRET between device components.[23] Recently indacenodithiothiopene based (ITIC) family of acceptors were reported as an effective main or third component and higher OPV performance were achieved for systems with higher ratio of ITIC in a blend (> 50% by mass).[19,24,25]

Despite all the progress made in developing ternary OPV cells, there are still challenges that need to be addressed, especially associated with the working mechanism of a third component. The binary OPV cells are already complex systems, and the addition of the third component makes the complexity multiplied. Previously, we reported an electron acceptor (TPB) that has lowest unoccupied molecular orbital (LUMO) energy level very close to that of the $PC_{71}BM$.[26,27] Its highest occupied molecular orbital (HOMO) is higher than that of $PC_{71}BM$ and lower than that of a donor polymer PTB7-Th, forming a hole transport cascade. The suitable molecular energy levels and complementary absorption spectra make TPB an ideal third component candidate for ternary solar cells. It was found that the inverted PTB7-Th/$PC_{71}BM$ OPV devices with TPB as the third component exhibited a PCE as high as 10.6%

while PCE for binary devices is 9.8%. The PCE enhancement mainly comes from an increase of J_{sc} values from 17.24 to 19.44 mA cm^{-2}. The detailed study shows that TPB can act as the interface modifier due to its unique cross-like molecular geometry, which benefits more efficient exciton dissociation and charge separation at donor and acceptor interfaces.

3.2 Results and Discussion

3.2.1 OPV Performance

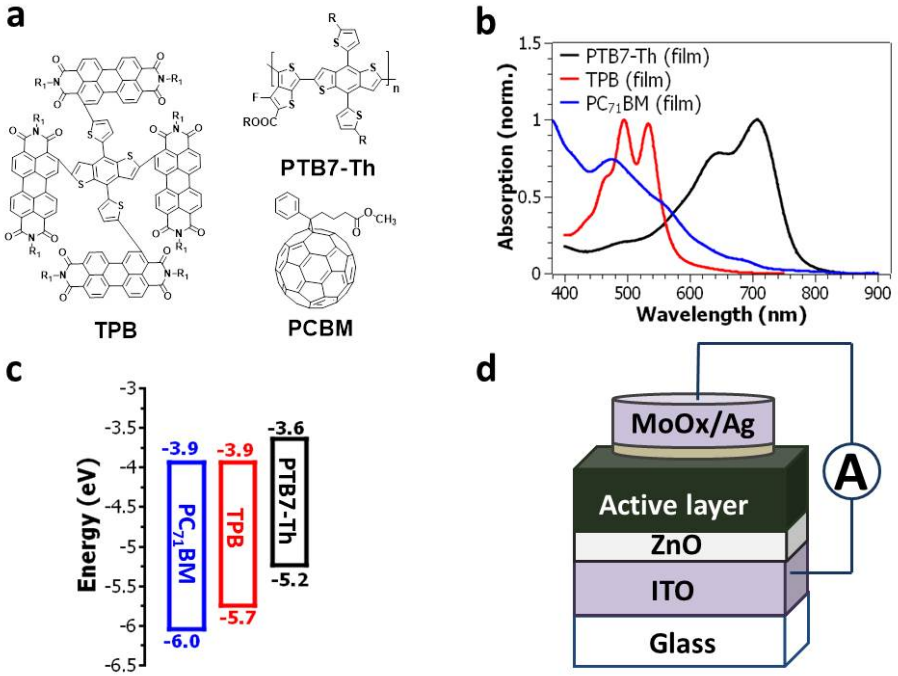

Figure 3.1. a) Chemical structures of TPB, PTB7-Th and $PC_{71}BM$ (R -ethylhexyl, R1 – propylbutyl). b) Normalized absorption spectra of PTB7-Th, TPB and $PC_{71}BM$ films. c) Energy level diagram. d) Structure of solar cell device.

The molecular structure of TPB is shown in Figure 3.1a.[26] Figure 3.1b shows that the absorption spectrum of TPB is complementary to the absorption of the donor material PTB7-Th

so that the blended film can harvest light from the spectral range between 400 and 800 nm. In addition, we measured film fluorescence and observed a significant fluorescence quenching when even a small quantity of TPB is added to PTB7-Th – 70% of fluorescence intensity is quenched when 10% TPB is present, which indicates electron transfer from the polymer to TPB (Figure 3.9). Cyclic voltammetric studies revealed the highest occupied molecular orbital (HOMO) at -5.7 eV and lowest unoccupied orbital (LUMO) at -3.9 eV (Figure 3.1c). Therefore, HOMO energy levels of the three components, PTB7-Th, TPB and $PC_{71}BM$, form a cascade, whereas the LUMOs of the two acceptors are very close, which allows for efficient charge transport from PTB7-Th but avoids unfavorable V_{OC} pinning in ternary devices.

To investigate the effect of the third component on OPV performances, a series of OPV devices with the varied content of TPB were fabricated. The composition was varied by increasing the concentration of the TPB (x) while keeping the weight ratio of PTB7-Th and $PC_{71}BM$ constant (PTB7-Th:TPB:$PC_{71}BM$ (1:x:1.5)). Devices had an inverted architecture consisting of ZnO/active layer/MoOx/Ag sequentially deposited onto the ITO glass substrate (Figure 3.1d).[28] The experimental results of OPV performance are summarized in Table 3.1 and Figure 3.2. The reference binary cell based on PTB7-Th:PC71BM (1:1.5) exhibited an average PCE value of 9.4%, with V_{OC} of 0.78 V, J_{SC} of 17.2 mA cm^{-2} and FF of 70%. The enhancement effect was observed even at the concentration of 5% (weight ratio related to donor) of the third component TPB. Further increase of the TPB concentration to 10% resulted in improved J_{SC} values from 17.2 to 19.4 mA cm^{-2} while FF decreased slightly from 70% to 68%. The optimal performance with the highest PCE of 10.6% was observed at this composition. Further increase

of third component concentration to 30% resulted in a sharp drop of J_{SC} values from 19.4 to 13.6 mA cm^{-2}, and the corresponding OPV PCE value to 6.7%.

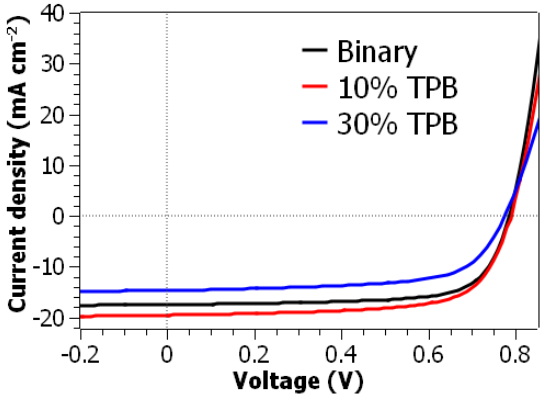

Figure 3.2. Current-voltage curves. b) External quantum efficiency spectra. c) Plot of photocurrent density versus effective voltage. d) Plot of short circuit current density versus light intensity.

We also tested device performance by screening different ratios of non-fullerene acceptor to $PC_{71}BM$ in a bulk heterojunction blend while keeping overall donor to acceptor ratio constant, the results are shown in Table 3.2.

Table 3.1. Summary of solar cell parameters of ternary blend devices with varying content of TPB and fixed ratio of PTB7-Th to PC71BM (PTB7-Th:PC71BM:TPB 1:1.5:x). (Reported mean values and standard deviations are calculated after averaging over 12 devices).

System	V_{OC} (V)	J_{SC} (mA cm^{-2})	FF (%)	PCE^{av} (max) (%)
1:1.5:0	0.78±0.01	17.2±0.5	70±0.1	9.4±0.2 (9.8)
1:1.5:0.05	0.77±0.01	17.8±0.8	70±0.1	9.7±0.2 (10.2)
1:1.5:0.1	0.78±0.01	19.4±0.3	68±1.4	10.2±0.2 (10.6)
1:1.5:0.2	0.77±0.01	19.4±0.7	67±1.2	10.0±0.3 (10.5)
1:1.5:0.3	0.76±0.02	13.6±0.5	65±2.4	6.7±0.4 (7.5)

In order to understand the role of the third component and the origin of changes in device performance, we measured the external quantum efficiency (EQE) spectra of these devices. It can be seen that when TPB (10%) was added to the blend, the EQE was enhanced over a broad range of wavelengths (Figure 3.3). The increase in the region of 450-600 nm can be attributed to the enhanced absorption by the addition of TPB component (Figure 3.10). The enhancement of EQE in PTB7-Th absorption region suggests the third component TPB facilitated extraction of charges generated in the polymer by influencing charge separation and transporting as discussed below.

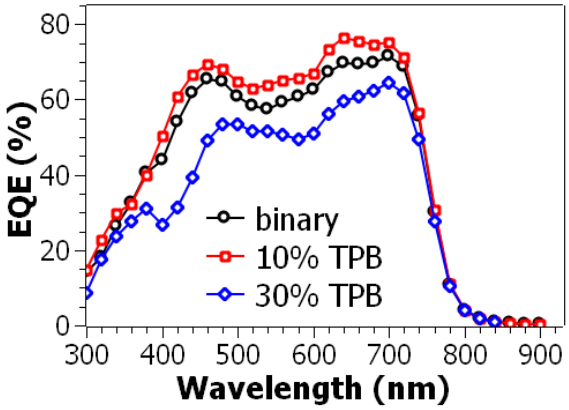

Figure 3.3. External quantum efficiency spectra.

The third component at the optimal concentration enhanced electron mobility. The SCLC hole mobility of devices was measured using a structure ITO/PEDOT/active layer/MoO_x/Ag and electron mobility of devices determined with a structure of ITO/ZnO/active layer/Ca/Al. The binary device exhibited the electron μ_e and hole μ_h mobilities of $(1.02 \pm 0.09) \times 10^{-5}$ $cm^2V^{-1}s^{-1}$ and $(1.03 \pm 0.13) \times 10^{-4}$ $cm^2V^{-1}s^{-1}$, respectively. When the third component was added (10%), electron mobility was increased to $(3.53 \pm 0.46) \times 10^{-5}$ cm^2V^{-}

^{1}s^{-}1, at the same time hole mobility was $(1.01 \pm 0.09) \times 10^{-4}$ cm^{2}V^{-1}s^{-1}, showing just minor changes. The addition of non-fullerene acceptor TPB seems to facilitate mostly electron transport in the device. However, when the concentration of the third component reached 30%, a significant decrease was observed in hole mobility down to $(3.31 \pm 0.43) \times 10^{-5}$ cm^{2}V^{-1}s^{-1}, resulting in lower short circuit current density, thus lower EQE and PCE.

3.2.2 Mechanistic Studies

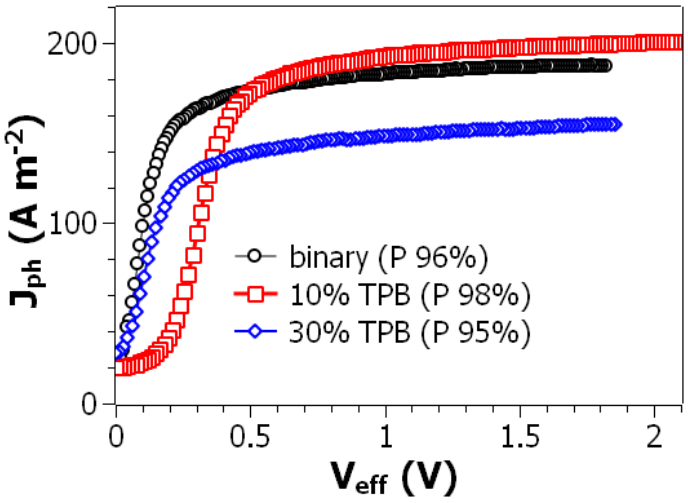

Figure 3.4. Plot of photocurrent density versus effective voltage.

The addition of the third component only slightly affects the rate of exciton dissociation and charge generation. The exciton dissociation probability for binary and ternary devices with 10% and 30% of TPB was reflected in a plot in Figure 3.4, which represents dependence of device photocurrent density J_{ph} on an effective voltage of the device V_{eff} ($V_{eff} = V_0$-V_{appl}, where V_0 voltage where J_{ph} is zero and V_{appl} is applied voltage). It can be noted that the photocurrent

increases with increasing effective voltage, reaching the saturation current, J_{sat}, at V_{eff} > 1.5 V, which depends only on the density of excitons generated in the film. It was assumed that at this point all generated excitons dissociate under the applied field. The exciton dissociation probability P is determined by normalizing photocurrent density J_{ph} at short-circuit condition with a saturation current J_{sat} ($P=J_{ph\ at\ SC}/J_{sat}$). The results show that the dissociation probability showed almost no changes, 96% for binary device to 98% for device with 10% TPB, but decreased to 95% when 30% third component is added into the blend.

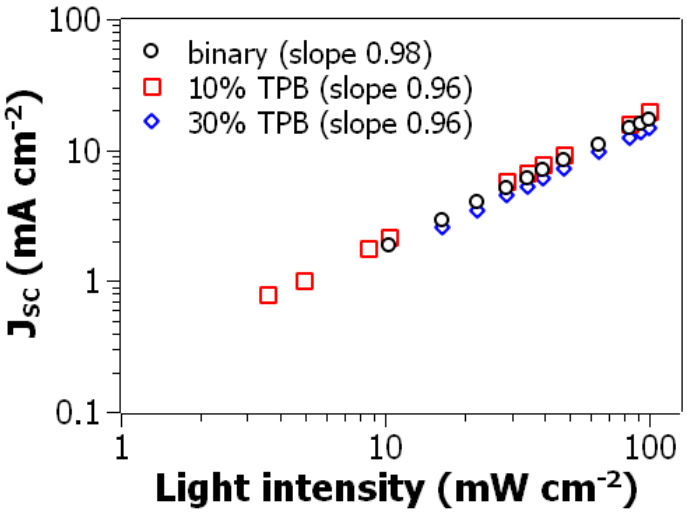

Figure 3.5. Plot of short circuit current density versus light intensity.

The third component also did not show a significant influence on the bimolecular recombination of the charge carriers. Under varying light intensity, the dependence of J_{SC} on incident light power will be linear if no significant bimolecular recombination is present and non-linear due to an increased charge loss through recombination. Figure 3.5 shows the logarithmic plot of J_{SC} vs light intensity, from which slopes >0.95 can be deduced for both binary and ternary devices. The results showed weak bimolecular recombination for these OPV

systems. A slight decrease is observed from 0.98 to 0.96 when the third component is added, which is consistent with a slight FF decrease as observed in OPV properties.

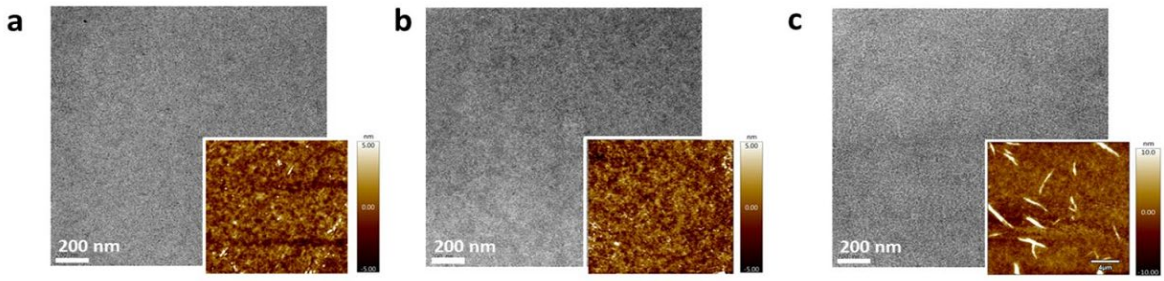

Figure 3.6. a) TEM and AFM ($10\mu m \times 10\mu m$) images of binary film PTB7-Th:$PC_{71}BM$. b) TEM and AFM ($10\mu m \times 10\mu m$) images of ternary film with 10% of TPB. c) TEM and AFM ($20\mu m \times 20\mu m$) images of ternary film with 30% of TPB.

3.2.3 Surface Properties

Transmission electron microscopy (TEM) and atomic force microscopy (AFM) were employed to investigate the binary and ternary blend film morphology, and the data are summarized in Figure 3.6 It is observed that all blends form desired bulk heterojunction network that is beneficial for OPV performance. The addition of 10% TPB does not affect the film morphologies significantly as fibril-like structures (approximately 20 nm) are observed in both binary and 10% ternary devices. The surface roughness RMS obtained from the AFM measurements is also similar, exhibiting the values of 1.3 nm and 1.4 nm, respectively. However, upon the increase of TPB content up to 30% by mass, larger aggregates are formed on the surface of the blend (Figure 3c AFM image inset) and the surface roughness RMS value increases up to 7.9 nm, indicating changes in the film morphology, which deteriorate the device performance.

We investigated surface properties further and measured surface energies of neat materials PTB7-Th, TPB and $PC_{71}BM$. We measured contact angle in a series of solvents

(water, diiodomethane and ethylene glycol) on the surface of these materials in air and from there calculated surface energies. As shown in Table 3.4 surface energy for PTB7-Th is 34.40 mN/m, for TPB 43.43 mN m^{-1} and for $PC_{71}BM$ 46.71 mN/m. For every pair of blend's components, we calculated interfacial surface energies using Neumann's equation (Table 3.5). For PTB7-Th/$PC_{71}BM$ interfacial surface energy was 2.325 mN/m, for PTB7-Th/TPB 1.255 mN/m and for TPB/$PC_{71}BM$ 0.168 mN/m. Surface energy and material's wetting coefficients are used as indicators which allow determining the sensitizer's location in a ternary blend.[29–31] If the wetting coefficient of a third component is larger than 1 or smaller than -1, it is preferentially located in one of the blend's main component's phases. However, the wetting coefficient's value within a range from -1 to +1 indicates the preferential location of the third component is at the interface between two main components. Therefore, we calculated TPB's wetting coefficient in PTB7-Th/PCBM blend using Young's equation. For TPB wetting coefficient in PTB7-Th/$PC_{71}BM$ blend is 0.47, indicating its preferential orientation at the interfaces between PTB7-Th and $PC_{71}BM$ domains.

3.2.4 Film Morphology Studies

We also measured 2D grazing incidence wide-angle x-ray scattering (GIWAXS) of films with 0, 10 and 30% TPB additive, and the data and linecuts were shown in Figure 3.7. There are several main diffraction peaks observed in a GIWAXS pattern. A broad arc-like scattering near q = 0.3 $Å^{-1}$ originates from the Bragg diffraction of periodic PTB7-Th lamellar layers, whereas a peak at q_z=1.6 $Å^{-1}$ that is absent in q_y direction appears from out-of-plane π-π stacking and has a preferential face-on orientation. A broad peak near q=1.4 $Å^{-1}$ originates from a $PC_{71}BM$

diffraction and appears both in out-of-plane and in-plane directions, which suggests a lack of preferential orientation and rather amorphous structure.

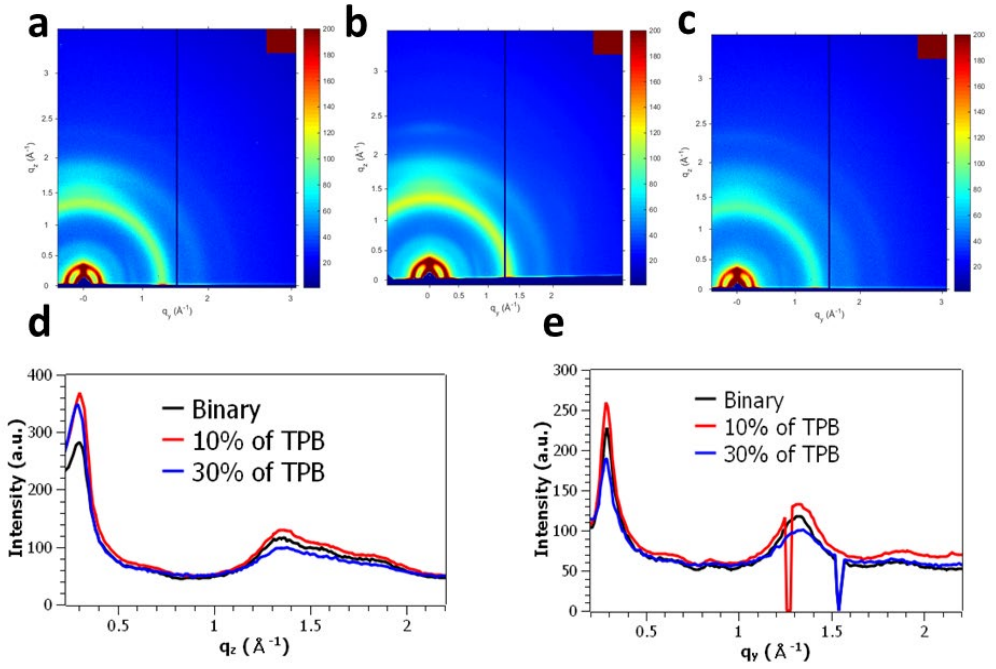

Figure 3.7. GIWAXS 2D patterns for a) binary blend, b) blend with 10% TPB, c) blend with 30% TPB. GIWAXS linecuts for d) out-of-plane q_z direction. e) in-plane q_y direction.

When the third component of 10% is added into a blend, an increase in the intensity of these peaks was observed, which suggests an increase in crystallinity of PTB7-Th and $PC_{71}BM$ phases. This conclusion is further supported by Scherer fitting analysis of the peaks (Table 3.3), where correlation length for out-of-plane lamellar peak increased from 49 Å for binary blend to 52Å for ternary blend, which suggests an increased crystallinity in the blend. Similar trends were observed in the in-plane direction. However, the in-plane lamellar peak intensity is

significantly reduced after increasing the TPB content to 30%, while out-of-plane lamellar peak is almost unchanged. This result indicates high TPB contents are not favorable for polymer PTB7-Th taking a face-on orientation, which could harm OPV performance. The drop of $PC_{71}BM$ peak's diffraction intensity is also observed, which indicates $PC_{71}BM$ phase is disrupted. The in-plane lamellar PTB7-Th diffraction peak for binary and 10% ternary blend was observed at 0.290 $Å^{-1}$, which corresponds to d-spacing of 21.7 Å, while 30% third component shifts the peak down a little bit, with a d-spacing of 22.1 Å. Similar trends are observed in out-of-plane direction, where lamellar distance contracts slightly when 10% TPB is present in a film (from 21.9 Å to 21.5 Å) and then expands to 22.1 Å when 30% TPB is added. The shorter polymer lamellar spacing indicates more close packing of the donor polymer, which should be beneficial for more efficient hole transport.

3.2.5 Proposed Model

From these studies discussed above, we propose a model (Figure 3.8) to explain the role that TPB plays in ternary PTB7-Th/$PC_{71}BM$ solar cells. The TPB molecule has a cross-like molecular geometry with four PDI moieties connected to BDT core. When a small amount (10%) of TPB is added to the binary PTB7-Th/$PC_{71}BM$ solar cells, TPB preferentially stays at the interfaces between PTB7-Th and $PC_{71}BM$, as indicated by its wetting coefficient. Excitons generated in PTB7-Th phase dissociate at the interface and electrons are transferred to TPB via charge transfer mechanism, as indicated by quenching of polymer film photoluminescence. The TPB at low concentration did not interrupt the binary system significantly but enhanced the performances. Due to its favorable cross-like molecular geometry, TPB served as an electronic relay bridge between polymer and $PC_{71}BM$ domains, thus improving connectivity between two

phases. Especially four partially conjugated PDI moieties facilitate charge separation by offering multiple charge transferring sites, which result in much higher J_{sc} values. In addition, each TPB molecule has multiple contact points with $PC_{71}BM$ where charge hopping can occur efficiently from TPB to $PC_{71}BM$, or from $PC_{71}BM$ to TPB because they have nearly identical LUMO energy level, leading to the higher electron mobility due to improved connectivity after 10% TPB was added.[32]

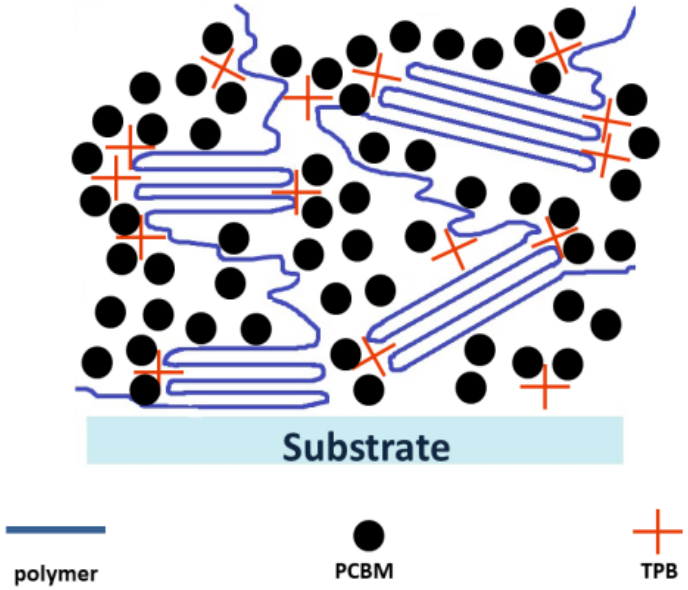

Figure 3.8. Schematic presentation of ternary blends where TPB serves as a linker between polymer and $PC_{71}BM$ phases.

3.3 Conclusions

A non-fullerene acceptor TPB was investigated as a third component in bulk heterojunction devices based on PTB7-Th and $PC_{71}BM$. It was observed that the performance of ternary devices was enhanced when 10% of TPB is added into a blend, resulting in PCE value

of 10.6% for the best performing device. The observed enhancement was mostly attributed to an increase in short-circuit current of the device, originating from more efficient charge separation, increased light harvesting and increased charge mobility. A model was suggested, in which the TPB serves as an electronic relay bridge, facilitating electron transfer from polymer to $PC_{71}BM$ phase. Four PDI units surrounding TPB's core provide multiple contact points between two phases, thus facilitating interfacial charge extraction and improving overall device performance. The model is further supported by measurements of the interfacial surface energies that indicate TPB's preferential location at the interface between PTB7-Th and $PC_{71}BM$.

3.4. Experimental Section

Materials used

Polymer PTB7-Th was purchased from company 1-Material Inc., fullerene-based acceptor $PC_{71}BM$ was purchased from American Dye Source Inc. Small molecule acceptor TPB was synthesized by Dr. Qinghe Wu in Prof. Luping Yu lab following procedures reported elsewhere.[26] Chlorobenzene, 1.8-diiodooctane, $Zn(CH_3COO)_2{\cdot}2H_2O$, 2-methoxyethanol and 2-aminoethanol all purchased from Sigma-Aldrich. All chemicals were used as obtained from the manufacturer.

Device fabrication

Devices were fabricated in inverted configuration ITO/ZnO/active layer/MoO_3/Ag. ITO substrates, purchased from Thin Film Devices Inc. were ultrasonicated in chloroform, acetone and isopropanol for 15 min and then treated with UV-ozone for 30 min. Sol-gel precursor solution of ZnO containing $Zn(CH_3COO)_2{\cdot}2H_2O$ in 2-methoxyethanol and 2-aminoethanol was

prepared following procedures described elsewhere.[28] To form a film of ZnO the solution was added dropwise onto ITO substrates through PTFE syringe filter and spin-coated at 4000 rpm for 40 seconds. Films were annealed in air immediately after spin coating at 200^0C for 30 minutes. Polymer and small molecule acceptors were dissolved in a chlorobenzene:DIO (97:3 vol %) overnight and solution was spin-coated onto the substrates at 70^0 C in a glovebox. Films were immediately transferred to a vacuum chamber and MoO_3 (8 nm) and Ag (80 nm) were thermally evaporated under the pressure lower than 2×10^{-6} Torr.

Device characterization

J-V curves of the devices were measured with a source meter unit model Keithley 2420. Devices were tested in nitrogen glovebox under 1 sun conditions (AM1.5G, 100 mW cm^{-2}) using xenon lamp (Oriel 69920) intensity of which was calibrated with a standard NREL certified Si cell (Newport, 91150V). Masks with a well-defined area of 3.14 mm^2 were used to define an active area of the device. Devices for EQE were sealed using UV curable Norland optical adhesive and measured outside of the glovebox. EQE was measured with a Newport QE measurement system (IQE-200) with a tungsten halogen lamp as a light source. To measure light intensity-dependent properties a series of neutral density filters was used. To measure charge carrier mobility hole-only devices were fabricated with a structure ITO/PEDOT/active layer/MoO_x/Ag and electron-only device ITO/ZnO/active layer/Ca/Al. JV curves were measured in dark from 0 to 10V and SCLC region was fitted with a Mott-Gurney law equation $J=(9\varepsilon\varepsilon_0\mu(V_{app}-V_{bi})^2/(8L^3)$ where J – current density, ε – dielectric constant of the medium (assumed value 3), μ-mobility, L-thickness. UV/Vis spectra were obtained with Shimadzu UV-2401PC spectrophotometer. PL spectra were obtained with Horiba FluoroLog-3 fluorometer.

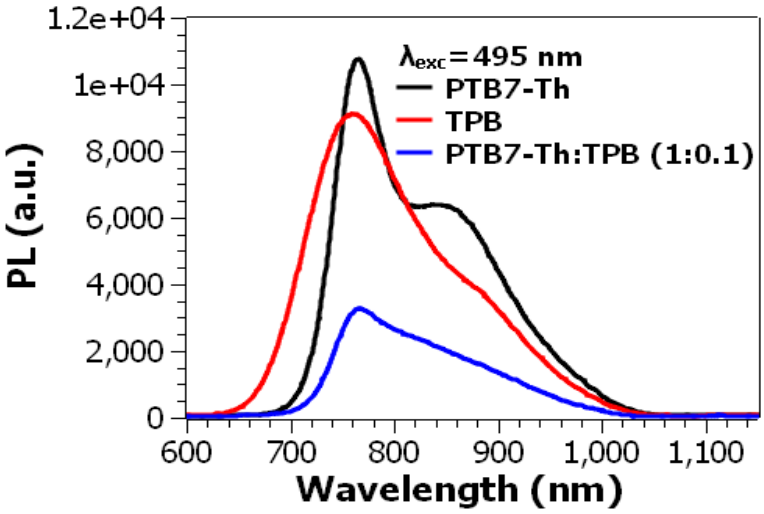

Figure 3.9. Photoluminescence spectra for PTB7-Th, TPB and a blend with PTB7-Th:TPB (1:0.1 by mass).

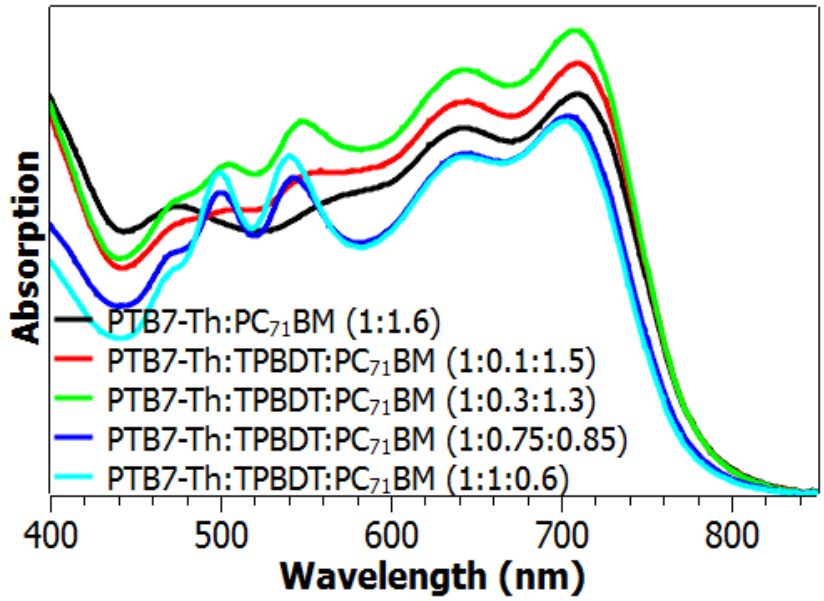

Figure 3.10. UV/Vis light absorption spectra for OPV devices with varying ratio of TPBDT:PC71BM (normalized with thickness).

Table 3.2. Summary of solar cell parameters for devices with varying ratio of TPB:$PC_{71}BM$.

PTB7-Th:TPB:$PC_{71}BM$ [1:x:y]	V_{OC} [V]	J_{SC} [mA cm^{-2}]	FF [%]	$PCE^{average}$ [%]	PCE^{max} [%]
1:0:1.6	0.78±0.01	16.05±0.35	71±0.35	8.9±0.2	9.2
1:0.1:1.5	0.78±0.01	19.44±0.25	68±1.39	10.2±0.2	10.6
1:0.3:1.3	0.78±0.01	15.95±0.36	68±0.19	8.5±0.2	8.7
1:0.75:0.85	0.80±0.01	14.97±0.25	65±0.48	7.8±0.1	7.9
1:1:0.6	0.81±0.01	14.68±0.31	63±0.22	7.5±0.1	7.6

Morphology studies.

TEM measurements were performed with Tecnai F30 microscope. AFM studies were made with Asylum Cyfer microscope at the University of Chicago MRSEC MPML facilities. AFM was measured in a tapping mode using Arrow UHF tip. The GIWAXS measurements were performed at 8ID-E beamline of Advanced Photon Source, Argonne National Laboratory with a radiation wavelength 1.1364 Å. Samples for GIWAXS were prepared on polished Si wafer, covered with ZnO and coated with an active layer film being studied. Scherer analysis of GIWAXS data was conducted where linecut peaks were fitted with pseudo-Voigt function to determine peak's position and full width at half maximum (FWHM).

Table 3.3 Summary of GIWAXS parameters obtained from Scherrer analysis of linecut peaks

Content of TPB [weight %]	q_y [$Å^{-1}$]	d_y [Å]	Δq_y [$Å^{-1}$]	D_L [Å]	q_z [$Å^{-1}$]	d_z [Å]	Δq_z [$Å^{-1}$]	D_L [Å]
0%	0.290	21.66	0.078	72.55	0.287	21.89	0.116	48.78
10%	0.290	21.66	0.063	89.82	0.292	21.51	0.109	51.91
30%	0.284	22.12	0.088	64.37	0.284	22.12	0.108	52.39

q – position of a peak obtained from 2D GIWAXS linecut, d – spacing ($\mathbf{d} = \frac{\mathbf{2\pi}}{\mathbf{q}}$), Δq – peak's full width at half maximum (FWHM), D_L – coherence length determined through Scherrer analysis.

Surface energy measurements.

Contact angle measurements were performed on pristine films of PTB7-Th, $PC_{71}BM$ and TPB using drop shape analyzer DSA-100 from Krüss GmbH at the University of Chicago MRSEC MPML. Experiments were conducted in air at room temperature for ultrapure 18MΩ water, diiodomethane and ethylene glycol. Software provided with the machine was used to analyze data and calculate surface energies for these materials using the OWRK (Owens, Wendt, Rabel and Kaelble) model. Procedures adapted from the literature were followed in calculations of surface energy of these materials.[30] Neumann's equation was used to calculate interfacial surface energies for pairs of PTB7-Th/PCBM, PTB7-Th/TPB and TPB/PCBM.

$$\boldsymbol{\gamma_{AB} = \gamma_A + \gamma_B - 2\sqrt{\gamma_A \cdot \gamma_B} \cdot \exp(-\beta \cdot (\gamma_A - \gamma_B)^2}$$

Where γ_A and γ_B are surface energies of materials forming an interface under consideration, γ_{AB} is interfacial surface energy between materials A and B, β is equal to 0.000115 m^4 mJ^{-2}. Young's equation was used to calculate wetting coefficient of TPB in PTB7-Th/PCBM blend.

$$\boldsymbol{\omega_{TPB} = \frac{\gamma_{TPB/PTB7Th} - \gamma_{TPB/PCBM}}{\gamma_{PTB7Th/PCBM}}}$$

Table 3.4. Measured contact angles and calculated surface energies for PTB7-Th, $PC_{71}BM$ and TPB films.

Material	Contact angle [^{0}]			Surface energy [mN/m]
	Water	Diiodomethane	Ethylene glycol	
PTB7-Th	100.71	49.05	75.88	34.40
$PC_{71}BM$	98.02	22.55	67.49	46.71
TPB	93.40	31.72	67.79	43.46

Table 3.5. Calculated interfacial surface energies PTB7-Th, $PC_{71}BM$ and TPB films.

Interface	Interfacial surface energy [mN/m]
PTB7-Th/ $PC_{71}BM$	2.325
PTB7-Th/TPB	1.255
TPB/$PC_{71}BM$	0.168

.

3.5 References

(1) Nian, L.; Gao, K.; Liu, F.; Kan, Y.; Jiang, X.; Liu, L.; Xie, Z.; Peng, X.; Russell, T. P.; Ma, Y. 11% Efficient Ternary Organic Solar Cells with High Composition Tolerance via Integrated Near-IR Sensitization and Interface Engineering. *Adv. Mater.* **2016**, *28*, 8184–8190.

(2) Zhang, G.; Zhang, K.; Yin, Q.; Jiang, X.; Zhang, G.; Zhang, K.; Yin, Q.; Jiang, X.; Wang, Z.; Xin, J.; *et al.* High-Performance Ternary Organic Solar Cell Enabled by a Thick Active Layer Containing a Liquid Crystalline Small Molecule Donor. *J. Am. Chem. Soc.* **2017**, *139*, 2387–2395.

(3) Zhao, J.; Li, Y.; Yang, G.; Jiang, K.; Lin, H.; Ade, H.; Ma, W.; Yan, H. Efficient Organic Solar Cells Processed from Hydrocarbon Solvents. *Nat. Energy* **2016**, *1*, 15027.

(4) Dai, S.; Zhao, F.; Zhang, Q.; Lau, T.-K.; Li, T.; Liu, K.; Ling, Q.; Wang, C.; Lu, X.; You, W.; *et al.* Fused Nonacyclic Electron Acceptors for Efficient Polymer Solar Cells. *J. Am. Chem. Soc.* **2017**, *139*, 1336–1343.

(5) Baran, D.; Ashraf, R. S.; Hanifi, D. A.; Abdelsamie, M.; Gasparini, N.; Röhr, J. A.; Holliday, S.; Wadsworth, A.; Lockett, S.; Neophytou, M.; *et al.* Reducing the Efficiency-Stability-Cost Gap of Organic Photovoltaics with Highly Efficient and Stable Small Molecule Acceptor Ternary Solar Cells. *Nat. Mater.* **2017**, *16*, 363–369.

(6) Park, K. H.; An, Y.; Jung, S.; Park, H.; Yang, C. The Use of an N-Type Macromolecular Additive as a Simple yet Effective Tool for Improving and Stabilizing the Performance of Organic Solar Cells. *Energy Environ. Sci.* **2016**, *107*, 1324.

(7) Zhao, W.; Li, S.; Yao, H.; Zhang, S.; Zhang, Y.; Yang, B.; Hou, J. Molecular Optimization Enables over 13% Efficiency in Organic Solar Cells. *J. Am. Chem. Soc.* **2017**, *139*, 7148–7151.

(8) Lu, L.; Kelly, M. A.; You, W.; Yu, L. Status and Prospects for Ternary Organic

Photovoltaics. *Nat. Photonics* **2015**, *9*, 491–500.
(9) An, Q.; Zhang, F.; Zhang, J.; Tang, W.; Deng, Z.; Hu, B. Versatile Ternary Organic Solar Cells: A Critical Review. *Energy Environ. Sci.* **2015**, *25*.
(10) Savoie, B. M.; Dunaisky, S.; Marks, T. J.; Ratner, M. a. The Scope and Limitations of Ternary Blend Organic Photovoltaics. *Adv. Energy Mater.* **2015**, *5*, 1400891.
(11) Ameri, T.; Khoram, P.; Min, J.; Brabec, C. J. Organic Ternary Solar Cells: A Review. *Adv. Mater.* **2013**, *25*, 4245–4266.
(12) Lu, L.; Xu, T.; Chen, W.; Landry, E. S.; Yu, L. Ternary Blend Polymer Solar Cells with Enhanced Power Conversion Efficiency. *Nat. Photonics* **2014**, *8*, 716–722.
(13) Lu, L.; Chen, W.; Xu, T.; Yu, L. High-Performance Ternary Blend Polymer Solar Cells Involving Both Energy Transfer and Hole Relay Processes. *Nat. Commun.* **2015**, *6*, 7327.
(14) Khlyabich, P. P.; Burkhart, B.; Thompson, B. C. Efficient Ternary Blend Bulk Heterojunction Solar Cells with Tunable Open-Circuit Voltage. *J. Am. Chem. Soc.* **2011**, *133*, 14534–14537.
(15) Cheng, P.; Li, Y.; Zhan, X. Efficient Ternary Blend Polymer Solar Cells with Indene-C60 Bisadduct as an Electron-Cascade Acceptor. *Energy Environ. Sci.* **2014**, *7*, 2005.
(16) Xu, X.; Li, Z.; Wang, Z.; Li, K.; Feng, K.; Peng, Q. 10.20% Efficiency Polymer Solar Cells via Employing Bilaterally Hole-Cascade Diazaphenanthrobisthiadiazole Polymer Donors and Electron-Cascade Indene-C70 Bisadduct Acceptor. *Nano Energy* **2016**, *25*, 170–183.
(17) Zhang, J.; Zhao, Y.; Fang, J.; Yuan, L.; Xia, B.; Wang, G.; Wang, Z.; Zhang, Y.; Ma, W.; Yan, W.; *et al.* Enhancing Performance of Large-Area Organic Solar Cells with Thick Film via Ternary Strategy. *Small* **2017**, *13*, 1–8.
(18) An, Q.; Zhang, F.; Sun, Q.; Zhang, M.; Zhang, J.; Tang, W.; Yin, X.; Deng, Z. Efficient Organic Ternary Solar Cells with the Third Component as Energy Acceptor. *Nano Energy* **2016**, *26*, 180–191.
(19) Lu, H.; Zhang, J.; Chen, J.; Liu, Q.; Gong, X.; Feng, S.; Xu, X.; Ma, W.; Bo, Z. Ternary-Blend Polymer Solar Cells Combining Fullerene and Nonfullerene Acceptors to Synergistically Boost the Photovoltaic Performance. *Adv. Mater.* **2016**, *28*, 9559–9566.
(20) Liu, T.; Guo, Y.; Yi, Y.; Huo, L.; Xue, X.; Sun, X.; Fu, H.; Xiong, W.; Meng, D.; Wang, Z.; *et al.* Ternary Organic Solar Cells Based on Two Compatible Nonfullerene Acceptors with Power Conversion Efficiency >10%. *Adv. Mater.* **2016**, *28*, 10008–10015.
(21) Zhang, Y.; Deng, D.; Lu, K.; Zhang, J.; Xia, B.; Zhao, Y.; Fang, J.; Wei, Z. Synergistic Effect of Polymer and Small Molecules for High-Performance Ternary Organic Solar Cells. *Adv. Mater.* **2015**, *27*, 1071–1076.
(22) Goh, T.; Huang, J. S.; Yager, K. G.; Sfeir, M. Y.; Nam, C. Y.; Tong, X.; Guard, L. M.; Melvin, P. R.; Antonio, F.; Bartolome, B. G.; *et al.* Quaternary Organic Solar Cells Enhanced by Cocrystalline Squaraines with Power Conversion Efficiencies >10%. *Adv. Energy Mater.* **2016**, *6*, 1600660.
(23) Cnops, K.; Rand, B. P.; Cheyns, D.; Verreet, B.; Empl, M. A.; Heremans, P. 8.4% Efficient Fullerene-Free Organic Solar Cells Exploiting Long-Range Exciton Energy Transfer. *Nat. Commun.* **2014**, *5*, 3406.
(24) Zhao, F.; Luo, X.; Liu, J.; Du, L.; Lv, W.; Sun, L.; Li, Y.; Wang, Y.; Peng, Y. Toward High Performance Broad Spectral Hybrid Organic–inorganic Photodetectors Based on

Multiple Component Organic Bulk Heterojunctions. *J. Mater. Chem. C* **2016**, *4*, 815–822.
(25) Liu, T.; Xue, X.; Huo, L.; Sun, X.; An, Q.; Zhang, F.; Russell, T. P.; Liu, F.; Sun, Y. Highly Efficient Parallel-Like Ternary Organic Solar Cells. *Chem. Mater.* **2017**, *29*, 2914–2920.
(26) Wu, Q.; Zhao, D.; Schneider, A. M.; Chen, W.; Yu, L. Covalently Bound Clusters of Alpha-Substituted PDI-Rival Electron Acceptors to Fullerene for Organic Solar Cells. *J. Am. Chem. Soc.* **2016**, *138*, 7248–7251.
(27) Wu, Q.; Zhao, D.; Goldey, M. B.; Filatov, A. S.; Sharapov, V.; Colon, Y. J.; Cai, Z.; Chen, W.; de Pablo, J. J.; Galli, G.; Yu, L. Intra-Molecular Charge Transfer and Electron Delocalization in Non-Fullerene Organic Solar Cells. *ACS Appl. Mater. Interfaces* **2018**, *10*, 10043–10052.
(28) Lee, B. R.; Jung, E. D.; Nam, Y. S.; Jung, M.; Park, J. S.; Lee, S.; Choi, H.; Ko, S.-J.; Shin, N. R.; Kim, Y.-K.; *et al.* Amine-Based Polar Solvent Treatment for Highly Efficient Inverted Polymer Solar Cells. *Adv. Mater.* **2014**, *26*, 494–500.
(29) Honda, S.; Ohkita, H.; Benten, H.; Ito, S. Selective Dye Loading at the Heterojunction in Polymer/Fullerene Solar Cells. *Adv. Energy Mater.* **2011**, *1*, 588–598.
(30) Ameri, T.; Khoram, P.; Heumüller, T.; Baran, D.; Machui, F.; Troeger, A.; Sgobba, V.; Guldi, D. M.; Halik, M.; Rathgeber, S.; *et al.* Morphology Analysis of near IR Sensitized Polymer/fullerene Organic Solar Cells by Implementing Low Bandgap Heteroanalogue C-/Si-PCPDTBT. *J. Mater. Chem. A* **2014**, *2*, 19461–19472.
(31) Zhu, Y.; Chen, Y.; Zhao, S.; Huang, Y.; Xu, Z.; Qiao, B.; Zhao, J.; Li, Y.; Liu, J.; Xu, X. The Effects of SQ Additive on Charge Carrier Transport and Recombination in PCDTBT:PC71BM Based Ternary Organic Solar Cells. *Synth. Met.* **2017**, *234*, 125–131.
(32) Foster, S.; Deledalle, F.; Mitani, A.; Kimura, T.; Kim, K. B.; Okachi, T.; Kirchartz, T.; Oguma, J.; Miyake, K.; Durrant, J. R.; *et al.* Electron Collection as a Limit to polymer:PCBM Solar Cell Efficiency: Effect of Blend Microstructure on Carrier Mobility and Device Performance in PTB7:PCBM. *Adv. Energy Mater.* **2014**, *4*, 1400311.

CHAPTER 4

REDUCED DARK CURRENT IN ORGANIC PHOTODETECTORS BASED ON TERNARY BULK HETEROJUNCTION BLENDS WITH SMALL MOLECULE ACCEPTOR TCN-BDT AS A THIRD COMPONENT

4.1 Introduction and Background

Photodetectors (PDs) are an important part of the modern world especially with the development of next-generation of technologies for various sensors, ranging from smart vision to biosensing and machine vision.[1,2] Many different types of photodetectors exist, covering a wide range of wavelengths and response speeds.[3–5] For example, PDs based on Si are widely used for UV/visible detection and those based on InGaAs and PbS are suitable for near-IR and IR range. Although these detectors are manufactured in industrial scale and widely used in different areas, there are still critical drawbacks that call for better solution, such as high cost for purification of inorganic materials (Si), usage of toxic elements (such as As in InGaAs or InAsSb or Pb in PbS), and often need for external cooling, especially for IR photodetectors. Therefore, organic or hybrid materials become a viable alternative to the existing systems.[1,6,7] Superior mechanical properties of organic materials (especially polymers) are a welcome bonus, which may allow for flexible lightweight devices that work under significant mechanical stress.[8–10]

The performance of any photodetector is characterized by a set of critical parameters, including dark current (J_d), current under illumination (J_{ph}), response time (t_{res}) and also a set of derived parameters, such as responsivity (R), specific detectivity (D^*), noise equivalent power

(NEP) and linear dynamic range (LDR).[4] The dark current is one of the most important parameters for these devices that defines their sensitivity. For the most sensitive devices, the ratio of signal under illumination to signal in dark must be maximized. Therefore, lowering dark current is a critical step in developing high-efficiency organic photodetector (OPD) devices.

Possible mechanisms for the origin of dark current include doping and impurities,[11] intrinsic charge carriers and charge injection from the electrodes.[12] In addition, various trap states and defects,[13] whether intrinsic (originating from irregularities in molecular structure and disordered packing), or extrinsic (originating from impurities, oxygen and moisture) significantly contribute to dark current.[14–16] Since organic semiconducting materials are almost always disordered systems, many of these dark current mechanisms may co-operate simultaneously in OPD devices.

Different approaches have been developed to lower the dark current in OPD devices. The most commonly used are methods involving photoactive materials design and device engineering. Careful engineering of the chemical structures of materials has led to reduction in dark current. [17–24] It was also shown that controls in polymer chains orientation in edge-on fashion on the surface of the device decreases dark current due to insulating effect of polymer alkyl side chains.[25] Incorporation of 3,4-ethylenedioxythiophene (EDOT) fragments into polymer side chains can increase the interaction of polymer chain with PEDOT/PSS hole transporting layer, resulted in a vertical phase separation with the polymer being concentrated near PEDOT. This vertical distribution resulted in formation of polymer-rich electron blocking layer near the PEDOT and fullerene reach hole blocking layer near the metal electrode thus reducing dark current in the device.[26] Non-fullerene acceptor materials were also developed for

low dark current devices. Thus, it was shown that rigid circular PDI based acceptor molecule cP_4 gives devices with decreased dark current, compared to devices with its non-cyclic counterpart aP_n or fullerene-based $PC_{71}BM$.[27]

Incorporation of various interfacial layers is another effective approach to decrease the dark current. These interfacial layers are used to block unwanted charge injections at the relevant electrode (hole injection is blocked at the electron collecting electrode and vice versa).[28] Polyelectrolytes were used to block holes at ZnO/$PC_{71}BM$ interface in devices with inverted architecture.[29] A stamp transferred P3HT layer on the top of the device's active layer was used to block electron injection due to its higher-lying LUMO.[30] The MoO_x interlayer was treated with plasma to control gap states.[31] Another frequently adapted approach to the reduction of dark current is fabrication of thicker devices.[32] Unfortunately, this approach works only for materials with high charge carrier mobility, otherwise, low photocurrent will offset the benefits.[33]

Despite intensive research efforts, there is still a very limited choice of effective methods to reduce the dark current in organic photodetector devices. Even for those devices with low dark current, a trade-off between dark current and responsivity often occurs.[1] In this chapter we present an approach of using ternary bulk heterojunction blends to reduce dark current in OPD devices while maintaining high photocurrent and thus high EQE. A new small molecule acceptor TCN-BDT was presented in Chapter 2. Here we use it as a third component in bulk heterojunctions blends with PTB7-Th and $PC_{71}BM$.

4.2. Results and Discussion

4.2.1 Materials and Characterization of Basic Properties

The main binary blend consisted of donor polymer PTB7-Th and $PC_{71}BM$ (Figure 4.1a). The light absorption spectra of all three blend components are shown in Figure 4.1b. Combined absorption spectra of acceptors are complementary to absorption of the donor polymer, resulted in devices with wide wavelength coverage from the blue region at 300 nm to about 800 nm in NIR. HOMO and LUMO energy levels of blend components were measured with CV and shown in Figure 4.1c.

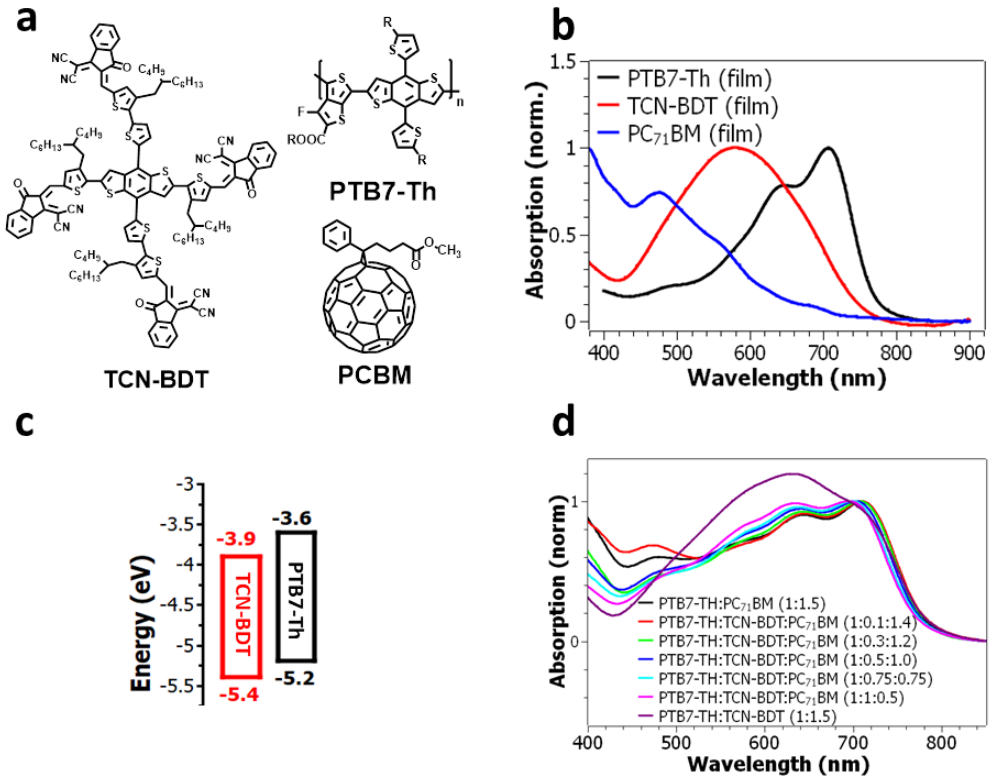

Figure 4.1. a) Molecular structure of PTB7-Th (R-2ethylhexyl), $PC_{71}BM$ and TCN-BDT; b) Absorption spectra of PTB7-Th, $PC_{71}BM$ and TCN-BDT films; c) Energy diagram of HOMO and LUMO energy levels of PTB7-Th, $PC_{71}BM$ and TCN-BDT calculated from CV measurements; d) Absorption spectra of binary and ternary blends.

The LUMO level of TCN-BDT is very close to LUMO level of $PC_{71}BM$ (-3.9 eV), while HOMO levels of all three components formed an energy cascade. Previous studies in ternary OPV devices suggested that such cascade facilitated a hole extraction from the excitons generated in $PC_{71}BM$ and improve device performance.[34,35]

4.2.2 Photovoltaic Properties

To test photoactivity, we fabricated a series of binary and ternary devices with different compositions and measured their photovoltaic performance under AM1.5G simulated illumination. The devices were made in an inverted configuration consisting of ITO/ZnO/active layer/MoOx/Ag. Photovoltaic efficiency parameters extracted from the *J-V* curves are shown in Table 4.1.

Table 4.1 Photovoltaic parameters for binary and ternary devices of various composition for PTB7-Th:TCN-BDT:PCBM (1:x:1.5-x)

TCN-BDT in acceptor phase [%]	V_{OC} [V]	J_{SC} [mA cm^{-2}]	FF [%]	PCE^{av} (max) [%]
0	0.79±0.00	16.00±0.59	68±2.0	8.5±0.2 (8.8)
6.6	0.78±0.01	16.80±0.29	67±1.0	8.9±0.3 (9.2)
20	0.79±0.00	16.05±0.39	69±0.0	8.6±0.2 (8.8)
33.3	0.78±0.00	16.24±0.68	66±0.0	8.4±0.4 (8.9)
50	0.78±0.00	15.78±0.02	64±1.0	7.8±0.1 (8.0)
66.6	0.76±0.00	16.47±0.20	63±2.0	7.9±0.2 (8.1)
100	0.77±0.00	15.43±0.33	61±1.0	7.2±0.2 (7.4)

Binary devices with PTB7-Th and $PC_{71}BM$ (1:1.5 by mass) demonstrated power conversion efficiency (PCE) of 8.5% with J_{SC} 16.0 mA cm^{-2}, V_{OC} 0.79 V and FF 68%. When a small amount of $PC_{71}BM$ was replaced with TCN-BDT (6.6% of total acceptor mass) the

efficiency slightly increased to 8.9% due to J_{SC} increase from 16.00 to 16.80 mA/cm^2; V_{OC} and FF stayed almost the same as for binary device – 0.78V and 67% respectively. When the amount of TCN-BDT was increased further, PCEs of the devices dropped mostly due to decreasing FF and eventually reached 7.2% for a binary fullerene-free device with PTB7-Th:TCN-BDT (1:1.5) with J_{SC} 15.43 mA cm^{-2}, V_{OC} 0.77 V and FF 61%. The EQE spectra are consistent with *J-V* results (Figure 4.2a). There are three recognizable peaks in the EQE spectrum of binary device, corresponding to absorption of $PC_{71}BM$ (around 450 nm) and two absorption maxima of a polymer (640nm and 720 nm). When $PC_{71}BM$ is gradually replaced with TCN-BDT, intensity of the absorption peak near 450 nm was reduced, while those in a region of 500-700 nm were increased, where TCN-BDT has its absorption maximum.

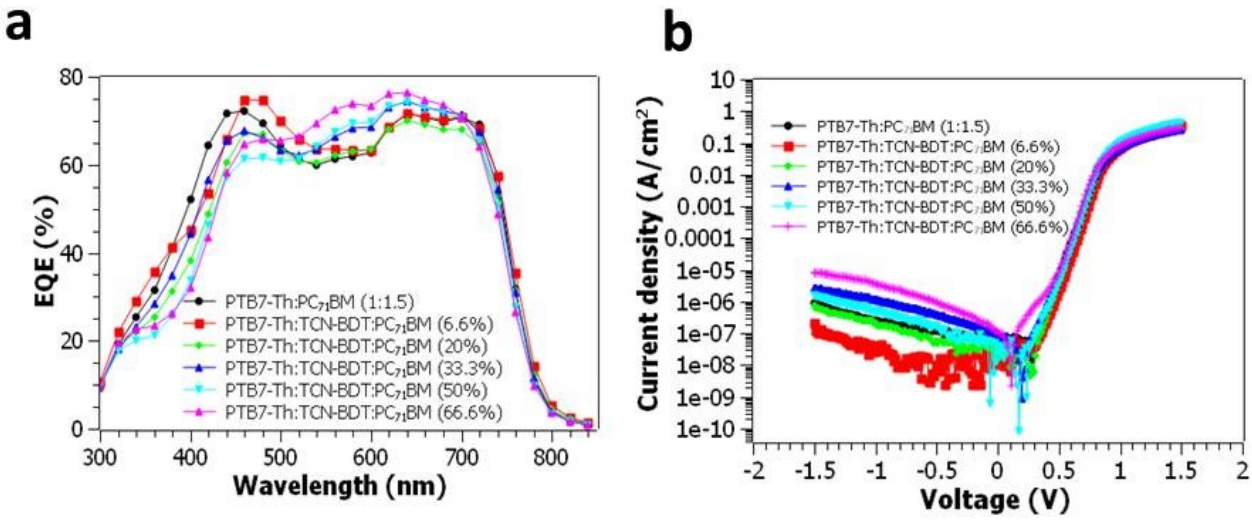

Figure 4.2. a) EQE spectrum for ternary and binary blends of varying composition; b) J-V curves for binary and ternary devices in semi-logarithmic form.

Table 4.2. Dark currents for binary and ternary systems of varying composition for PTB7-Th:TCN-BDT:PC71BM at -1 V bias.

TCN-BDT in acceptor phase (mass %)	J_d^{av} (A cm^{-2})	J_d^{best} (A cm^{-2})
0	1.26×10^{-6}	2.49×10^{-7}
6.6	6.69×10^{-8}	2.88×10^{-8}
20	2.70×10^{-7}	2.06×10^{-7}
33.3	1.53×10^{-6}	1.12×10^{-7}
50	9.34×10^{-7}	4.75×10^{-7}
66.6	3.66×10^{-6}	2.91×10^{-6}
100	6.17×10^{-7}	2.29×10^{-7}

These results are consistent with the absorption spectra of the blends (Figure 4.1d). The results of *J-V* measurements in dark are shown in Figures 4.2b and summarized in Table 4.2, and statistics is provided in Figure 4.8. The binary device exhibited an average dark current 1.26×10^{-6} A cm^{-2} at a bias voltage of -1 V. When a small molecule acceptor TCN-BDT was added in the place of $PC_{71}BM$ (6.6% of total acceptor mass), it was found that the dark current decreased almost 20 times to $6.69 \cdot 10^{-8}$ A cm^{-2} with the lowest value 2.88×10^{-8} A cm^{-2}. Due to increased photocurrent, the on-off ratio at -1 V increased from 1.32×10^{4} for the binary device to 2.68×10^{5} for ternary device, which indicated a higher sensitivity. When $PC_{71}BM$ is further replaced with TCN-BDT, an overall trend of increasing dark current was observed, with a slight drop for a binary device where 100% TCN-BDT was used as an acceptor in PTB7-Th:TCN-BDT (1:1.5) blend.

4.2.3 Photodetector Properties

Even though photovoltaic devices and photodetectors share similar operation principles, the characteristic figures of merit of these devices are different.

Responsivity is a parameter that describes the ratio of the device's photocurrent to power of incident light, which can be calculated from the EQE spectrum under bias:

$$R = EQE \cdot \frac{\lambda q}{hc}$$

where R – responsivity, EQE – external quantum efficiency, λ – wavelength, q – charge of electron, h – Planck constant, c – the speed of light. Figure 4.3 shows the resultant responsivity spectra.

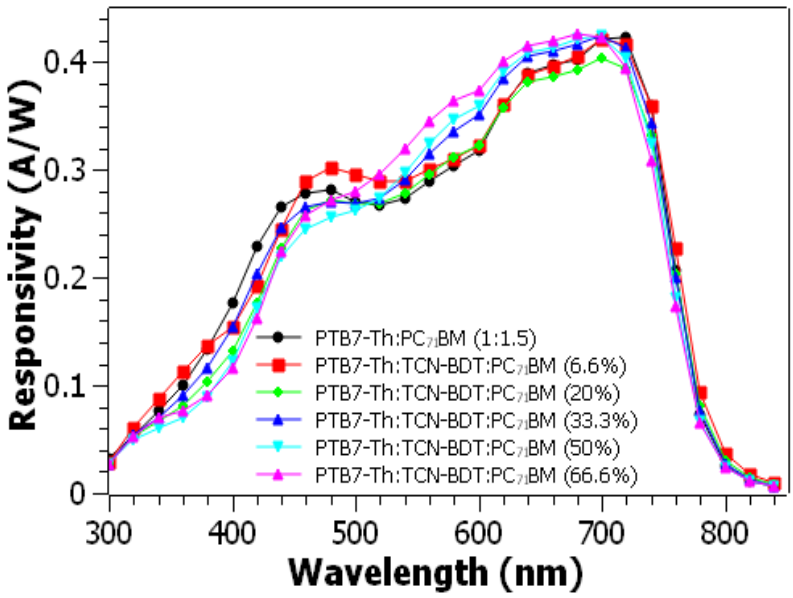

Figure 4.3. Responsivity spectrum for binary and ternary devices measured at -1V.

The responsivity of the binary device reached a maximum of 0.42 A/W at 720 nm. The maximum responsivity of the ternary device with 6.6% TCN-BDT in the acceptor phase is also 0.42 A W^{-1}, but shifted to 700 nm. A further shift to 680 nm was observed for responsivity

maxima of devices with higher loads of TCN-BDT. At the same time, gradual increase in responsivity is observed in the region of 500nm to 700 nm in ternary devices, corresponding to additional light harvesting from TCN-BDT. We used responsivity data to calculate specific detectivity in the binary and ternary photodetector devices.

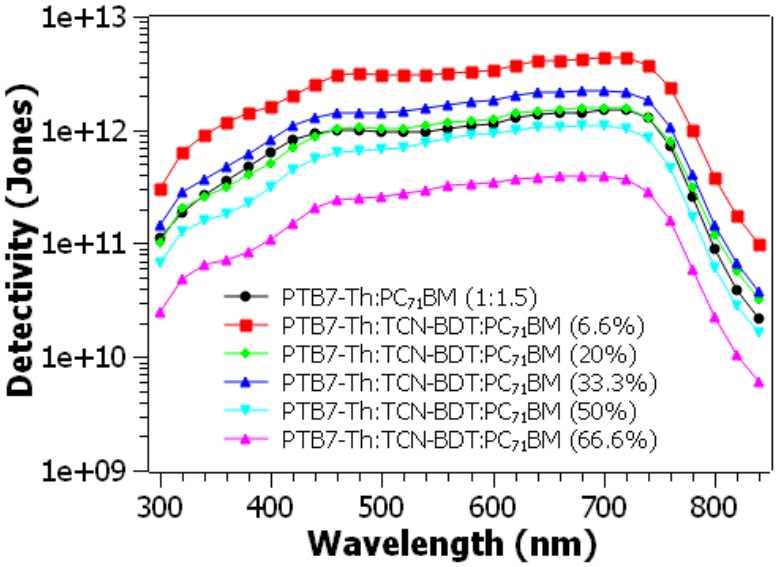

Figure 4.4. Specific detectivity spectrum for binary and ternary devices at -1V.

Figure 4.4 shows the specific detectivity of 1.5×10^{12} Jones at 720 nm for the binary device. This maximum value was increased to $4.4 \cdot 10^{12}$ Jones for ternary device with 6.6% TCN-BDT at 700 nm. This increase originates from a decreased dark current density in ternary device. As a load of third component increases, specific detectivities of the ternary devices drop to as low as 3.8×10^{11} Jones for the device with the highest load of the third component (66.6%).

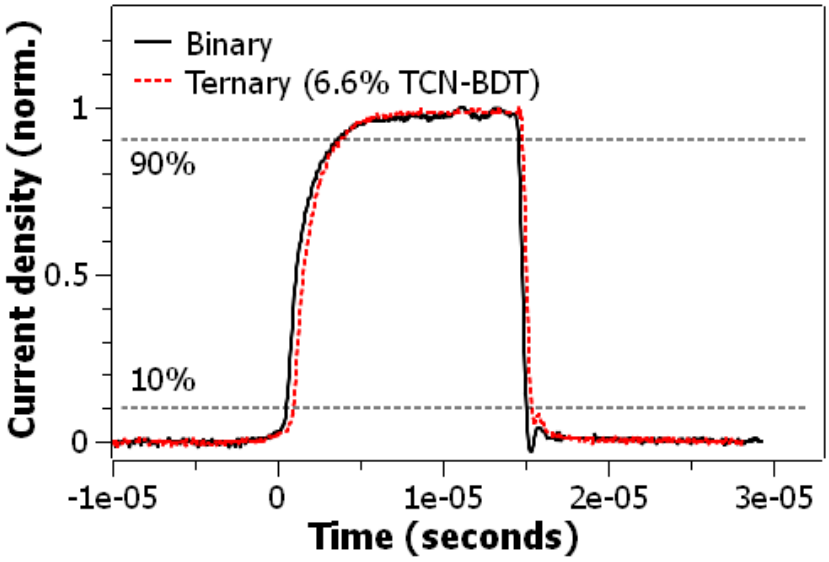

Figure 4.5. Transient photocurrent responses of binary and ternary photodetectors under -1 V bias for 25 kHz laser pulse at 650 nm.

A critical evaluation of the OPDs is their transient properties. Figure 4.5 shows normalized transient photocurrent response of binary and best ternary device with 6.6% TCN-BDT when illuminated with a 5 mW cm^{-2} laser at 650 nm (frequency 25.3 kHz). The signal rise time, t_r, (time that it takes for photocurrent to increase from 10% to 90% of a total signal) and fall time, t_f, (time that it takes for a signal to decrease from 90% to 10%) can be deduced from this graph. The rise and fall times of the binary device were 3.09 µs and 0.49 µs, respectively, while rise time of ternary device decreased to 2.48 µs and fall time slightly increased to 0.52 µs.

To further study dynamic properties, SCLC hole and electron mobility were measured by using a hole-only device with a structure ITO/PEDOT/active layer/MoO_x/Ag and electron-only device ITO/ZnO/active layer/Ca/Al for binary and ternary devices. Hole mobility of binary device was 3.8×10^{-5} $cm^2V^{-1}s^{-1}$ and increased to 4.6×10^{-5} $cm^2V^{-1}s^{-1}$ for the ternary

device with 6.6% TCN-BDT. These results are consistent with decreased rising time for ternary device, resulting in more sensitive organic photodetectors and slightly enhanced photovoltaic performance in ternary devices. At the same time electron mobility of binary devices is 3.7×10^{-5} $cm^2V^{-1}s^{-1}$ and it decreases to 2.9×10^{-5} $cm^2V^{-1}s^{-1}$ for ternary device with 6.6% TCN-BDT. Overall the mobility is quite balanced in the devices.

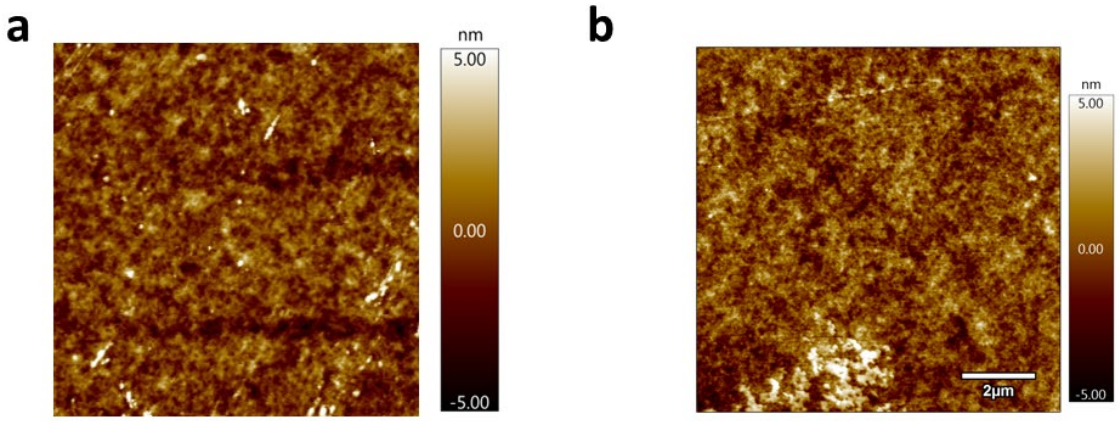

Figure 4.6. AFM images for a) binary and b) ternary blends with 6.6% TCN-BDT.

4.2.4 Surface Studies

To rationalize trends in the performance of binary and ternary devices, we studied their surface topography with AFM and its bulk molecular packing with GIWAXS. Figure 4.6 displays AFM images of the surface of binary and ternary devices with 6.6% TCN-BDT in acceptor phase, respectively. Surface roughness analysis showed minimum difference between binary and ternary blend surfaces, with the calculated RMS of 1.3 nm and 1.2 nm respectively. We studied materials' surface properties further and conducted interfacial surface energy measurements to determine location of the third component in the blend relative to the location

of the main components. For each of the materials PTB7-Th, TCN-BDT and $PC_{71}BM$ we measured surface energies and calculated interfacial surface energies for each pair of components (Tables 4.4). Using Young's equation we calculated wetting coefficient of TCN-BDT in a blend of PTB7-Th/$PC_{71}BM$ – a parameter that was used before to determine location of the third component in a blend (Table 4.5). If wetting coefficient is larger than 1 or smaller (more negative) than -1, this indicates preferential location of the third component in one of the main phases, however wetting coefficient from -1 to 1 indicates preferential location at the interface between two components.[36] For TCN-BDT the wetting coefficient was found to be -0.17, which indicates small molecule's preferential location at the polymer/$PC_{71}BM$ interface.

4.2.5 Morphology Studies

Figure 4.7 shows 2D diffraction GIWAXS patterns and 1D linecuts for binary and ternary blends. There are several recognizable peaks in the diffraction pattern. Polymer PTB7-Th has two distinct peaks in q_z direction at around 0.3 $Å^{-1}$, corresponding to periodic lamellar layers and near 1.6 $Å^{-1}$, corresponding to π-π stacks. There is only one distinct peak for polymer in q_y direction, near 0.3 $Å^{-1}$, while π-π stack peak is suppressed, indicating a preferential face-on orientation of the polymer chains. The broad scattering peak near 1.4 $Å^{-1}$ that is present in both out-of-plane and in-plane directions, originates from amorphous $PC_{71}BM$ aggregates. The Scherrer analysis of the linecut peaks was carried out to quantitatively analyze results (Table 4.3). The polymer lamellar peak was fitted with pseudo-Voigt function to determine position of the peaks and correlation lengths of domains. It was found that when TCN-BDT (6.6%) is added to a binary blend, the in-plane peak at 0.29 $Å^{-1}$ becomes wider, which results in lowered correlation length from 56.98 Å to 52.84 Å. At the same time, we observed an increase in out-

of-plane correlation length from 47.95 Å for binary device to 51.08 Å for ternary with 6.6% TCN-BDT.

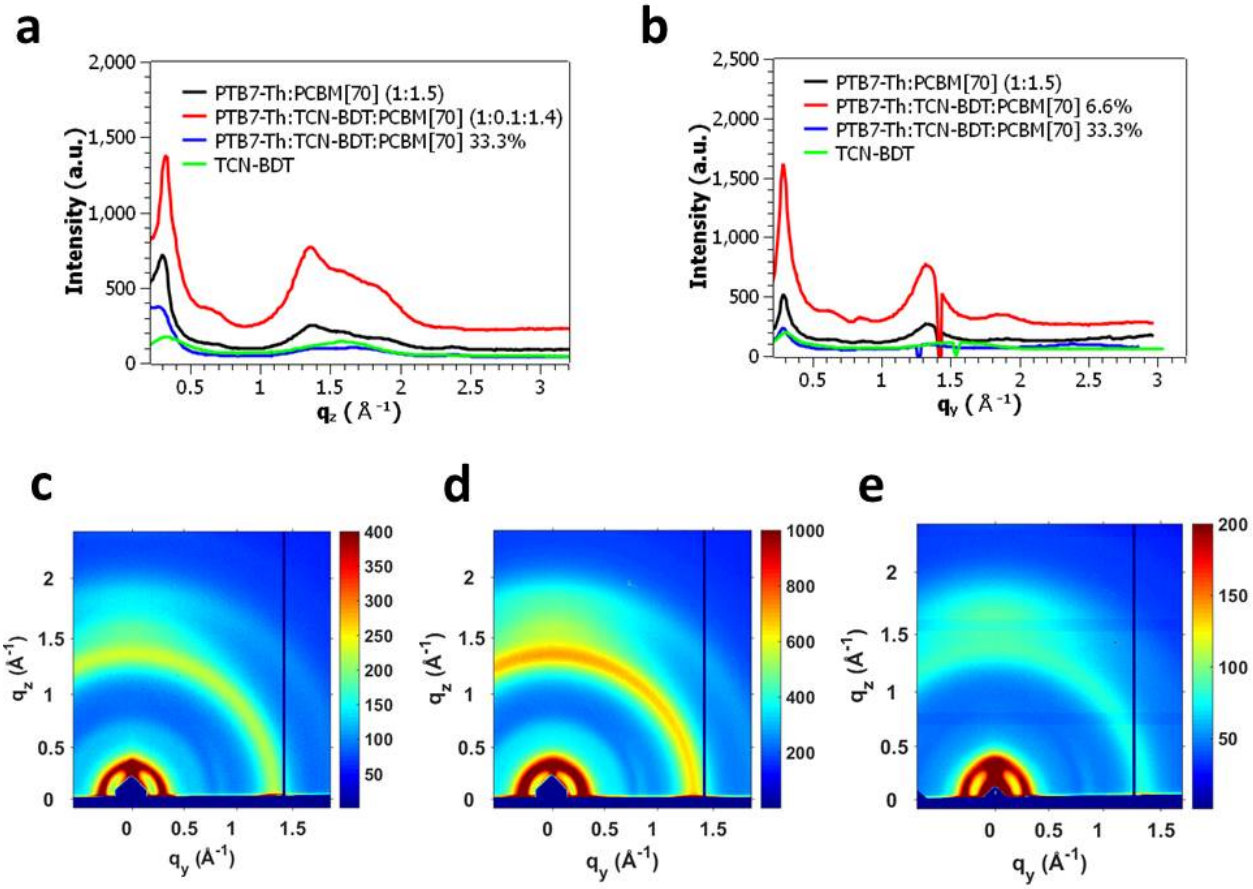

Figure 4.7. GIWAXS pattern linecuts in a)out-of-plane direction and b) in-plane direction; GIWAXS 2D pattern for c) binary blend, d)ternary blend with 6.6% TCN-BDT and e) ternary blend with 33.3% TCN-BDT.

This increase originates from a more crystalline structure that usually favors vertical charge transport. At the same time when the concentration of TCN-BDT was increased further (to 33.3%) scattering intensity of the peaks is significantly suppressed, which indicates that high

loads of a small molecule disrupt polymer and $PC_{71}BM$ phases which results in deteriorated performance for both OPV and OPD.

It is evident from our studies that a smaller concentration of TCN-BDT in the blend is important in order to improve the efficiency of devices. At the smaller concentrations the small molecule stays at the interface between PTB7-Th and PCBM, and starts penetrating into the main components' phases and disrupting them at the higher concentrations. When the charges (electrons) are injected from the top metal electrode to the LUMO of the donor in the dark, they will follow downward energy cascade percolating through PTB7-Th phase, then transfer to LUMO of a small molecule acceptor at the interface between PTB7-Th and $PC_{71}BM$. After the final electron transfer occurs into $PC_{71}BM$ phase, the charges will be collected at the ITO electrode, thus contributing to leakage current in dark. Since TCN-BDT has four acceptor contact points, surrounding conjugated core, the electron transfer from the polymer through the interface will most likely occur to one of the branches of the acceptor and will be passed further to $PC_{71}BM$ through another contact branch. According to DFT results for TCN-BDT presented in Chapter 2, LUMO of the molecule is mostly concentrated on the acceptor unit and HOMO is concentrated on the BDT core. Unlike, TPB which has four large and flat PDI units surrounding the core, TCN-BDT has four very compact and strong acceptor units. When electron is transferred to PDI unit, it may be easily delocalized over the large area of PDI and its transfer to another PDI unit or to PCBM is much easier. At the same time, when electron transfer happens to one of the accepting units in TCN-BDT, which is much smaller, compared to PDI, its further transfer to another accepting branch of the molecule or to PCBM may be hindered due to limited intermolecular contact. Interestingly, dark current in ternary devices with TPB did not change,

compared to binary devices, even though electron mobility increased. At the same time, we observed simultaneous decrease in electron mobility and in dark current in ternary devices with TCN-BDT. SCLC mobilities are measured in dark, thus mobility is adequately comparable with the dark current measurements. When concentration of the third component increases further, beyond optimum level, we observed significant morphological disruption in PTB7-Th and $PC_{71}BM$, as indicated by a significant decrease in intensities of scattering peaks, which indicates increased disorder in the films, consistent with deteriorated performance in both OPV and OPD. In addition, for higher loads the intermolecular interaction between third component molecules will establish charge transport channels of their own, that will result in increased dark current

.

4.3 Conclusions

New ternary bulk heterojunction blends were developed as a new approach to control dark current in organic photodetector devices. A series of experiments showed that with a proper concentration of the third component, the photodetector performance can be enhanced. It was found that the addition of a small amount of TCN-BDT (6.6%) in the acceptor phase results in an almost 20 fold decrease in dark current, thus improving the detectivity of fabricated photodetector devices. The increased photocurrent originated from additional light absorption by the third component, favorable morphology and resulted in the overall increase of device responsivity and quantum efficiency and avoided unfavorable trade-off between dark current and responsivity.

4.4 Experimental Section

Materials used.

Polymer PTB7-Th was obtained from 1 Material Company. Acceptor PCBM was obtained from American Dye Source. Small molecule acceptor TCN-BDT was synthesized by Dr. Qinghe Wu. Components for sol-gel ZnO precursor synthesis Zn(CH3COO)22H2O, 2-methoxyethanol and 2-aminoethanol were and solvents for active layer film formation chlorobenzene, 1,8-diiodooctane were purchased from Sigma Aldrich and were used as obtained without any additional purification. Sources for thermal deposition of electrodes, Molybdenum (VI) oxide was purchased from Sigma Aldrich and Ag slugs were purchased from Fisher Scientific.

Device fabrication:

Devices were assembled in an inverted configuration including layers of ITO/ZnO/active layer/MoOx/Ag sequentially deposited on top of each other. ITO glass was purchased from the company Thin Film Devices. To clean glass slides, they were sequentially ultrasonicated in chloroform, acetone and isopropyl alcohol, 15 minutes for each solvent. After ultrasonication the glasses were exposed to UV light /O_3 for 20 minutes, cooled down to room temperature and layer of ZnO was deposited on it. We used sol-gel method of ZnO formation described in the literature. Precursor solution was prepared 12 hours ahead of time and used immediately after that. Solution was filtered through syringe PTFE filter, 2-3 drops of it were placed onto the ITO surface and spin-coated at 4000 rpm/40 seconds in air. Films were immediately annealed in air at 2000C for 30 minutes (films placed on hot surface). After annealing films were slowly cooled

down to room temperature and transferred to glove box. Polymer and small molecule acceptors were dissolved in a mixture of solvents (chlorobenzene:DIO (97:3 vol %) overnight at 85^0C and spin-coated on ZnO surface at 70^0C. After film coating Molybdenum (VI) oxide (8 nm) and Ag (100 nm) were thermally evaporated on the active layer surface under vacuum < $2 \cdot 10^{-6}$ Torr.

Device characterization

Solar cell performance and dark current measurements: To test solar cell performance of the devices JV curves were obtained under illumination and in dark using source meter unit Keithley 2420. Devices for OPV were tested under 1 sun conditions (AM1.5G, 100 mW/cm2) using xenon lamp (Oriel 69920) intensity of which was calibrated with a standard NREL certified Si cell (Newport, 91150V). Masks with a well-defined area of 3.14 mm2 were used to define an active area of the device.

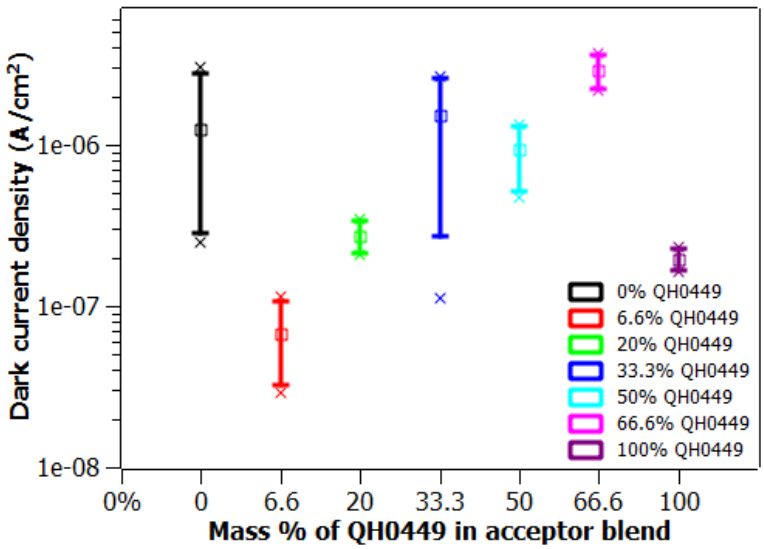

Figure 4.8. Dark current values for binary and ternary blends

EQE, detectivity and responsivity measurements: EQE was measured with a Newport QE measurement system (IQE-200) with a tungsten halogen lamp as a light source. Keithley SMU was used to bias devices for EQE under negative bias measurements. Responsivity and specific detectivity were calculated from EQE spectra.

Response time measurements: 5mW laser with a wavelength 650 nm was used as a light source and function generator BK Precision 3011B was used to modulate laser's signal at 25.3 kHz. Oscilloscope LeCroy 9354A was used to record a signal generated by a photodetector device. The signal was amplified with transimpedance amplifier.

Characterization of film's optical properties and morphology: UV/Vis spectra were obtained with Shimadzu UV-2401PC spectrophotometer. AFM studies were made with Asylum Cyfer microscope at the University of Chicago MRSEC MPML facilities. The GIWAXS measurements were performed at 8ID-E beamline of Advanced Photon Source, Argonne National Laboratory with a radiation wavelength 1.1364 Å. Samples for GIWAXS were prepared on polished Si wafer, covered with ZnO and coated with an active layer film being studied. Scherrer analysis of GIWAXS data was conducted where linecut peaks were fitted with pseudo-Voigt function to determine peak's position and full width at half maximum (FWHM).

Table 4.3 GIWAXS Scherrer peak analysis of GIWAXS scattering patterns for PTB7-Th, PCBM and TCN-BDT.

Content of TCN-BDT in acceptor [weight %]	q_y [Å^{-1}]	d_y [Å]	Δq_y [Å^{-1}]	D_L [Å]	q_z [Å^{-1}]	d_z [Å]	Δq_z [Å^{-1}]	D_L [Å]
0%	0.29	21.66	0.099	56.98	0.29	21.66	0.118	47.95
6.6%	0.29	21.66	0.107	52.84	0.32	19.64	0.111	51.08

Surface energy measurements:

Contact angle measurements were performed on pristine films of PTB7-Th, $PC_{71}BM$ and TCN-BDT using drop shape analyzer DSA-100 from Krüss GmbH at the University of Chicago MRSEC MPML. Experiments were conducted in air at room temperature for ultrapure 18MΩ water, diiodomethane and ethylene glycol. Software provided with the machine was used to analyze data and calculate surface energies for these materials using the OWRK (Owens, Wendt, Rabel and Kaelble) model. Neumann's equation was used to calculate interfacial surface energies for pairs of PTB7-Th/PCBM, PTB7-Th/TCN-BDT and TCN-BDT/PCBM.

$$\boldsymbol{\gamma_{AB} = \gamma_A + \gamma_B - 2\sqrt{\gamma_A \cdot \gamma_B} \cdot \exp(-\beta \cdot (\gamma_A - \gamma_B)^2}$$

Where γ_A and γ_B are surface energies of materials forming an interface under consideration, γ_{AB} is interfacial surface energy between materials A and B, β is equal to 0.000115 $m^4 mJ^{-2}$. Young's equation was used to calculate wetting coefficient of TCN-BDT in PTB7-Th/PCBM blend.

$$\boldsymbol{\omega_{TCN-BDT} = \frac{\gamma_{TCN-BDT/PTB7Th} - \gamma_{TCN-BDT/PCBM}}{\gamma_{PTB7Th/PCBM}}}$$

Table 4.4. Measured contact angles and calculated surface energies for PTB7-Th, $PC_{71}BM$ and TCN-BDT films.

Material	Contact angle [^{0}]			Surface energy [mN/m]
	Water	Diiodomethane	Ethylene glycol	
PTB7-Th	100.71	49.05	75.88	34.40
$PC_{71}BM$	98.02	22.55	67.49	46.71
TCN-BDT	99.57	40.07	67.89	39.57

Table 4.5. Calculated interfacial surface energies PTB7-Th, $PC_{71}BM$ and TPB films.

Interface	Interfacial surface energy [mN/m]
PTB7-Th/ $PC_{71}BM$	2.325
PTB7-Th/TCN-BDT	0.407
TCN-BDT/$PC_{71}BM$	0.799

4.5 References

(1) Jansen-van Vuuren, R. D.; Armin, A.; Pandey, A. K.; Burn, P. L.; Meredith, P. Organic Photodiodes: The Future of Full Color Detection and Image Sensing. Adv. Mater. 2016, 28, 4766–4802.

(2) Hussain, A. M.; Hussain, M. M. CMOS-Technology-Enabled Flexible and Stretchable Electronics for Internet of Everything Applications. Adv. Mater. 2016, 28, 4219–4249.

(3) Ostroverkhova, O. Organic Optoelectronic Materials: Mechanisms and Applications. Chem. Rev. 2016, 116, 13279–13412.

(4) García de Arquer, F. P.; Armin, A.; Meredith, P.; Sargent, E. H. Solution-Processed Semiconductors for next-Generation Photodetectors. Nat. Rev. Mater. 2017, 2, 16100.

(5) Konstantatos, G.; Sargent, E. H. Nanostructured Materials for Photon Detection. Nat. Nanotechnol. 2010, 5, 391–400.

(6) Richter, M.; Heumüller, T.; Matt, G. J.; Heiss, W.; Brabec, C. J. Carbon Photodetectors: The Versatility of Carbon Allotropes. Adv. Energy Mater. 2017, 7, 1601574.

(7) Yang, F.; Cheng, S.; Zhang, X.; Ren, X.; Li, R.; Dong, H.; Hu, W. 2D Organic Materials for Optoelectronic Applications. Adv. Mater. 2017, 1702415, 1–27.

(8) Xie, C.; Yan, F. Flexible Photodetectors Based on Novel Functional Materials. Small 2017, 13, 1701822.

(9) Tortiglione, C.; Antognazza, M. R.; Tino, A.; Bossio, C.; Marchesano, V.; Bauduin, A.; Zangoli, M.; Morata, S. V.; Lanzani, G. Semiconducting Polymers Are Light Nanotransducers in Eyeless Animals. Sci. Adv. 2017, 3, e1601699.

(10) Basiricò, L.; Ciavatti, A.; Cramer, T.; Cosseddu, P.; Bonfiglio, A.; Fraboni, B. Direct X-Ray Photoconversion in Flexible Organic Thin Film Devices Operated below 1 V. Nat. Commun. 2016, 7, 13063.

(11) Higgins, A.; Mohapatra, S. K.; Barlow, S.; Marder, S. R.; Kahn, A. Dopant Controlled Trap-Filling and Conductivity Enhancement in an Electron-Transport Polymer. Appl. Phys. Lett. 2015, 106, 1–5.

(12) Xue, J.; Forrest, S. R. Carrier Transport in Multilayer Organic Photodetectors: I. Effects of Layer Structure on Dark Current and Photoresponse. J. Appl. Phys. 2004, 95, 1859–1868.

(13) Carr, J. a.; Chaudhary, S. The Identification, Characterization and Mitigation of Defect States in Organic Photovoltaic Devices: A Review and Outlook. Energy Environ. Sci. 2013, 6, 3414.

(14) Fallahpour, A. H.; Kienitz, S.; Lugli, P. Origin of Dark Current and Detailed Description of Organic Photodiode Operation Under Different Illumination Intensities. IEEE Trans. Electron Devices 2017, 64, 2649–2654.

(15) Kaake, L. G.; Barbara, P. F.; Zhu, X. Y. Intrinsic Charge Trapping in Organic and Polymeric Semiconductors: A Physical Chemistry Perspective. J. Phys. Chem. Lett. 2010, 1, 628–635.

(16) Dongaonkar, S.; Servaites, J. D.; Ford, G. M.; Loser, S.; Moore, J.; Gelfand, R. M.; Mohseni, H.; Hillhouse, H. W.; Agrawal, R.; Ratner, M. a.; et al. Universality of Non-Ohmic Shunt Leakage in Thin-Film Solar Cells. J. Appl. Phys. 2010, 108, 124509.

(17) Siegmund, B.; Mischok, A.; Benduhn, J.; Zeika, O.; Ullbrich, S.; Nehm, F.; Böhm, M.; Spoltore, D.; Fröb, H.; Körner, C.; et al. Organic Narrowband near-Infrared Photodetectors Based on Intermolecular Charge-Transfer Absorption. Nat. Commun. 2017, 8, 15421.

(18) Pace, G.; Grimoldi, A.; Natali, D.; Sampietro, M.; Coughlin, J. E.; Bazan, G. C.; Caironi, M. All-Organic and Fully-Printed Semitransparent Photodetectors Based on Narrow Bandgap Conjugated Molecules. Adv. Mater. 2014, 26, 6773–6777.

(19) Qi, J.; Qiao, W.; Zhou, X.; Yang, D.; Zhang, J.; Ma, D.; Wang, Z. Y. High-Detectivity All-Polymer Photodetectors with Spectral Response from 300 to 1100 Nm. Macromol. Chem. Phys. 2016, 217, 1683–1689.

(20) Han, J.; Qi, J.; Zheng, X.; Wang, Y.; Hu, L.; Guo, C.; Wang, Y.; Li, Y.; Ma, D.; Qiao, W.; et al. Low-Bandgap Donor–acceptor Polymers for Photodetectors with Photoresponsivity from 300 Nm to 1600 Nm. J. Mater. Chem. C 2017, 5, 159–165.

(21) Kielar, M.; Dhez, O.; Pecastaings, G.; Curutchet, A.; Hirsch, L. Long-Term Stable Organic Photodetectors with Ultra Low Dark Currents for High Detectivity Applications. Sci. Rep. 2016, 6, 39201.

(22) Baeg, K. J.; Binda, M.; Natali, D.; Caironi, M.; Noh, Y. Y. Organic Light Detectors: Photodiodes and Phototransistors. Adv. Mater. 2013, 25, 4267–4295.

(23) Zhong, Y.; Sisto, T. J.; Zhang, B.; Miyata, K.; Zhu, X.-Y.; Steigerwald, M. L.; Ng, F.; Nuckolls, C. Helical Nanoribbons for Ultra-Narrowband Photodetectors. J. Am. Chem. Soc. 2017, 139, 5644–5647.

(24) Keivanidis, P. E.; Ho, P. K. H.; Friend, R. H.; Greenham, N. C. The Dependence of Device Dark Current on the Active-Layer Morphology of Solution-Processed Organic Photodetectors. Adv. Funct. Mater. 2010, 20, 3895–3903.

(25) Eom, S. H.; Nam, S. Y.; Do, H. J.; Lee, J.; Jeon, S.; Shin, T. J.; Jung, I. H.; Yoon, S. C.; Lee, C. Dark Current Reduction Strategies Using Edge-on Aligned Donor Polymers for High Detectivity and Responsivity Solution-Processed Organic Photodetectors. Polym. Chem. 2017, 8, 3612–3621.

(26) Zhang, L.; Yang, T. B.; Shen, L.; Fang, Y.; Dang, L.; Zhou, N.; Guo, X. G.; Hong, Z.; Yang, Y.; Wu, H.; et al. Toward Highly Sensitive Polymer Photodetectors by Molecular Engineering. Adv. Mater. 2015, 27, 6496–6503.

(27) Zhang, B.; Trinh, M. T.; Fowler, B.; Ball, M.; Xu, Q.; Ng, F.; Steigerwald, M. L.; Zhu, X.-Y.; Nuckolls, C.; Zhong, Y. Rigid, Conjugated Macrocycles for High Performance Organic Photodetectors. J. Am. Chem. Soc. 2016, 138, 16426–16431.

(28) Keivanidis, P. E.; Khong, S. H.; Ho, P. K. H.; Greenham, N. C.; Friend, R. H. All-Solution Based Device Engineering of Multilayer Polymeric Photodiodes: Minimizing Dark Current. Appl. Phys. Lett. 2009, 94, 173303.

(29) Yoon, S.; Jo, J. W.; Yu, S. H.; Yun, J. H.; Son, H. J.; Chung, D. S. Development of Novel Conjugated Polyelectrolytes as Water-Processable Interlayer Materials for High-Performance Organic Photodiodes. ACS Photonics 2017, 4, 703–709.

(30) Xiong, S.; Li, L.; Qin, F.; Mao, L.; Luo, B.; Jiang, Y.; Li, Z.; Huang, J.; Zhou, Y. A Universal Strategy to Reduce Noise Current for Sensitive Organic Photodetectors. ACS Appl. Mater. Interfaces 2017, 9, 9176–9183.

(31) Kim, S. H.; Heo, S.; Yun, D.-J.; Satoh, R.; Park, G.; Kim, K.-S. Dark Current Reduction of Small Molecule Organic Photodetectors by Controlling Gap States of Molybdenum Oxide Buffer Layers. Jpn. J. Appl. Phys. 2016, 55, 91601.

(32) Armin, A.; Hambsch, M.; Kim, I. K.; Burn, P. L.; Meredith, P.; Namdas, E. B. Thick Junction Broadband Organic Photodiodes. Laser Photonics Rev. 2014, 8, 924–932.

(33) Moulé, A. J.; Bonekamp, J. B.; Meerholz, K. The Effect of Active Layer Thickness and Composition on the Performance of Bulk-Heterojunction Solar Cells. J. Appl. Phys. 2006, 100, 94503.

(34) Lu, L.; Chen, W.; Xu, T.; Yu, L. High-Performance Ternary Blend Polymer Solar Cells Involving Both Energy Transfer and Hole Relay Processes. Nat. Commun. 2015, 6, 7327.

(35) Lu, L.; Xu, T.; Chen, W.; Landry, E. S.; Yu, L. Ternary Blend Polymer Solar Cells with Enhanced Power Conversion Efficiency. Nat. Photonics 2014, 8, 716–722.

(36) Xu, H.; Wada, T.; Ohkita, H.; Benten, H.; Ito, S. Molecular Design of Near-IR Dyes with Different Surface Energy for Selective Loading to the Heterojunction in Blend Films. Sci. Rep. 2015, 5, 9321.

CHAPTER 5

PHOTOLUMINESCENT POLYMERS CONTAINING SEMI-LADDER STRUCTURES FOR SOLUTION PROCESSED ORGANIC LIGHT-EMITTING FIELD-EFFECT TRANSISTORS

5.1 Introduction and Background

Organic conjugated polymers exhibit numerous electrical and optical properties, such as high electrical conductivity, semiconductivity, photoluminescence and optical nonlinearity.[1] In the past two decades, research efforts in the interconversion of light and electricity by using organic conjugated polymers have dominated the trends. The functionality involving the conversion of photons to electrons takes place in photovoltaic devices and photodetectors.[2–5] The reverse process, converting electrons to photons, occurs in organic light-emitting diodes (OLED). The OLED devices are nowadays widely used in lighting and display applications. The OPV solar cells show a promising perspective for commercialization as well.

Accompanied with the development of OLED, organic light-emitting field-effect transistors (OLEFET) emerged as a class of organic optoelectronic devices, which combine both the electrical switching capability of OFETs and the light-generating capability of OLEDs in a single device.[6–10] These transistors have a potential for digital displays and on-chip optical interconnection, and simplification of circuit design in electroluminescent displays.

Since the first demonstration of OLEFETs in 2003, several different structures of OLEFETs were investigated, including single layer, bilayer, and multilayer devices.[11] Different types of light-emitting materials were explored, such as normal LED materials, phosphorescent

LED materials as well as thermally activated delayed fluorescent (TADF) materials. However, there is only modest progress being made so far in this field.[12–14]

In an OLEFET device, electrons and holes are simultaneously injected from the opposite electrodes into an organic semiconductor layer under the proper gate-source and drain-source voltages. The excitons will be formed following the charge carrier injection, which undergoes radiative relaxation to the ground state, thus emitting light. Depending on the bias voltage between source and drain, the gate voltage can control the position of the light-emitting recombination zone and intensity.

There are several desired characteristics of semiconducting polymers for OLEFET application. The first one is the balanced electron and hole mobility. The OLEFETs are actually unique type of OFETs, with active layer prepared from luminescent organic semiconductor, or blends containing organic light-emitting materials. Therefore, high mobility is a critical factor due to the relatively long channel in the OLEFET devices. The second characteristic is high emission quantum yield, namely, the external quantum efficiency (EQE). It defines the electrical-to-light energy conversion capacity of devices, expressed as the percentage of charge carriers converted to photons. The third characteristic is the light-emitting spectrum, which indicates the color of the emitted light and is related to the energy gap of materials. The fourth is the image of the light-emission zone, which indicates the location of the recombination region, and the emission brightness. The light-emitting region should be controlled so that the exciton/charge interaction and exciton/metal electrode interaction can be minimized, both of which enhance non-radiative exciton decay. It is therefore preferred that devices are capable of ambipolar hole/electron injection from their respective source-drain electrodes.[15,16] Since OLET

devices typically consist of multiple layers (interfacial layers, organic dielectrics, emissive layers), the polymers used must be soluble in orthogonal solvents to each other. This requirement significantly limits the choice of available materials. Therefore, new emissive polymers that meet these criteria may significantly boost the progress in the field. While side-chain engineering may control the polymer solubility and processability, it is much more challenging to balance optical and electrical properties in a single material.[17–20] On the one hand, dense crystalline structures with tightly packed conjugated molecules have the highest electronic coupling and thus the best charge transport. At the same time, tight π-π stacking of conjugated molecules is detrimental to their photoluminescence properties and may facilitate a cascade of quenching processes, including exciplex (excimer) formation, energy and electron transfer processes, resulting in increased non-radiative decay. Even though a class of molecules with aggregation-induced fluorescence is known, where fluorescence increases with increasing concentration, these molecules are scarce and typically have structures with significant steric hindrance of aromatic moieties, which may inhibit charge transport. The contradicting requirements for high charge mobility and high fluorescence make it very challenging to balance these properties in a single material.

Despite many attempts to resolve the mobility-fluorescence trade-off, there are still challenges in developing OLET materials that have comparable efficiency with the best performing OLED. In this chapter, I describe introduction of ladder-type monomers as a strategy to overcome the trade-off.[21–23] There are two main advantages associated with the conjugated ladder systems. Firstly, ring fusion introduces rigidity into the entire system, greatly decreasing the effective vibrational modes available for non-radiative decay and improving light emission.

Secondly, the ring fusion extends effective conjugation length, leading to more controllable bandgaps, better delocalization of frontier molecular orbitals and eventually better intramolecular charge transport. Because of improved intramolecular transport, there is less π-π stacking required for efficient charge transfer between polymer chains.

Previously, our group has developed a series of polymer electron acceptors that contain TPTQ (5,11-bis(2-butyloctyl)-dihydrothieno[2′,3′:4,5]-pyrido[2,3-g]thieno[3,2-c]quinoline-4,10-dione) and TPTI (4,10- bis(2-butyloctyl)thieno[2′,3′:5,6]pyrido[3,4-g]thieno[3,2-c]-isoquinoline-5,11-dione) fragments.[24–26] Even though these polymers were designed for solar cell applications, most of them showed ambipolar behavior in FET. Since ambipolar charge injection is one of the prerequisites for efficient OLEFET devices, we further synthesized fluorescent polymers containing these ladder-type structures. We investigated the physical, optical and electronic properties and morphologies of these polymers. Their performances as emissive materials in OLEFET devices were explored.

5.2 Results and Discussion

5.2.1 Synthesis and Characterization

The polymers were synthesized via Suzuki polymerization of TPTQ/TPTI bromide with carbazole/fluorene monomers containing bis(pinacolato)diboron (BPin) moieties. Structures and general synthetic approaches of the polymers are summarized in Scheme 5.1. Carbazole was chosen as a co-monomer because of its superior fluorescent properties and the possibility of side-chain engineering in positions N9 of the ring. It may be expected that the HOMO energy level of the resulting polymers will be closer to the HOMO of a more electron-

rich unit (carbazole) and the LUMO of the polymer will be closer to that of more electron-withdrawing (TPTI/TPTQ). Sizable molecular weights and generally narrow polydispersity indices PDI were observed for polymers as summarized in Table 5.1. Both polymers were soluble in common organic solvents such as p-xylene or chloroform.

Scheme 5.1. A general synthesis scheme of the polymers TPTQ-C and TPTI-C (R1 – 2-butyloctyl, R – 2-ethylhexyl).

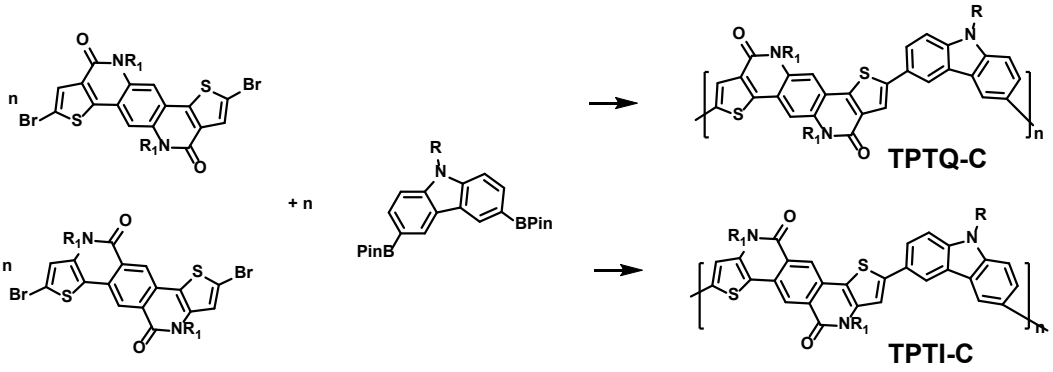

Table 5.1. Physical properties of the polymers measured with gel-permeation chromatography.

Parameters	TPTQ-C	TPTI-C
M_w	91767	17797
M_n	32823	14070
PDI	2.8	1.26

5.2.2 Electrochemical Properties

The HOMO and LUMO energy levels were determined by using the cyclic voltammetry (CV) technique, with ferrocene as a standard. The electrochemical parameters are summarized in Table 5.2. The polymer containing TPTQ fragment has deeper HOMO and LUMO energy levels than its TPTI analog. The same trend is observed both in experimentally measured energy levels and the ones calculated from DFT. It is understandable that TPTQ

monomer has amide carbonyl group attached to the thiophene moiety, which reduced the electron density in thiophenyl moiety. TPTI monomers has the electron rich nitrogen attached to thiophenyl (Th) moiety, which further enhances the electron density in Th ring.

Table 5.2. HOMO and LUMO energies of the polymers measured with CV and calculated from DFT

Polymer	HOMO (eV)	LUMO (eV)	Bandgap (eV)
TPTQ-C	-5.44[a]/-5.03[b]	-2.81[a]/-2.16[b]	2.25[c]/2.63[a]/2.87[b]
TPTI-C	-5.29[a]/-4.77[b]	-2.65[a]/-1.78[b]	2.14[c]/2.64[a]/2.99[b]

[a] Measured from cyclic voltammetry
[b] Calculated from DFT
[c] Calculated from the onset of the solution absorption spectrum in chloroform

5.2.3 Optical Properties

The optical absorption and emission properties of these materials were investigated in solution and in film. The photophysical parameters of the polymers deduced from absorption (Figure 5.1a) and photoluminescence (Figure 5.1b) spectra in solution and in the form of thin films are summarized in Table 5.3.

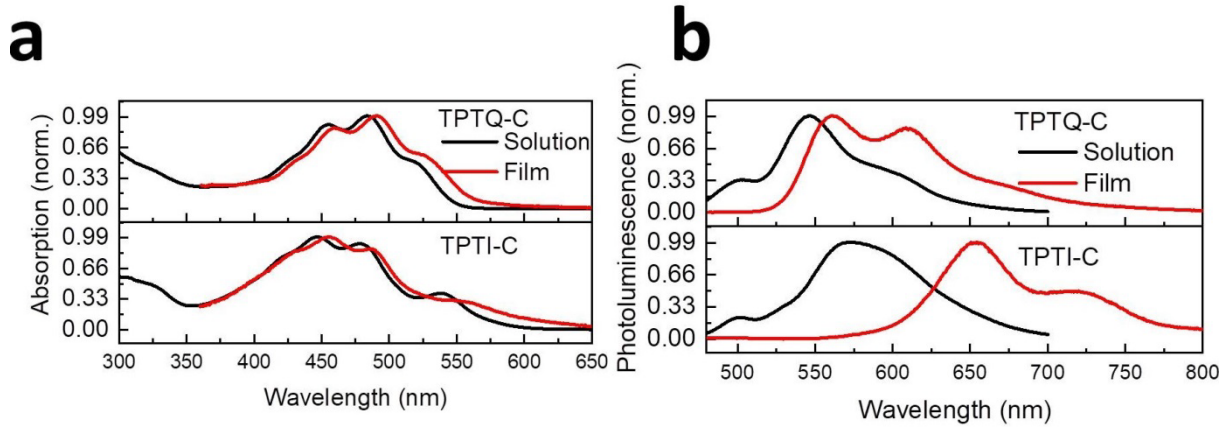

Figure 5.1. Spectra of a) absorption and b) photoluminescence of the polymers in chloroform solution and in thin films.

TPTQ-C has three well-resolved peaks in its solution absorption spectrum. The peak at 270 nm can be attributed to the combined absorption of individual monomers. N-alkylated carbazole has an absorption peak at around 290 nm and TPTQ monomer has a peak at 260 nm. The peaks at 453 nm, 484 nm and a shoulder at 520 nm originate from (0-2), (0-1) and (0-0) electronic transitions, respectively.

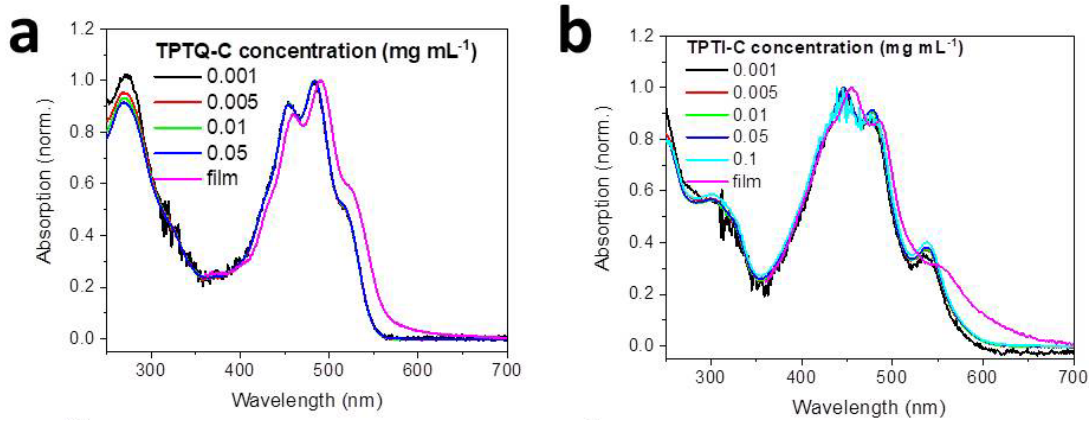

Figure 5.2. Concentration dependent UV-Vis absorption spectra of TPTQ-C and TPTI-C chloroform solutions

With the increasing concentration of the polymer solution, the general shape of the absorption spectrum does not change (Figure 5.2a). A slight red shift in the position of visible region peaks is observed in absorption spectra of the films. The peak attributed to monomer absorption does not exhibit such a shift. Similarly to TPTQ-C, the polymer TPTI-C exhibits blue absorption peak at around 300 nm originating from the overlapping absorption of carbazole and TPTI individual units. In the visible region TPTI-C has three peaks – a better resolved 0-0 peak at 540 nm, 0-1 peak at 478 nm and 0-2 peak at 447 nm. In more concentrated solutions and in films, the general shape of the spectrum stays almost unchanged, except 0-0 peak which becomes broader and less resolved (Figure 5.2b).

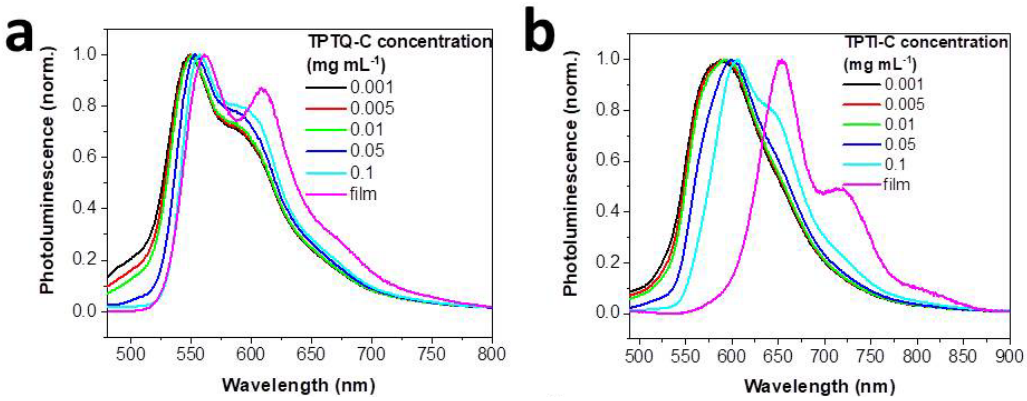

Figure 5.3. Concentration-dependent photoluminescence spectra of TPTQ-C and TPTI-C, chloroform solutions.

TPTQ-C is more fluorescent, showing PLQY 30%, while TPTI-C shows lower PLQY of 21%. The fluorescence spectra of TPTQ-C in dilute solutions show vibronic structure with 0-0 transition at 548 nm and a shoulder at 604 and 660 nm, due to 0-1 and 0-2 transitions. The shoulder peak is present even in the most dilute solution and its intensity increases with the increasing concentration. This result seems to indicate that the polymers are naturally folded and chromophores show weak aggregation. Upon concentration increase, the PL spectrum exhibits a slight red shift and a growth of 0-1 peak, which becomes fully resolved in the film (Figure 5.3a). TPTI-C shows broad, almost featureless emission, centered at around 575 nm and a barely visible shoulder in the most dilute solution. The emission spectrum like this is usually present in disordered systems. The general shape of the spectrum is almost unchanged until concentration 0.1 mg mL^{-1}. The red-shifted shoulder-peak appears in the film fluorescence, however it is less pronounced than in the case of TPTQ-C.

Table 5.3. Photophysical parameters of polymer solutions and films

Polymer	Solution			Film		
	$\lambda_{absorption}$ (nm)	λ_{PL} (nm)	PLQY (%)	PL lifetime τ (ns)	$\lambda_{absorption}$ (nm)	λ_{PL} (nm)
TPTQ-C	453/484	548/604	30	2.00	460/490	560/610
TPTI-C	447/478	570	21	0.43/1.33	456/487	652/720

It should be noted that the polymer containing TPTI moiety shows a dramatic solution to film fluorescence red-shift than its TPTQ analog. In addition, the peak has a more resolved vibronic structure in the film. This may be indicating strong aggregation of TPTI-C and in general its more ordered conformational structure in the film compared to solution.

To gain more insight into the photophysical properties, time-resolved fluorescence decay was measured for polymer solutions (Figure 5.4a).

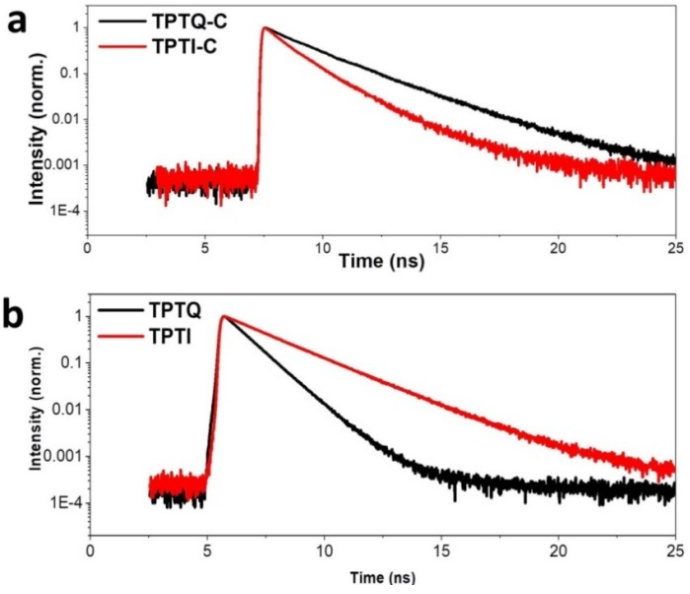

Figure 5.4. Time resolved fluorescence decay characteristics of a)TPTQ-C and TPTI-C polymer solutions excited at 450 nm, b) TPTQ and TPTI monomer chloroform solutions excited at 406 nm.

Table 5.4. Concentration-dependent fluorescence lifetimes of TPTQ-C, TPTI-C, TPTQ and TPTI chloroform solutions.

Conc. (mg mL^{-1})		TPTQ-C		TPTI-C		TPTQ		TPTI	
		Time (ns)	Fraction	Time (ns)	Fraction	Time (ns)	Fraction	Time (ns)	Fraction
0.001	τ_1	2.00	n/a	1.33	83%	0.93	n/a	2.04	n/a
	τ_2	-	n/a	0.43	17%	-	n/a	-	n/a
0.005	τ_1	2.12	n/a	1.32	85.3%	0.94	n/a	2.06	n/a
	τ_2	-	n/a	0.39	14.7%	-	n/a	-	n/a
0.01	τ_1	2.14	n/a	1.33	86.1%	0.95	n/a	2.04	n/a
	τ_2	-	n/a	0.38	13.9%	-	n/a	-	n/a
0.05	τ_1	2.10	n/a	1.32	88.3%	0.99	n/a	2.05	n/a
	τ_2	-	n/a	0.34	11.7%	-	n/a	-	n/a
0.1	τ_1	2.29	n/a	1.35	89.8%	1.05	n/a	2.05	n/a
	τ_2	-	n/a	0.32	10.2%	-	n/a	-	n/a

Fluorescence decay curves were fitted with exponential decay equation and fluorescence lifetimes were calculated. It was found that polymer TPTQ-C exhibits single exponential decay behavior with the longest fluorescence lifetime of 2 ns. TPTI-C showed double exponential decay behavior with shorter lifetimes, which may indicate the presence of different emissive species. We also measured the same parameters for monomers TPTQ and TPTI. As shown in Figure 5.4b and summarized in Table 5.4, both TPTQ and TPTI exhibit monoexponential fluorescence decay. TPTQ has twice as short lifetime of 0.93 ns and higher PLQY of 23%. At the same time TPTI has a lifetime constant 2.04 ns and smaller PLQY 9%. Relation of PLQY and the radiative decay rate is described with the equation $PLQY=\tau \times k_r$, where k_r is rate of radiative decay, τ excited state lifetime. Higher PLQY for TPTQ means that TPTQ has higher radiative decay rate. This is consistent with Strickler-Berg relation, which indicates that species

with lower molar absorption coefficient usually have longer radiative lifetimes and lower radiative decay rate. As shown in Figure 5.5 TPTQ has higher molar absorption coefficient. It is interesting to notice that TPTQ polymer have longer lifetime for the excited state than TPTQ monomer, while for TPTI is just the opposite.

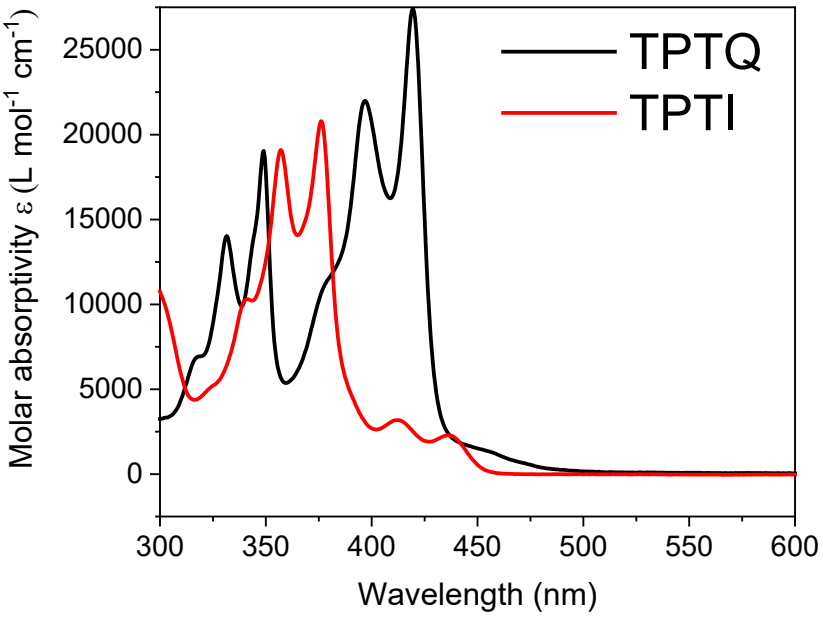

Figure 5.5. Molar absorptivity spectra of 0.01 mg mL^{-1} solutions of TPTQ and TPTI in chloroform

5.2.4 Light-Emitting Properties of OLEFET Devices

We prepared organic light-emitting field-effect transistor devices (OLEFET) with these polymers as emissive layers and investigated their current-voltage characteristics (Figure 5.6a). We used the bottom gate-top contact (BG-TC) configuration of the device with p-doped silicon as a gate and thermally evaporated layer of gold as source-drain electrodes. The channel length (L) of the devices is 50 µm and channel width (W) of 18.2 mm. Silicon nitride (Si_3N_4)

was used as a dielectric layer because of its higher dielectric constant and it was modified with a layer of PMMA or OTS.

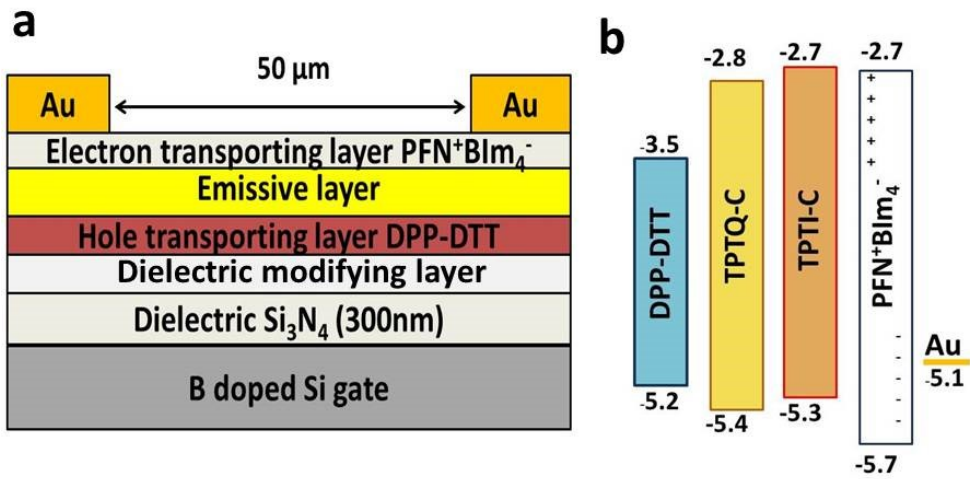

Figure 5.6. a) Device architecture of organic light-emitting field-effect transistors (OLEFET); b) Energy diagram of light-emitting polymers, interfacial layers and source-drain metal contacts.

Polymers DPP-DTT and $PFN^{+}BIm_4^{-}$ were used as hole-transporting and electron-transporting layers, respectively, which do not contribute to light emission and only facilitate charge transport (Figure 5.6b). Polymer emissive layer was coated from the solvents orthogonal to those that dissolve DPP-DTT and annealed at 100°C. Source-drain current-voltage characteristics were measured at positive and negative gate voltages to test electron and hole transport in the device (Figure 5.7). The output curves show that the devices exhibit ambipolar behavior demonstrating both hole and electron transport. However, the transport is not balanced, resulting in source-drain currents at negative gate voltages (hole transport) being noticeably larger than the currents at positive gate voltages (electron transport). The device transfer curves also support the conclusion about ambipolar behavior, showing typical v-shape curves attributed to hole and electron transport. The curves in the saturation mode were used to calculate hole and

electron mobilities, which are summarized in Table 5.5. It is evident from the mobility data that the charge transport happens predominantly at the DPP-DTT/dielectric interface, since mobilities observed for multilayer devices are several orders of magnitude larger than for single layer devices with the emissive layer (Table 5.6). The results are consistent with the misbalanced output curves showed above. These FET devices contain symmetric source and drain electrodes (i.e. electrodes made of the same metal – gold). The injection barrier for holes is much lower than the barrier for electrons. The work function of metal gold (-5.1 eV) is better aligned with HOMO energy levels of the polymers (-5.2 to -5.7 eV) where hole injection happens, rather than with LUMO levels (-2.7 to -2.8 eV), participating in electron injection. The misbalance in the hole and electron mobilities results in light emission being predominately concentrated near the minority charge carrier injecting electrode, rather than in the middle of the channel, which we observe in our devices. Polymer TPTQ-C, which has higher hole mobility in this series also shows the brightest yellow emission. TPTI-C shows weak orange emission from the region near the electrode for higher gate voltages.

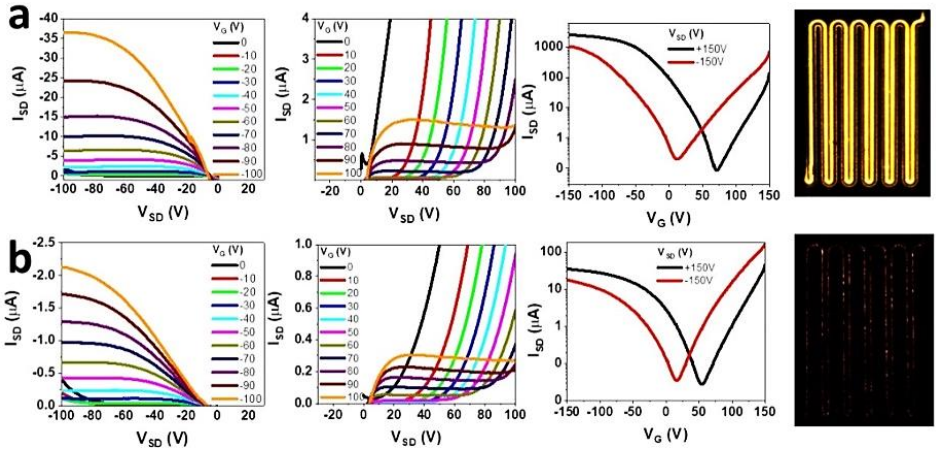

Figure 5.7. Transfer curves and microscope photographs of light-emitting transistors with the emissive layers made of a)TPTQ-C; b)TPTI-C.

Table 5.5. Hole and electron mobilities in OLEFET devices

Device	Hole mobility, $cm^2V^{-1}s^{-1}$	Electron mobility, $cm^2V^{-1}s^{-1}$
OLEFET with TPTQ-C	$(8.15\pm1.81) \times 10^{-2}$	$(2.03\pm0.65)\times10^{-3}$
OLEFET with TPTI-C	$(2.75\pm1.40) \times 10^{-2}$	$(4.53\pm3.95)\times10^{-3}$

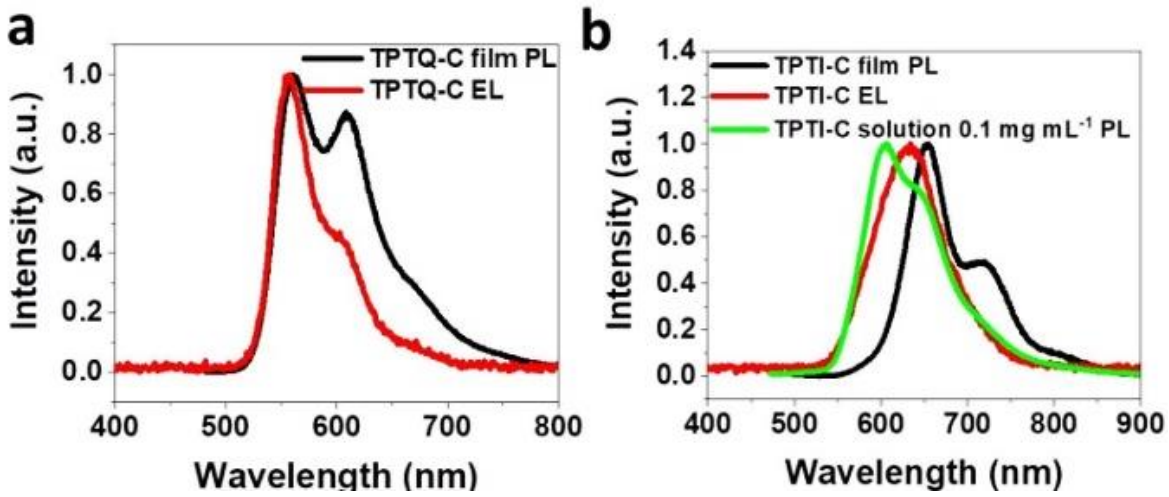

Figure 5.8. a) Film photoluminescence and electroluminescence in TPTQ-C, b) Film photoluminescence and electroluminescence in TPTI-C.

The graphs in Figure 5.8 show that TPTQ-C has electroluminescence spectrum very close to 0-0 transition band in the film photoluminescence spectrum. At the same time, the electroluminescence spectrum appears slightly blue-shifted for TPTI-C. The solution fluorescence spectrum presented in Figure 5.8b for comparison shows that the electroluminescence spectrum of TPTI-C resembles the fluorescence spectrum of solution with the polymer concentration of 0.1 mg mL^{-1}. This indicates that electroluminescence in TPTI-containing polymers happens predominantly from individual polymer molecules, rather than from aggregated clusters.

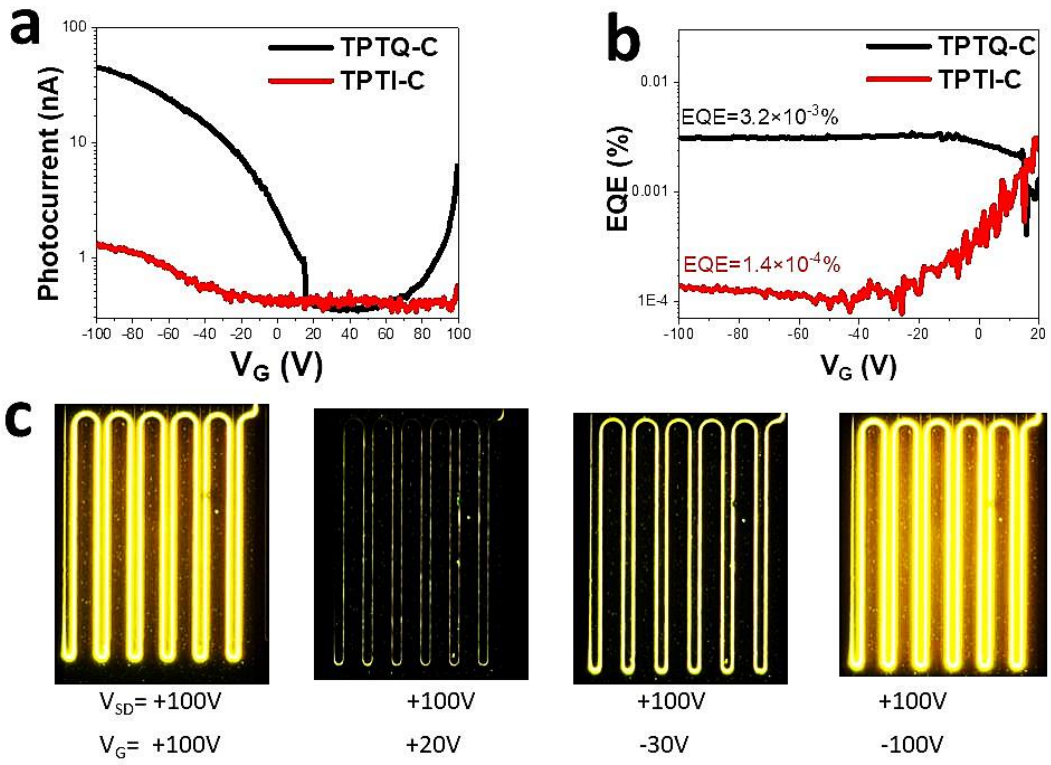

Figure 5.9. a) Photodetector photocurrent as a function of gate voltage for OLEFET devices with TPTQ-C and TPTI-C; b) EQE as a function of gate voltage for OLEFET devices with TPTQ-C and TPTI-C; c) microscope photographs of light-emitting device at different gate voltages and source-drain voltage +100V.

We studied light emission from the OLEFET devices in detail. The transfer characteristics of the OLEFET and the photocurrent of the reverse-biased photodiode were simultaneously measured, by placing calibrated photodiode right in front of the device and observing the response (Figure 5.9a). For both polymers, the brightest light emission was observed for negative gate voltages, where hole transport dominates. The light signal from TPTQ-C was much stronger than for TPTI-C. We observed three distinct light-emitting modes as a function of the gate voltage. At the positive gate voltages (dominating electron transport),

light emission is observed due to recombination of major charge carrier electrons and minor charge carrier holes near electrodes. Decreasing gate voltage results in decreased amounts of injected charge carriers which, in turn, diminishes light emission. When gate voltage reaches more negative values, hole transport becomes dominating and electrons become minority charge carriers. The threshold turn-on gate voltage required for light emission was around +20V for TPTQ-C and -20 V for TPTI-C. Light emission in TPTQ-C devices is observed over a much wider range of gate voltages.

We measured the external quantum (EQE) efficiency of OLEFET devices in the brightest emission mode (gate voltage from +20V to -100 V). The results are summarized in Figure 5.9b. Devices with TPTQ-C show EQE at the brightest point 3.2×10^{-3}%, while TPTI-C shows much smaller EQE of 1.4×10^{-4}%. EQE in the hole accumulation mode that we observed in TPTQ-C is 3 times higher than the hole accumulation EQE of similarly structured OLET devices with Super Yellow, a very-well studied polymer with similar electroluminescence spectrum.[9] Moreover, we do not observe EQE roll-off at the brightest point and higher currents –EQE in TPTQ-C device stays almost constant over the range of gate voltages 75V, which is a highly desired property in light-emitting devices. Photographs in Figure 5.9c demonstrate light emission from TPTQ-C device at different gate voltages and constant source-drain voltage. It is evident that gate voltage does not affect the position of light-emitting zone and only changes emission intensity.

5.2.4 Morphology Studies

In order to study bulk polymer packing in the film, we measured GIWAXS for polymer films. The samples were prepared on PEDOT:PSS coated silicon substrates and

measured in vacuum. We studied the morphology of TPTQ and TPTI monomers, which are drastically different (Figures 5.10 and 5.12).

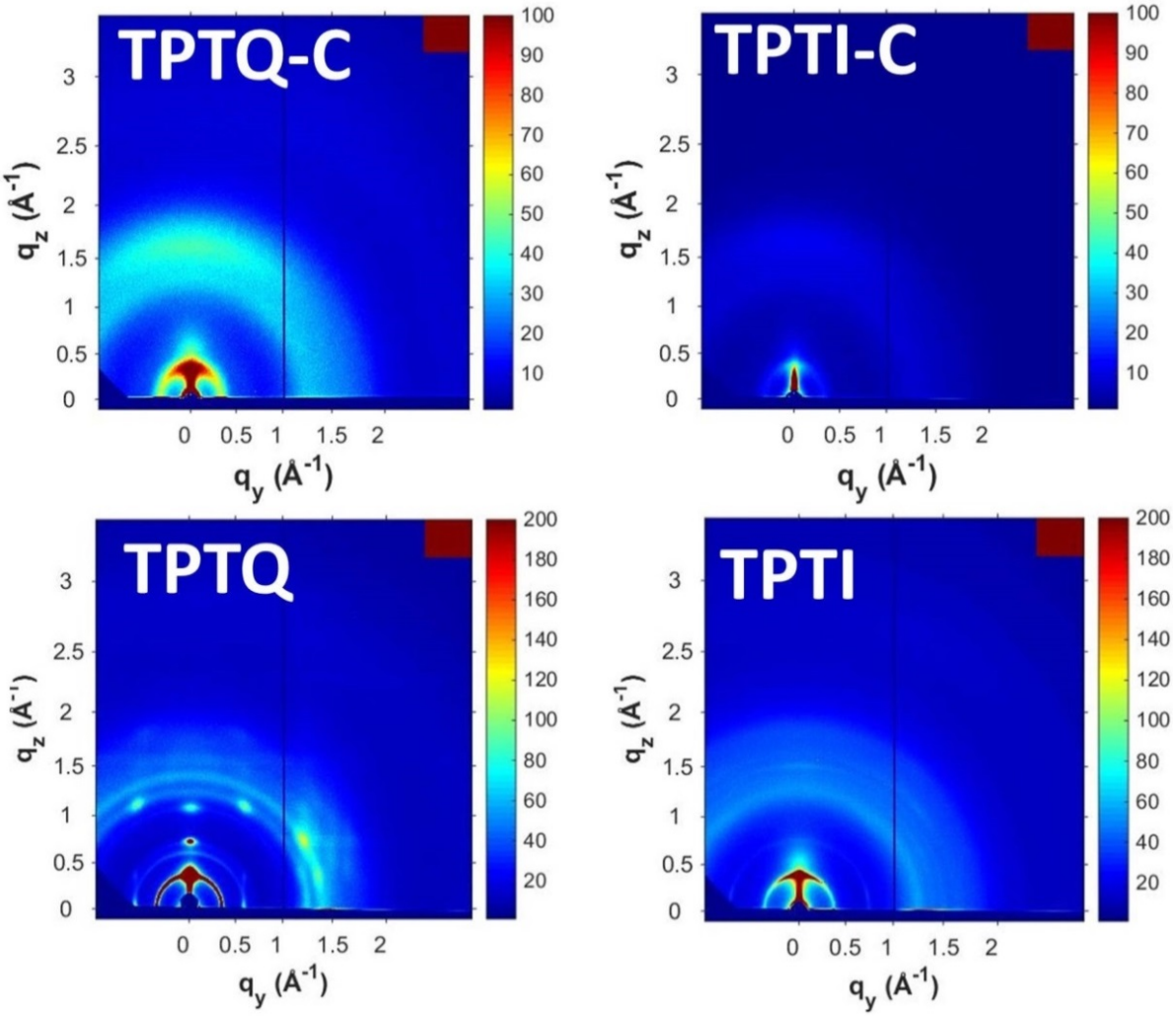

Figure 5.10. 2D GIWAXS scattering patterns of polymer and monomer films

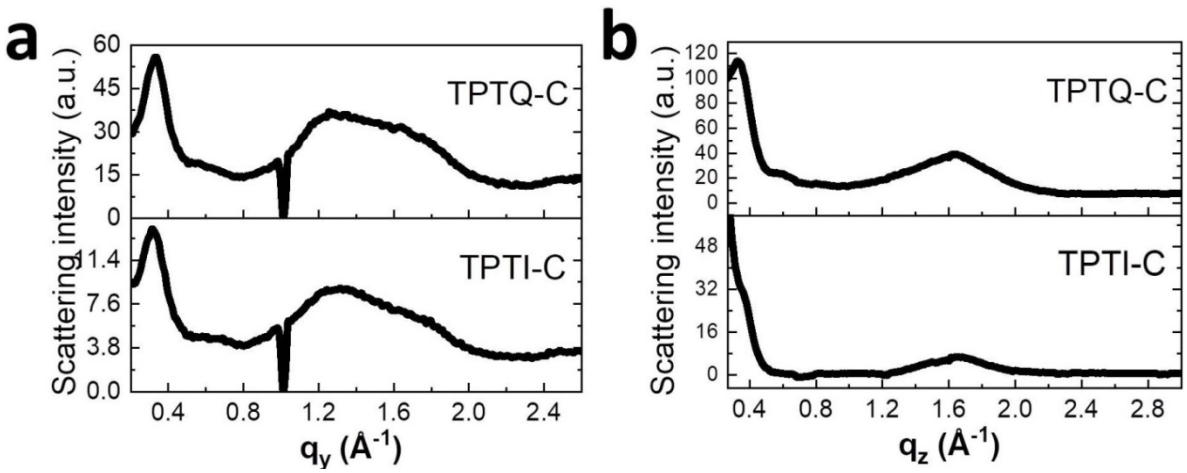

Figure 5.11. Polymer films GIWAXS linecuts in a) in-plane, b) out-of-plane directions.

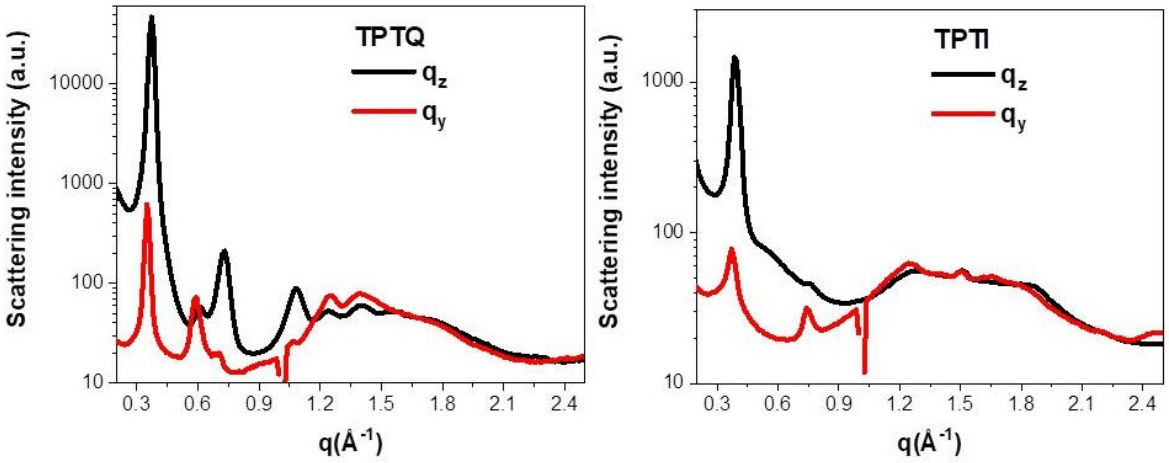

Figure 5.12. GIWAXS linecuts of TPTQ and TPTI monomer films

TPTQ shows quite crystalline structure with very well resolved peaks that indicate edge-on orientation. TPTI is slightly more amorphous and shows more face-on character. The 2D scattering profile and linecuts in out-of-plane and in-plane directions for polymers are

summarized in Figures 5.10 and 5.11. The polymers exhibit lamellar and π-π stacking peaks both in out-of-plane and in-plane directions. GIWAXS data show the polymers form quite an amorphous film with just a slight preferential face-on orientation. A lamellar peak at around 0.3-0.35 $Å^{-1}$ (inter-lamellar distance 18.5-21 Å) is present in both in-plane and out-of-plane directions, showing no preferential orientation. A π-π stacking peak at 1.6-1.7 $Å^{-1}$ (stacking distance 3.7-3.9 Å) is better revealed in out-of-plane directions which indicates a slight preference to face-on π-π stacking. At the same time, this peak is very broad, which indicates a lack of crystalline features and generally amorphous structure. Improving crystallinity of the polymer may be one of the approaches to increase charge carrier mobility in the devices.

5.2.5 Mechanism Discussion

Experimental results discussed above indicate that TPTQ-containing polymer TPTQ-C shows much superior PL and EL properties than its TPTI-containing analog TPTI-C. Both polymers have close energy levels and have the same device structure. This results in close charge injection barriers and does not explain the difference in performance. However, optical properties and morphology are drastically different for these two polymers. Optimized polymer geometries obtained from DFT calculations show that TPTQ-C exhibit coiled-like structure while TPTI-C is more elongated zigzag-like geometry (Figure 5.13). The position of alkyl chains in TPTI-containing polymers facilitates its more elongated geometry and aggregation. Outward-facing butyloctyl chains present in TPTI create steric hindrance with the alkyl chains on carbazole units thus preventing it from forming efficient coil structure. At the same time they make the center of the conjugated TPTI unit more open and accessible for stacking with the neighboring units. Alkyl chains in TPTQ polymers face inward, which partially covers the

conjugated unit and does not let it aggregate as efficiently. At the same time they allow more conformational flexibility in TPTQ and carbazole units which results in more efficient coiling.

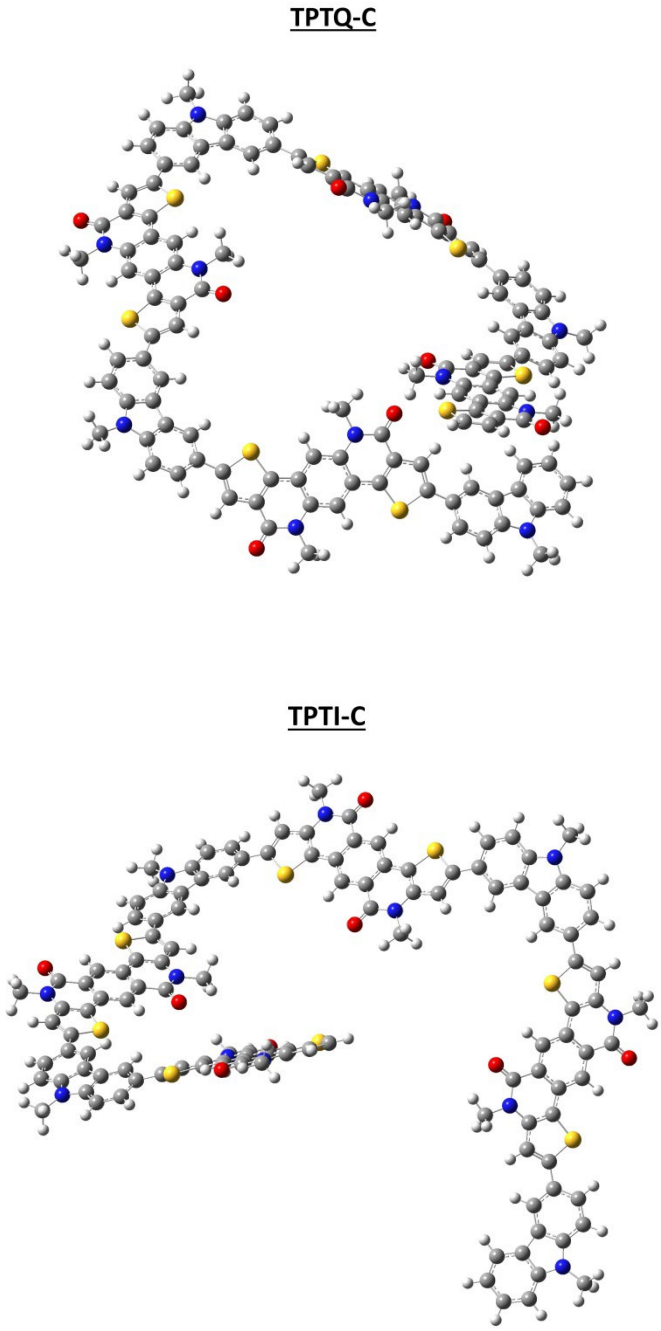

Figure 5.13. DFT optimized geometries for TPTQ-C and TPTI-C.

The comparison of TPTQ monomer film PL spectra and polymer film PL/EL indicate that emission in the polymer system happens predominantly from the TPTQ-C 0-0 emission band which appears in weakly aggregated structures. Photoluminescence excitation (PLE) spectra measured for both polymers (Figure 5.14) show a close resemblance to the corresponding UV-Vis absorption spectra.

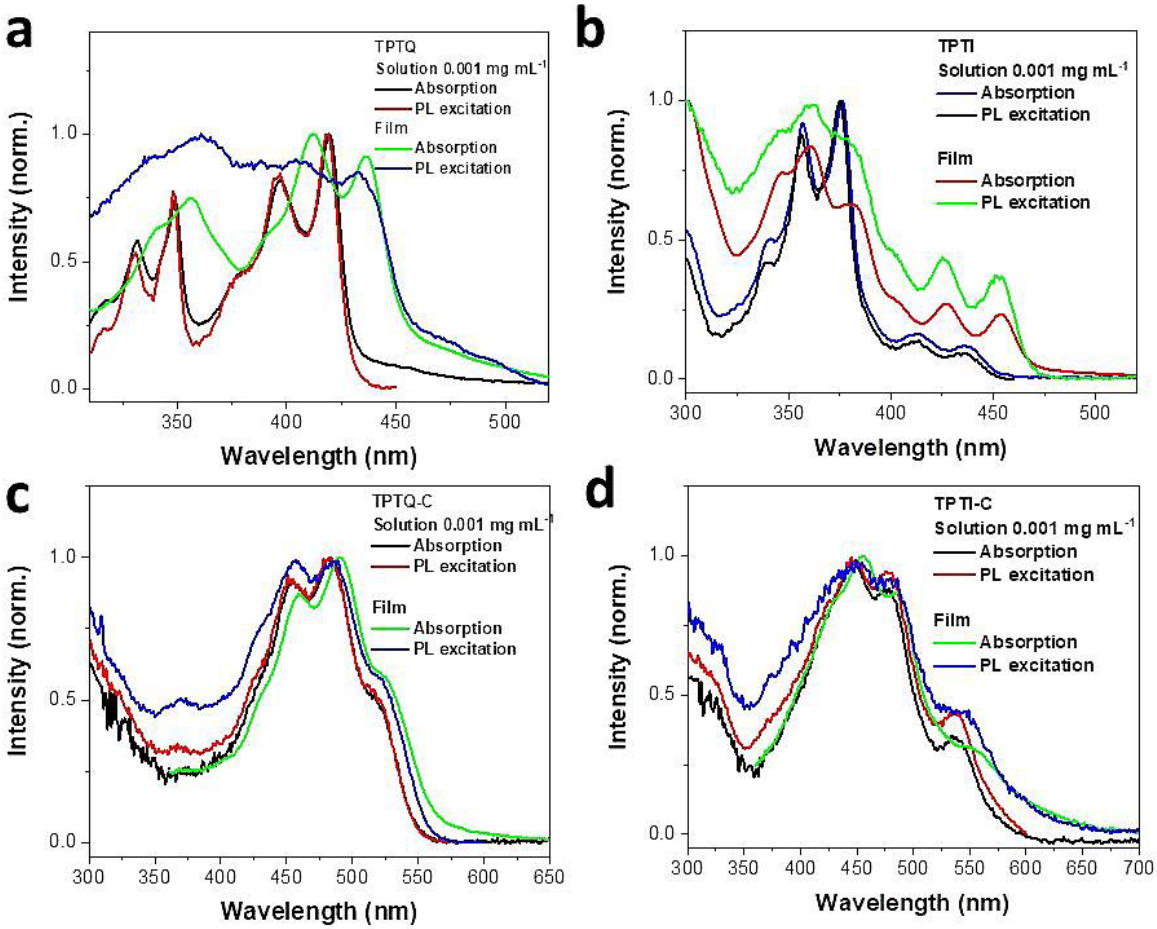

Figure 5.14. Comparison of absorption spectra and photoluminescence excitation spectra in films and solutions of a) TPTQ, b) TPTI, c) TPTQ-C, d) TPTI-C.

At the same time, the emitting chromophore in TPTI-C experiences significant quenching due to aggregation in the film and weak electroluminescent emission is only observed from monomeric, less aggregated TPTI-C units.

5.3 Conclusions

As a result of our studies, we have developed two new fluorescent polymers and studied them for OLEFET applications. An important structural feature of these polymers is the presence of semi-ladder monomer units TPTQ and TPTI which were introduced in order to achieve good fluorescence and charge transport properties. TPTQ and TPTI are isomers and have very similar structures. Despite the structural similarity, their properties and the properties of the polymers containing them are drastically different. TPTQ containing polymer TPTQ-C shows good light-emitting properties. When used as the emissive layer in OLEFET devices it shows bright yellow emission, the intensity of which depends on gate voltage. EQE of the OLEFET devices with TPTQ-C is 3.2×10^{-3}% in hole accumulation mode and it is stable over a wide range of gate voltages. Observed EQE in hole-accumulation mode is higher than in similarly structured devices containing Super Yellow. At the same time, TPTI-C shows much inferior properties. When used as an emissive layer in OLEFET devices it shows very weak orange emission and its EQE is only 10^{-4}%. Molecular structure of the TPTQ and TPTI monomer units, and more specifically position of alkyl chains affects folding modes in the polymers and their optoelectronic properties. TPTQ-C shows coiled structure, however its TPTQ monomer units are somewhat isolated with the alkyl chains which prevent their efficient

aggregation. At the same time, TPTI-C forms more elongated curved structure and TPTI units are more sterically available for aggregation with the other units.

5.4 Experimental section

Materials used

Polymers TPTQ-C, TPTI-C, their monomers and precursors have been synthesized by Mr. Mohammad A. Awais in Prof. Luping Yu lab. Polymers DPP-DTT and PFN-Br have been purchased from 1 Material, Inc. Bromide counter ion has been replaced with BIm_4^- in PFN-Br using methods described elsewhere.[27] All the solvents used in this study, including p-xylene, methanol, and chloroform were anhydrous and used as received from Sigma Aldrich without additional purification.

Materials properties studies

UV-Vis absorption spectra were measured using Shimadzu UV-3600 spectrometer.

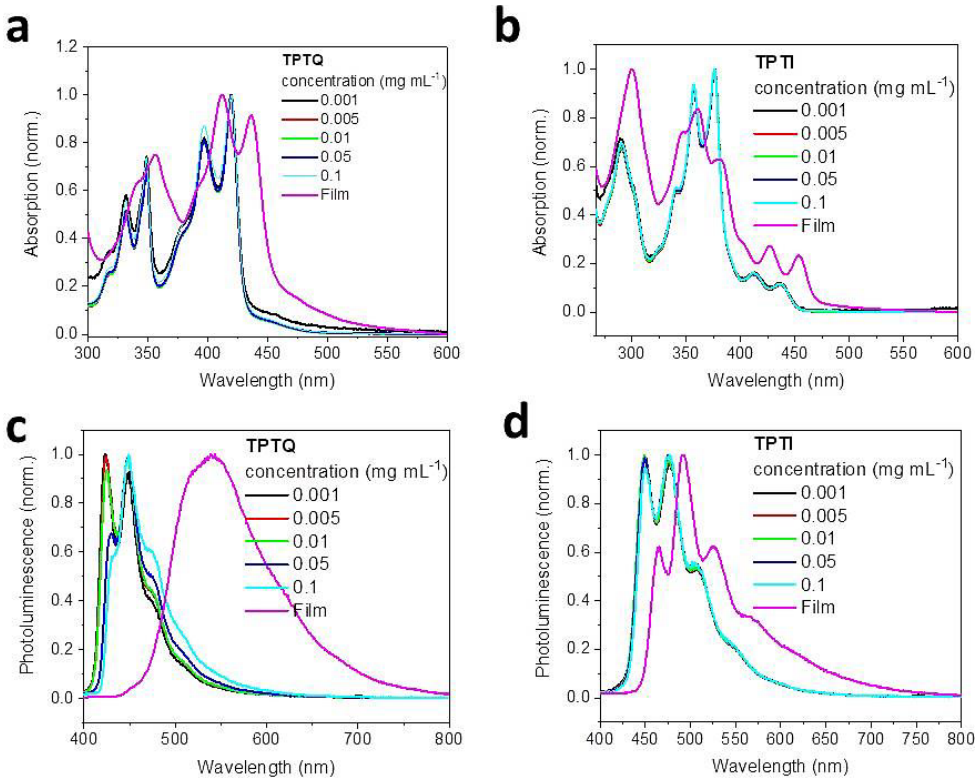

Figure 5.15. a) Concentration dependent absorption spectra of TPTQ chloroform solutions and thin films; **b)** Concentration dependent absorption spectra of TPTI chloroform solutions and thin films; **c)** Concentration dependent photoluminescence spectra of TPTQ chloroform solutions and thin films; **d)** Concentration dependent photoluminescence spectra of TPTI chloroform solutions and thin films.

Fluorescence spectra were measured using Horiba FluoroLog fluorometer at the University of Chicago MRSEC MPML. Time-dependent fluorescence decay spectra were measured using ISS Chronos BH fluorometer at the University of Chicago MRSEC MPML. Instrument response function was estimated using standard 1% LUDOX solution from Sigma Aldrich. Exponential decay fitting was performed using the software provided with the instrument.

Device fabrication

Devices were assembled in BG-TC configuration. B doped silicon wafers with 300 nm silicon nitride were purchased from University Wafers and used as substrates. Wafers were cut into 14×19 mm slides and ultrasonicated in acetone and isopropanol for 15 min each. After that they were dried using compressed dry nitrogen. Silicon wafers were modified either with a layer of PMMA or with OTS. For PMMA modification 30 mg mL-1 solution in n-propyl acetate was used. Solution was filtered through 0.2 μm PTFE filter and spin-coated in glove box at 2500 rpm for 30 seconds. The obtained film annealed at 150°C for 30 min in glove box. For OTS modification, silicon wafers were put in glass petri dish and several drops of octadecyltrichlorosilane were added. It was kept in vacuum oven overnight at temperature 120°C. After modification wafers were kept in glove box. Solution of DPP-DTT 2 mg mL^{-1} was prepared in chloroform 24 hours before the coating. Solution was spin-coated on rotating substrate at 1500 rpm/60 seconds and annealed at 150°C for 30 min in glove box. Active layer polymers TPTQ-C and TPTI-C were dissolved in p-xylene for 24 hours to prepare solutions with the concentration 10 mg mL^{-1} and spin-coated on DPP-DTT from warm solutions at 1500 rpm for 30 seconds. Polymer films were annealed at 100°C for 30 min in glove box. PFN-BIm4 was dissolved in methanol overnight to prepare solution with the concentration 2 mg mL^{-1}. Solution was filtered through PVDF filter and spin-coated on active layer at 7000 rpm for 30 seconds. Polymer films were annealed at 60°C for 20 min in air and transferred back to glove box for thermal deposition of source-drain electrodes. 70 nm of gold was deposited in vacuum chamber under pressure $<10^{-6}$ Torr through a shadow mask purchased from Ossila Ltd.

Device characterization

All devices were tested in nitrogen glovebox in dark. Two-channel SMU Keithley 2612A was used to test output and transfer characteristics of devices. The custom-built experimental stage was used for the measurements. Needle probes from Quater Research were used for measurements. A microscope with a USB camera from AmScope was used for needle probe alignment with the device contacts. The same microscope with more sensitive camera MU530-BI-CK from AmScope was used to observe light emission from OLEFET.

Table 5.6 Mobilities of single layer FET devices with active layer materials

Material	μ_h ($cm^2V^{-1}s^{-1}$)	μ_{el} ($cm^2V^{-1}s^{-1}$)
TPTQ-C	6.9×10^{-5}	-
TPTI-C	-	2.9×10^{-6}

Electroluminescence spectra of emissive polymers were obtained from brighter OLED devices using TPTQ-C and TPTI-C as emissive layers. The structure of the OLED devices was ITO/PEDOT:PSS/emissive layer/Ca/Al. ITO glasses were ultrasonicated in chloroform, acetone and isopropanol for 15 minutes each and dried using compressed nitrogen. Glasses were cleaned in UV/ozone for 20 minutes. PEDOT:PSS from Heraeus was spin-coated on ITO at 6000 rpm for 60 seconds and annealed in vacuum oven at 95°C. Solution of TPTQ-C and TPTI-C in p-xylene with the concentration 10 mg mL^{-1} was spin-coated on PEDOT:PSS at 1500 rpm for 30 seconds and annealed at 100°C for 30 min in glovebox. 20 nm calcium and 80 nm aluminum were thermally evaporated in vacuum chamber under pressure $<10^{-6}$ Torr through a shadow mask that defined the device area 3.14 mm^2. Electroluminescence spectra of these OLEDs were

measured using calibrated integrating sphere AvaSphere-50-IRRAD and AvaSpec-ULS2048 spectrometer from Avantes and source meter unit Keithley 2420 to drive OLED.

In order to measure EQE of OLEFET devices we used a modified method previously described elsewhere.[28] The photodiode FDS100-CAL purchased from Thorlabs was calibrated with OLED of known irradiance based on the same emissive layer as OLEFET. Irradiance of OLED was measured using calibrated integrating sphere AvaSphere-50-IRRAD and AvaSpec-ULS2048 spectrometer. Photocurrent from the calibrated photodiode placed right in front of the operating device was used to calculate brightness of OLEFET devices and based on it calculate photon flux. Lambertian emission was assumed. Number of electrons injected in the device was calculated from source drain current. EQE was calculated as the ratio of photon flux to number of injected electrons per second.

DFT calculations

DFT calculations were performed using Gaussian 09. B3LYP method and 6-31g** basis were used[29].

Morphology studies

The GIWAXS measurements were performed at 8ID-E beamline of Advanced Photon source Argonne National Laboratory with the radiation wavelength 1.1354 Å. Samples were prepared on polished silicon wafer covered with PEDOT:PSS. The same solvent and annealing mode was used as in the actual device fabrication process.

5.5 References

(1) Ostroverkhova, O. Organic Optoelectronic Materials: Mechanisms and Applications. *Chem. Rev.* **2016**, *116*, 13279–13412.

(2) Lu, L.; Zheng, T.; Wu, Q.; Schneider, A. M.; Zhao, D.; Yu, L. Recent Advances in Bulk Heterojunction Polymer Solar Cells. *Chem. Rev.* **2015**, *115*, 12666–12731.

(3) Wadsworth, A.; Moser, M.; Marks, A.; Little, M. S.; Gasparini, N.; Brabec, C. J.; Baran, D.; McCulloch, I. Critical Review of the Molecular Design Progress in Non-Fullerene Electron Acceptors towards Commercially Viable Organic Solar Cells. *Chem. Soc. Rev.* **2019**, *48*, 1596–1625.

(4) Hu, H.; Ye, L.; Ghasemi, M.; Balar, N.; Rech, J. J.; Stuard, S. J.; You, W.; O'Connor, B. T.; Ade, H. Highly Efficient, Stable, and Ductile Ternary Nonfullerene Organic Solar Cells from a Two-Donor Polymer Blend. *Adv. Mater.* **2019**, *31*, 1808279.

(5) Yuan, J.; Zhang, Y.; Zhou, L.; Zhang, C.; Lau, T.; Zhang, G.; Lu, X.; Yip, H.; So, S. K.; Beaupré, S.; *et al.* Fused Benzothiadiazole: A Building Block for N-Type Organic Acceptor to Achieve High-Performance Organic Solar Cells. *Adv. Mater.* **2019**, *31*, 1807577.

(6) Zhang, C.; Chen, P.; Hu, W. Organic Light-Emitting Transistors: Materials, Device Configurations, and Operations. *Small* **2016**, *12*, 1252–1294.

(7) Liu, C.-F.; Liu, X.; Lai, W.-Y.; Huang, W. Organic Light-Emitting Field-Effect Transistors: Device Geometries and Fabrication Techniques. *Adv. Mater.* **2018**, *1802466*, 1802466.

(8) Hou, L.; Zhang, X.; Cotella, G. F.; Carnicella, G.; Herder, M.; Schmidt, B. M.; Pätzel, M.; Hecht, S.; Cacialli, F.; Samorì, P. Optically Switchable Organic Light-Emitting Transistors. *Nat. Nanotechnol.* **2019**, *14*, 347–353.

(9) Ullah, M.; Tandy, K.; Li, J.; Shi, Z.; Burn, P. L.; Meredith, P.; Namdas, E. B. High-Mobility, Heterostructure Light-Emitting Transistors and Complementary Inverters. *ACS Photonics* **2014**, *1*, 954–959.

(10) Capelli, R.; Toffanin, S.; Generali, G.; Usta, H.; Facchetti, A.; Muccini, M. Organic Light-Emitting Transistors with an Efficiency That Outperforms the Equivalent Light-Emitting Diodes. *Nat. Mater.* **2010**, *9*, 496–503.

(11) Hepp, A.; Heil, H.; Weise, W.; Ahles, M.; Schmechel, R.; von Seggern, H. Light-Emitting Field-Effect Transistor Based on a Tetracene Thin Film. *Phys. Rev. Lett.* **2003**, *91*, 157406.

(12) Wawrzinek, R.; Muhieddine, K.; Ullah, M.; Koszo, P. B.; Shaw, P. E.; Grosjean, A.; Maasoumi, F.; Stoltzfus, D. M.; Clegg, J. K.; Burn, P. L.; *et al.* Orange-Red-Light-Emitting Field-Effect Transistors Based on Phosphorescent Pt(II) Complexes with Area Emission. *Adv. Opt. Mater.* **2016**, *4*, 1867–1874.

(13) Ullah, M.; Tandy, K.; Clulow, A. J.; Burn, P. L.; Gentle, I. R.; Meredith, P.; Lo, S. C.; Namdas, E. B. Host-Free Blue Phosphorescent Dendrimer Organic Light-Emitting Field-Effect Transistors and Equivalent Light-Emitting Diodes: A Comparative Study. *ACS Photonics* **2017**, *4*, 754–760.

(14) Song, L.; Hu, Y.; Liu, Z.; Lv, Y.; Guo, X.; Liu, X. Harvesting Triplet Excitons with

Exciplex Thermally Activated Delayed Fluorescence Emitters toward High Performance Heterostructured Organic Light-Emitting Field Effect Transistors. *ACS Appl. Mater. Interfaces* **2017**, *9*, 2711–2719.
(15) Zaumseil, J.; Sirringhaus, H. Electron and Ambipolar Transport in Organic Field-Effect Transistors. *Chem. Rev.* **2007**, *107*, 1296–1323.
(16) Ren, Y.; Yang, X.; Zhou, L.; Mao, J.; Han, S.; Zhou, Y. Recent Advances in Ambipolar Transistors for Functional Applications. *Adv. Funct. Mater.* **2019**, 1902105.
(17) Mei, J.; Bao, Z. Side Chain Engineering in Solution-Processable Conjugated Polymers. *Chem. Mater.* **2014**, *26*, 604–615.
(18) Setayesh, S.; Grimsdale, A. C.; Weil, T.; Enkelmann, V.; Müllen, K.; Meghdadi, F.; List, E. J. W.; Leising, G. Polyfluorenes with Polyphenylene Dendron Side Chains: Toward Non-Aggregating, Light-Emitting Polymers. *J. Am. Chem. Soc.* **2001**, *123*, 946–953.
(19) Zhang, F.; Hu, Y.; Schuettfort, T.; Di, C.; Gao, X.; Mcneill, C. R.; Thomsen, L.; Mannsfeld, S. C. B.; Yuan, W.; Sirringhaus, H.; *et al.* Critical Role of Alkyl Chain Branching of Organic Semiconductors in Enabling Solution-Processed N-Channel Organic Thin-Film Transistors with Mobility of up to 3.50 Cm 2 V−1s −1. *J. Am. Chem. Soc.* **2013**, *135*, 2338–2349.
(20) Kang, I.; Yun, H.-J.; Chung, D. S.; Kwon, S.-K.; Kim, Y.-H. Record High Hole Mobility in Polymer Semiconductors via Side-Chain Engineering. *J. Am. Chem. Soc.* **2013**, *135*, 14896–14899.
(21) Cai, Z.; Awais, M. A.; Zhang, N.; Yu, L. Exploration of Syntheses and Functions of Higher Ladder-Type π-Conjugated Heteroacenes. *Chem* **2018**, *4*, 2538–2570.
(22) Cai, Z.; Zhang, N.; Awais, M. A.; Filatov, A. S.; Yu, L. Synthesis of Alternating Donor–Acceptor Ladder-Type Molecules and Investigation of Their Multiple Charge-Transfer Pathways. *Angew. Chemie - Int. Ed.* **2018**, *57*, 6442–6448.
(23) Zhang, X.; Bronstein, H.; Kronemeijer, A. J.; Smith, J.; Kim, Y.; Kline, R. J.; Richter, L. J.; Anthopoulos, T. D.; Sirringhaus, H.; Song, K.; *et al.* Molecular Origin of High Field-Effect Mobility in an Indacenodithiophene- Benzothiadiazole Copolymer. *Nat. Commun.* **2013**, *4*, 2238.
(24) Carlotti, B.; Cai, Z.; Kim, H.; Sharapov, V.; Madu, I. K.; Zhao, D.; Chen, W.; Zimmerman, P. M.; Yu, L.; Goodson, T. Charge Transfer and Aggregation Effects on the Performance of Planar vs Twisted Nonfullerene Acceptor Isomers for Organic Solar Cells. *Chem. Mater.* **2018**, *30*, 4263–4276.
(25) Jung, I. H.; Lo, W.-Y.; Jang, J.; Chen, W.; Zhao, D.; Landry, E. S.; Lu, L.; Talapin, D. V; Yu, L. Synthesis and Search for Design Principles of New Electron Accepting Polymers for All-Polymer Solar Cells. *Chem. Mater.* **2014**, *26*, 3450–3459.
(26) Jung, I. H.; Zhao, D.; Jang, J.; Chen, W.; Landry, E. S.; Lu, L.; Talapin, D. V.; Yu, L. Development and Structure/Property Relationship of New Electron Accepting Polymers Based on Thieno[2′,3′:4,5]Pyrido[2,3- *g*]Thieno[3,2- *c*]Quinoline-4,10-Dione for All-Polymer Solar Cells. *Chem. Mater.* **2015**, *27*, 5941–5948.
(27) Yang, R.; Wu, H.; Cao, Y.; Bazan, G. C. Control of Cationic Conjugated Polymer Performance in Light Emitting Diodes by Choice of Counterion. *J. Am. Chem. Soc.* **2006**, *128*, 14422–14423.
(28) Chaudhry, M. U.; Muhieddine, K.; Wawrzinek, R.; Li, J.; Lo, S. C.; Namdas, E. B. Nano-

Alignment in Semiconducting Polymer Films: A Path to Achieve High Current Density and Brightness in Organic Light Emitting Transistors. *ACS Photonics* **2018**, *5*, 2137–2144.

(29) Gaussian 09, Revision A.02, M. J. Frisch, G. W. Trucks, H. B. Schlegel, G. E. Scuseria, M. A. Robb, J. R. Cheeseman, G. Scalmani, V. Barone, G. A. Petersson, H. Nakatsuji, X. Li, M. Caricato, A. Marenich, J. Bloino, B. G. Janesko, R. Gomperts, B. Mennucci, H. P. Hratchian, J. V. Ortiz, A. F. Izmaylov, J. L. Sonnenberg, D. Williams-Young, F. Ding, F. Lipparini, F. Egidi, J. Goings, B. Peng, A. Petrone, T. Henderson, D. Ranasinghe, V. G. Zakrzewski, J. Gao, N. Rega, G. Zheng, W. Liang, M. Hada, M. Ehara, K. Toyota, R. Fukuda, J. Hasegawa, M. Ishida, T. Nakajima, Y. Honda, O. Kitao, H. Nakai, T. Vreven, K. Throssell, J. A. Montgomery, Jr., J. E. Peralta, F. Ogliaro, M. Bearpark, J. J. Heyd, E. Brothers, K. N. Kudin, V. N. Staroverov, T. Keith, R. Kobayashi, J. Normand, K. Raghavachari, A. Rendell, J. C. Burant, S. S. Iyengar, J. Tomasi, M. Cossi, J. M. Millam, M. Klene, C. Adamo, R. Cammi, J. W. Ochterski, R. L. Martin, K. Morokuma, O. Farkas, J. B. Foresman, and D. J. Fox, Gaussian, Inc., Wallingford CT, 2016.